THREE-DIMENSIONAL IMAGING TECHNIQUES FOR BIOMEDICAL APPLICATIONS

by

Shaobai Li

A Dissertation Submitted to the Faculty of the

JAMES C. WYANT COLLEGE OF OPTICAL SCIENCES

In Partial Fulfillment of the Requirements

For the Degree of

DOCTOR OF PHILOSOPHY

In the Graduate College

THE UNIVERSITY OF ARIZONA

2024

THE UNIVERSITY OF ARIZONA
GRADUATE COLLEGE

As members of the Dissertation Committee, we certify that we have read the dissertation prepared by *Shaobai Li,* titled *Three-Dimensional Imaging Techniques for Biomedical Applications* and recommend that it be accepted as fulfilling the dissertation requirement for the Degree of Doctor of Philosophy.

Rongguang Liang — Date: 06/20/2024
Professor Rongguang Liang, Chair

Dongkyun Kang — Date: 6/20/24
Professor Dongkyun Kang

Travis W. Sawyer — Date: 6/20/24
Professor Travis W. Sawyer

Final approval and acceptance of this dissertation is contingent upon the candidate's submission of the final copies of the dissertation to the Graduate College.

I hereby certify that I have read this dissertation prepared under my direction and recommend that it be accepted as fulfilling the dissertation requirement.

Rongguang Liang — Date: 06/20/2024
Professor Rongguang Liang
Dissertation Committee Chair
Wyant College of Optical Sciences

ACKNOWLEDGMENTS

Firstly and most importantly, I would like to thank my advisor Prof. Rongguang Liang for all his help and guidance during my Ph.D. career. His motivation, patience, immense knowledge, and unwavering support have influenced me to be a better person. I am very grateful to him for generously sharing his knowledge and skills in optics with me and for providing me with the opportunity to broaden my horizons and conduct valuable research in optics. It is my true privilege to have him as my advisor and mentor.

Besides my advisor, I would like to thank the rest of my dissertation committee members, Dr. Dongkyun Kang and Dr. Travis William Sawyer, for their invaluable time, guidance, and helpful review of this dissertation.

I would like to thank the National Institutes of Health (NIH), for the financial support for this project and my research assistantship.

I would like to thank all the members of the Applied Optics Lab that I have met throughout my Ph.D. career. I would like to thank Xiaobo Tian, Bofan Song, Zhihan Hong, Wenjun Kang, Qi Cui, Yuanyuan Sun, Jiabin Chen, Tyler Peterson, Yihan Wang, Ruilin You, Shuyuan Guan, Shengtai Zhu for their invaluable discussions and friendship. I also would like to thank Daodang Wang and Hongzhang Ma for their help and support.

I would like to thank all my friends I met in Tucson: Yifan Hong, Xianyue Deng, Chaohan Cui,Ted Lee, Miaomiao Xu, Xingzhou Tu, Yuanxin Guan, Tianyao Zhang and many others for their friendship.

Finally, I would like to thank my wife Jingwei Zhao for his continuous love, support, and care. Thank my parents and family for their endless encouragement and unconditional love. Thank them all for giving me love and peace.

TABLE OF CONTENTS

LIST OF FIGURES

LIST OF TABLES

ABSTRACT

The pursuit of extended depth, higher resolution, and three-dimensional (3D) imaging capabilities has been a driving force in the field of biomedical imaging and clinical applications. By providing detailed volumetric representations of biological structures, 3D imaging modalities offer significant advantages over traditional 2D imaging methods, enabling unprecedented insights into the complex three-dimensional architecture and dynamics of biological systems. Chromatic confocal microscopy and Optical Coherence Tomography (OCT) stand out as two techniques offering high-resolution, non-invasive 3D visualization of living tissues and organisms. Chromatic confocal microscopy utilizes longitudinal chromatic aberration to conduct depth scans, facilitating high-resolution 3D imaging of specimens. On the other hand, OCT, a non-invasive interferometric technique, relies on low-coherence interferometry to capture high-resolution depth images of tissues. OCT provides detailed 3D representations of tissue microstructures, making it a valuable tool in clinical disciplines such as ophthalmology, cardiology, and dermatology.

In this dissertation, we concentrate on Chromatic confocal microscopy and Swept source OCT these two techniques and their applications. We first present two digital scanning chromatic confocal microscopes: DMD-based and MicroLED-based chromatic confocal microscopes that eliminate the need for mechanical scanning. Furthermore, we discuss system

enhancements achieved through custom optical design, including the integration of freeform prism pairs and hyperchromatic objectives. These advancements enable higher resolution, extended depth imaging, and multifunctional imaging. In terms of SS-OCT, we demonstrate the development of a multimodal intraoral screening system for oral cancer. This system integrates bright field imaging, autofluorescence imaging, and Swept-source OCT, enabling multi-modalities of intraoral imaging. The optical design, mechanical design, and software architecture of this system are comprehensively discussed. The final integrated system and preliminary results will be presented.

Chapter 1

Introduction

1.1 Overview

Three-dimensional (3D) biomedical imaging techniques have undergone a radical transformation over the past century, propelled by continual innovation and technological advancements [1, 2]. These techniques utilize advanced imaging modalities to capture detailed volumetric data of biological specimens, enabling researchers and clinicians to visualize, analyze, and monitor biological phenomena in three dimensions [2, 3]. They provide a broader perspective for understanding the complex structure and function of biological systems and are widely used in various medical fields. For example, they facilitate more precise localization and characterization of tumors [4], leading to improved diagnosis and management of cardiovascular diseases. Moreover, they enhance surgical planning for orthopedic procedures and provide detailed visualization of the brain's anatomy and function [5]. Beyond medical practice, 3D imaging has emerged as a valuable tool for patient education, enabling healthcare professionals to convey complex medical information effectively and empowering patients to make informed decisions about their health [6].

Figure 1.1 shows the current medical imaging modalities and their respective scales in terms of resolution and penetration depth[7]. It illustrates that current medical techniques

have a trade-off between resolution and penetration depth. As shown, there is an inverse relationship between these two factors, with higher resolution techniques having shallower penetration depths, and vice versa.

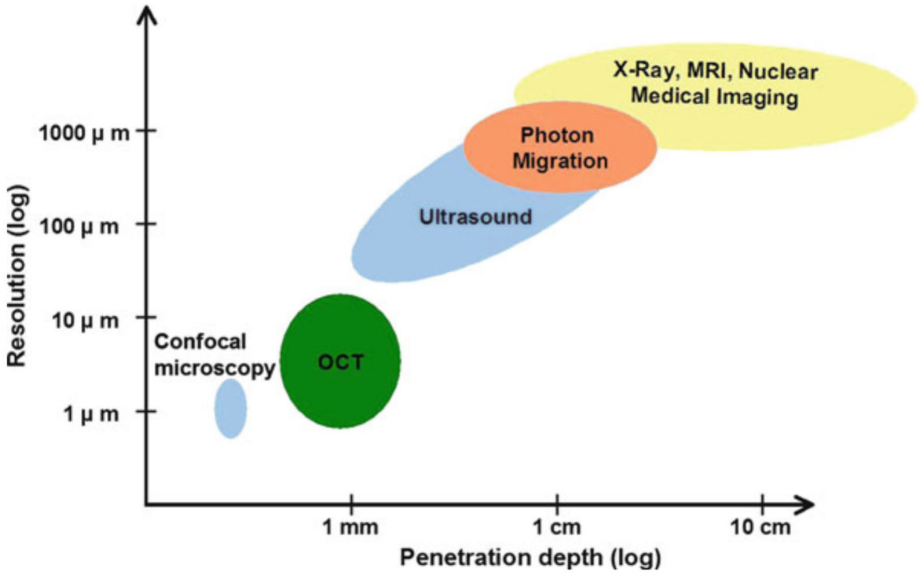

Figure 1.1: 3D medical imaging modalities and their scales.[7]

Confocal Microscopy, with its exceptional spatial resolution, is widely employed in cellular and molecular biology for capturing detailed 3D images of biological samples through 3D scanning[8, 9, 10]. This technique facilitates studies on cellular structures, dynamics, and interactions at the microscopic level.

Optical coherence tomography (OCT) is an optical imaging modality based on low-coherence interferometry [11, 12]. It enables the noninvasive, noncontact imaging of cross-sectional structures in biological tissues and materials with high resolution [13].

Ultrasound Imaging is a non-optical imaging technique based on high-frequency sound waves [14]. The ultrasound image is produced based on the reflection of the waves off of the body structures [15].

Computed Tomography (CT) imaging utilizes X-rays to produce cross-sectional images of the body, allowing for precise anatomical visualization and detection of abnormalities such as tumors and fractures [16]. On the other hand, Magnetic Resonance Imaging (MRI) employs powerful magnetic fields and radio waves to generate high-resolution 3D images of soft tissues [17], making it invaluable for diagnosing conditions ranging from brain disorders to musculoskeletal injuries[18].

These 3D imaging techniques not only enhance our understanding of biological processes at various scales but also drive innovations in medical diagnosis, treatment planning, and drug discovery, ultimately contributing to advancements in healthcare and biomedicine.

1.2 Introduction to Chromatic Confocal Microscopy

1.2.1 Confocal Microscopy

The concept of confocal microscopy was first proposed by Minsky in the 1950's [19]. Then in the 1970's, the first detailed investigation of the imaging performance of confocal microscopy revealed that the transverse resolution in confocal microscopy is 1.4 times greater than that of conventional microscopes [20]. However, this improvement in resolution comes at the expense of a reduced field of view, which can be easily compensated for by using the scanning mechanism [21]. Confocal scanning microscopy exhibits a remarkable depth discrimination capability: it preferentially detects in-focus signals while significantly attenuating out-of-focus information. This contrasts with conventional microscopy systems, where out-of-focus signals are merely blurred but still contribute to the final image [22]. Furthermore, confocal microscopy mitigates noise arising from flare and undesired scattered

light by employing a small pinhole aperture in front of the detector [23]. This spatial filtering mechanism effectively rejects a substantial portion of the unwanted light, leading to improved signal-to-noise ratio and enhanced image quality [23]. These unique attributes offer confocal microscopy the optical sectioning ability. It facilitates the acquisition of the particular transverse section in a thick object with high resolution and high contrast to form a 3D image accordingly [24].

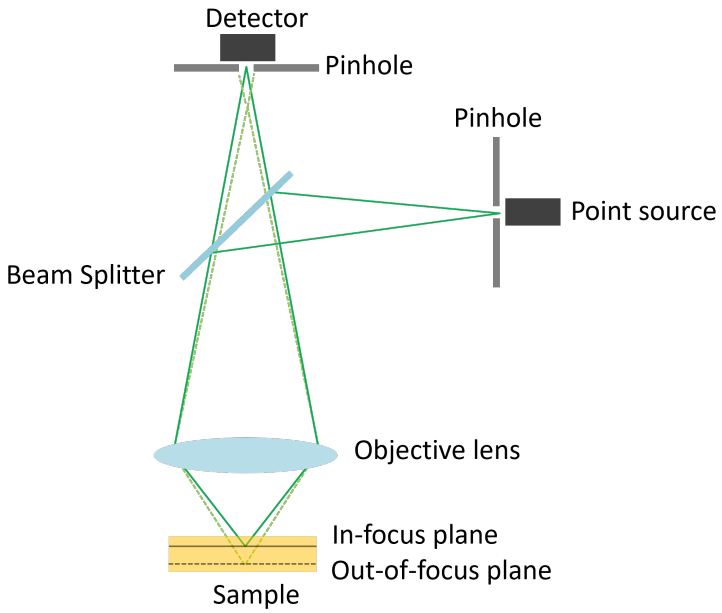

Figure 1.2: Schematic diagram of a reflectance confocal scanning microscope.

.

Figure 1.2 demonstrates the principle of optical sectioning in a reflectance confocal scanning imaging system. Reflectance confocal microscopy typically contains two conjugate pinholes: one is used to generate a point light source, and the other is placed in front of the detector. The light from the point source is firstly focused on the tissue by an objective lens. The backscattered light from the different layers of the tissue is collected by the objective lens and then focused on the detector. When the object is located in the focal plane of the

objective (solid lines in Figure 1.2), the reflected beam is focused exactly onto the point detector, allowing it to collect a significant portion of the incident energy. However, when the object is away from the focal plane (dashed lines in Figure 1.2), most of the signal is rejected by the pinhole in the detection path. This optical sectioning capability enables direct imaging of a thin layer within thick, unsliced tissue specimens while maintaining excellent contrast. In this configuration, the microscope acquires data from the sample on a point-by-point basis. To create a 2D image of the sample, a scanning mechanism, such as a galvanometric mirror, is employed to raster scan the light across the lateral dimensions [25]. For imaging thick three-dimensional objects, a series of optical sections at different depths within the specimen are recorded. These individual sections can then be stacked together to form a complete 3D representation of the thick object [26], effectively visualizing its internal structure without the need for physical sectioning.

In conventional microscopy, the optical resolution is characterized by the system's point spread function (PSF) in terms of irradiance. Assume the system is aberration-free and has uniform illuminated circular aperture, then the PSF can be written as[20]:

$$h(u,v) = \int_0^1 \mathrm{P}(\rho) \exp\left(\frac{ju\rho^2}{2}\right) J_0(\rho v)\rho \, d\rho \tag{1.1}$$

Where P is the pupil function, ρ is the normalized radial pupil coordinate centered on the optical axis, u and v are the normalized optical coordinates in the axial direction (z) and transverse direction in the object plane (r) by the following equation:

$$\begin{cases} u = \dfrac{2\pi}{\lambda}\dfrac{NA^2}{n}z \\ v = \dfrac{2\pi r}{\lambda}\mathrm{NA} \end{cases} \tag{1.2}$$

where λ is the wavelength, NA is the numerical aperture of the objective lens, n is the refraction index in the object space, z and r are the real coordinates in axial direction and transverse direction, respectively. The irradiance on the image plane can be obtained based on incoherent PSF as[20]:

$$I_{\mathrm{conv}}(u,v) = |h(u,v)|^2 \tag{1.3}$$

Here, the I_{conv} represents the irradiance of the conventional microscope. Applying the relation $\int_0^x x' J_0(x')dx' = xJ_1(x)$ into equation 1.1 and 1.3, the normalized irradiance on the image plane along the lateral direction (0, v) and axial direction (u,0) are:

$$\begin{cases} I_{\mathrm{conv}}(0,v) = \left(\dfrac{2J_1(v)}{v}\right)^2 \\ I_{\mathrm{conv}}(u,0) = \mathrm{sinc}^2\left(\dfrac{u}{4}\right) \end{cases} \tag{1.4}$$

$I_{conv}(0,v)$ is the irradiance distribution in the transverse direction on the image plane, which is also called the Airy disk. The resolution of an optical system can be estimated by the Rayleigh criterion defined by Lord Rayleigh: two point sources are regarded as just resolved when the principal diffraction maximum (center) of the Airy disk of one image coincides with the first minimum of the Airy disk of the other. The Airy disk hits zero intensity when

$$J_1(v) = J_1\left(\frac{2\pi r}{\lambda}\mathrm{NA}\right) = 0 \tag{1.5}$$

then the lateral resolution is given by:

$$\delta r_{\text{lateral}} = 0.61\frac{\lambda}{\text{NA}} \tag{1.6}$$

Similarly, the conventional microscope axial resolution is determined by the depth of focus, where

$$\text{sinc}^2\left(\frac{u}{4}\right) = \text{sinc}^2\left(\frac{\pi}{2\lambda}\frac{\text{NA}^2}{n}z\right) = 0 \tag{1.7}$$

then the axial resolution is given by

$$\delta z_{\text{axial}} = 2\frac{n\lambda}{\text{NA}^2} \tag{1.8}$$

Furthermore, in confocal microscopy, pointwise illumination scanning and pointwise detection are employed, so that only the backscattered light in the shared volume of the illumination and detection PSFs can be detected. For a system using the same illumination and detection path, the normalized irradiance PSF is given by [27]:

$$\begin{aligned} I_{\text{confocal}}(u,v) = \int_0^{v_p} \Bigg| &\left\{\int_0^1 P(\rho)\exp\left(\frac{ju\rho^2}{2}\right)J_0(\rho v)\rho d\rho\right\} \\ &\times\left\{\int_0^1 P(\rho)\exp\left(\frac{ju\rho^2}{2}\right)J_0(\rho v)\rho d\rho\right\}\Bigg|^2 v dv \end{aligned} \tag{1.9}$$

where v_p is the normalized radius of the pinhole in the optical coordinates. Therefore, the ideal irradiance distribution at the focal plane(u=0) is:

$$I_{\text{confocal}}(v) = \left(\frac{2J_1(v)}{v}\right)^4 \tag{1.10}$$

Figure 1.3 shows the comparison of the lateral irradiance PSFs of a conventional microscope and confocal microscope. While the zero-crossing points of both PSFs coincide, the lateral Full-Width-Half-Maximum (FWHM) of the confocal microscope's PSF is narrower than that of the conventional microscope. The corresponding lateral resolution of confocal microscopy is given by:

$$\delta r_{\text{lateral\_confocal}} = \frac{0.37\lambda}{\text{NA}} \tag{1.11}$$

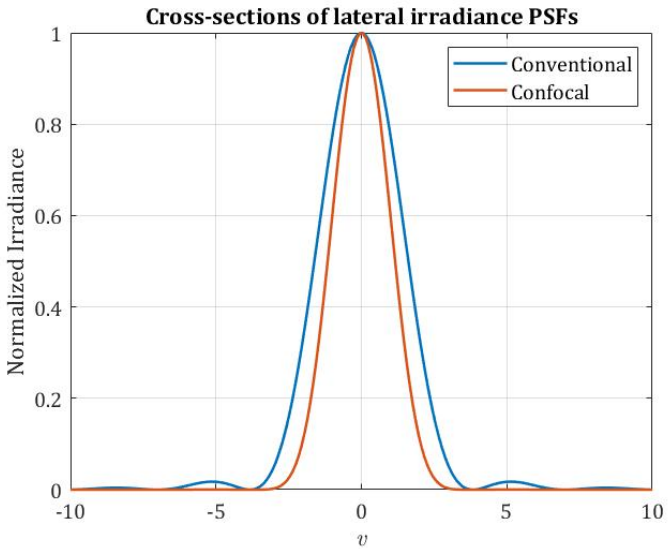

Figure 1.3: Comparison of the ideal lateral irradiance PSFs of a conventional microscope and confocal microscope.

.

Similarly, the ideal irradiance distribution of a single point along the axial direction of the confocal microscope can be obtained by:

$$I_{\text{confocal}}(u) = \left[\text{sinc}\left(\frac{u}{2}\right)\right]^2 \tag{1.12}$$

Figure 1.4 shows the comparison of the axial PSF of a conventional microscope and confocal microscope. The axial FWHM of the confocal microscope's response curve is narrower than that of the conventional microscope. The corresponding axial resolution of confocal microscopy is given by:

$$\delta z_{\text{axial\_confocal}} = 1.4\frac{n\lambda}{\text{NA}^2} \tag{1.13}$$

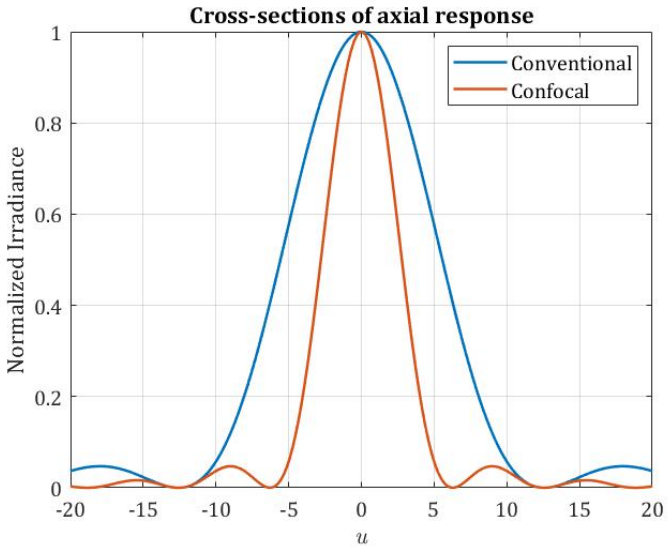

Figure 1.4: Comparison of the ideal axial PSF of a conventional microscope and confocal microscope.

.

Considering that the actual pinhole has a physical size, the real lateral and axial response of the confocal microscope can be evaluated by integrating the PSF over the pinhole as shown in Equation 1.9. Figure 1.5 plots the half-width of the confocal lateral PSF(lateral resolution of the confocal) as a function of pinhole size. We notice that $v_p = 0$ represents the single point resolution, the larger v_p conditions are equivalent to the conventional microscopes. Figure 1.6 plots the axial responses for a variety of values of v_p. We expect that the axial resolution will be greatest for $v_p = 0$, which means the single point case, and get worse

for larger v_p. This is further emphasized in Figure 1.7, which plots the axial response half-widths for different pinhole sizes. Another consideration is the confocal signal level. Figure 1.8 shows the confocal signal strength versus different pinhole sizes. For optimal sectioning performance and better signal-to-noise ratio (SNR), the pinhole size should be selected to be close to the size of the Airy disk($v_p \approx 3.8$). Reducing the pinhole size does not significantly enhance the sectioning capability but can lead to a reduction in signal irradiance, which is undesirable. Therefore, it is crucial to strike a balance between sectioning capability and signal intensity by carefully selecting the pinhole size in proximity to the Airy disk size.

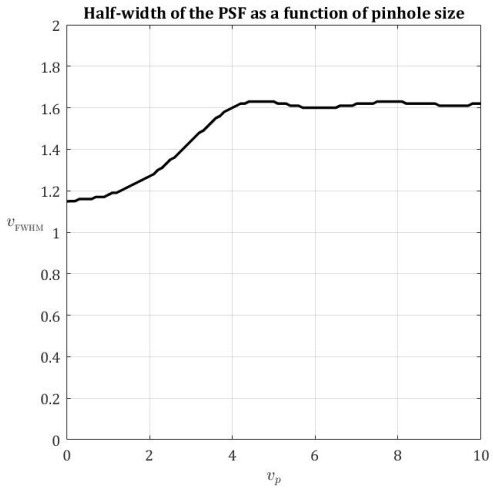

Figure 1.5: Half-width of the lateral PSF as a function of pinhole size.

.

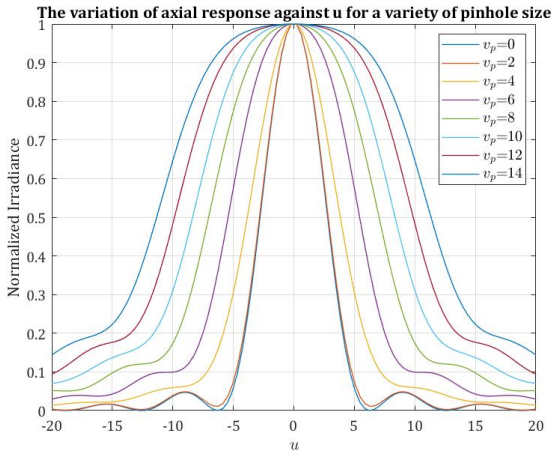

Figure 1.6: The variation of axial response as a function of u for a variety of pinhole size.

.

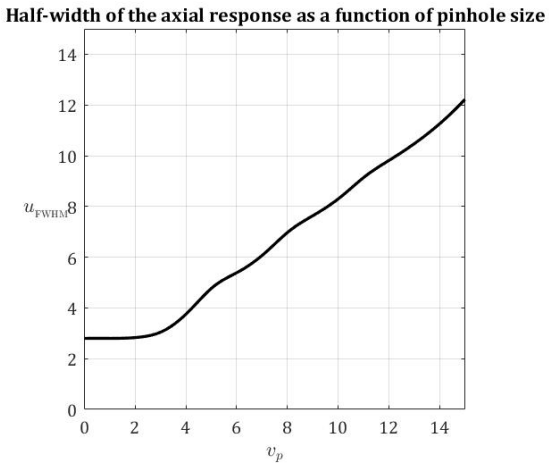

Figure 1.7: Half-width of the axial response as a function of pinhole size.

.

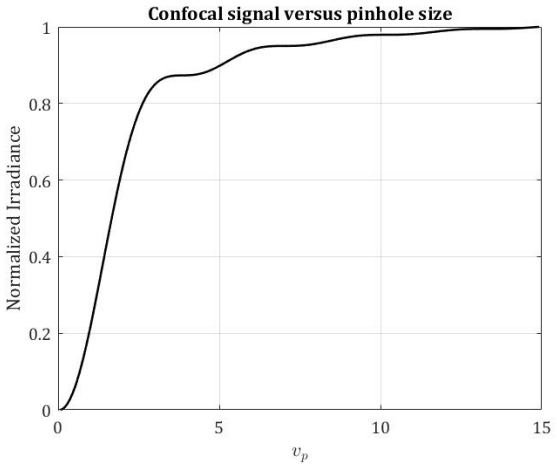

Figure 1.8: Confocal signal strength versus different pinhole size.

.

1.2.2 Chromatic Aberration

Chromatic aberration is a common optical problem that occurs when a lens is unable to focus all colors to the same point [28]. Chromatic aberration is caused by lens dispersion: the refractive index of the lens elements varies with the wavelength of light. As a result, different colors of the visible spectrum travel at slightly different speeds through the lens elements. It can be classified as longitudinal chromatic aberration: the longitudinal variation of the focus with wavelength(Dispersion of marginal ray); and lateral chromatic aberration [29]: the variation of the image size with wavelength(Dispersion of chief ray) as shown in Figure 1.9. It is common to select F (486.1327 nm, blue), d (587.5618 nm, yellow), and C (656.2725 nm, red) spectral lines for the design and analysis of visual systems [30]. As seen in the figure, the focus for F light is inside the paraxial focus for d light while the C light focus lies to the outside. This should be evident since the refractive index is progressively

greater for C, d, and F light thereby increasing the optical power of the thin lens:

$$\phi(\lambda) = (n(\lambda) - 1)(\frac{1}{r} - \frac{1}{r'}) \tag{1.14}$$

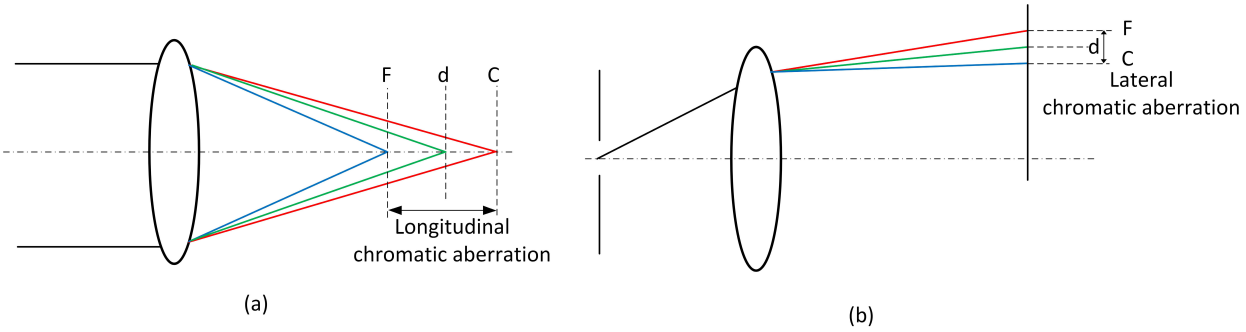

Figure 1.9: Chromatic aberration: (a)Longitudinal chromatic aberration and (b)lateral chromatic aberration.

.

The second-order chromatic wave aberration function can be written as [29]:

$$W(\vec{H}, \vec{\rho}) = \partial_\lambda W_{000} + \partial_\lambda W_{200}(\vec{H} \cdot \vec{H}) + \partial_\lambda W_{111}(\vec{H} \cdot \vec{\rho}) + \partial_\lambda W_{020}(\vec{\rho} \cdot \vec{\rho}), \tag{1.15}$$

where $\partial_\lambda W_{000}$ and $\partial_\lambda W_{200}$ represent chromatic changes of piston, $\partial_\lambda W_{020}$ the longitudinal chromatic aberration, and $\partial_\lambda W_{111}$ the lateral chromatic aberration.In this section, we will mainly focus on longitudinal chromatic aberration, since it's the fundamental principle for chromatic confocal microscopy.

The chromatic change of focus $\partial_\lambda W_{020}$ represents a quadratic difference between the wavefronts of two different wavelengths, which often are F and C light. It causes a longitudinal shift, along the optical axis, in the position of the images due to different wavelengths.

The longitudinal focal shift can be found as:

$$\Delta s'_{\lambda} = -\frac{2}{n'u'^2}\partial_{\lambda} W_{020} \tag{1.16}$$

where n' and u' are the refraction index and the marginal ray angle in the imaging space.

For a system with j optical surfaces, the longitudinal chromatic wave aberration is:

$$\partial_{\lambda} W_{020} = \frac{1}{2}\sum_{i=1}^{j} A\Delta\left(\frac{\partial n}{n}\right) y_j \tag{1.17}$$

where A is the marginal ray refraction invariant, which is equal to $ni = nu + nyc$. $y_j$is the marginal ray height at j^{th} surface. $\Delta(\frac{\partial n}{n}) = \frac{\partial n'}{n'} - \frac{\partial n}{n}$, $\partial n = n_F - n_C$ is the index of refraction difference for the F light and C light. It is noticed that the choice of wavelength depends on the specific application of the optical system.

When considering an optical system consisting of thin lenses, which are idealized models of lenses with negligible thickness but possessing optical power, certain calculations can be simplified. Specifically, the chromatic aberrations for a system of thin lenses in air can be expressed as follows:

$$\partial_{\lambda} W_{020} = \frac{1}{2}\sum_{i=1}^{j}\left[\frac{\phi}{\nu}y^2\right]_i \tag{1.18}$$

where phi is the optical power and ν is the Abbe number [31]:

$$\nu = \frac{n_d - 1}{n_F - n_C} \tag{1.19}$$

The longitudinal chromatic aberration in a thin lens system exhibits the following characteristics:

1. Independence from conjugate distances: The longitudinal chromatic aberration is independent of the object and image distances, as it is an intrinsic property of the lens material and its dispersion characteristics.

2. Dependence on marginal ray height: The longitudinal chromatic aberration is directly proportional to the square of the marginal ray height, which is the height of the outermost ray passing through the lens. This dependence arises from the fact that rays farther from the optical axis experience greater refraction and, consequently, greater dispersion.

3. Proportionality to optical power: The longitudinal chromatic aberration is directly proportional to the optical power of the thin lens element. Lenses with higher optical power (shorter focal lengths) exhibit greater chromatic aberration for a given lens material and wavelength range.

4. Inverse relationship with Abbe number: The longitudinal chromatic aberration is inversely proportional to the Abbe number of the lens material. The Abbe number is a measure of the material's dispersion characteristics, with higher values indicating lower dispersion and, consequently, lower chromatic aberration.

1.2.3 Chromatic Confocal Microscopy

To realize 3D imaging in a conventional confocal imaging system, mechanical point-by-point scanning in all three spatial dimensions is required [32]. This process involves

sequentially acquiring individual 2D images at different focal planes by precisely adjusting the position of the sample or the objective lens along the axial direction, while also performing lateral scanning within each focal plane. The whole 3D scan is typically achieved through the coordinated operation of various mechanical components, such as 2D (two-dimensional) galvanometer mirrors for lateral scanning[33], piezoelectric stages for axial positioning [34], and piezoelectric objective scanners[35, 36]. This intricate system not only contributes to its overall complexity and bulkiness but also imposes limitations on the speed of image acquisition, making the process relatively slow. Consequently, there is a need for more efficient and streamlined approaches to enable faster and more compact 3D confocal imaging systems.

Chromatic confocal microscopy is a technique that utilizes chromatic aberration to eliminate the mechanical scanning in the axial direction [37, 38, 39]. It encodes the focal length, or working distance, into the spectrum [40]. Compared with conventional confocal systems, there are three major differences in the chromatic confocal systems.

1. Objective lens design: Typical confocal systems use achromatic objective lenses which would minimize the wavelength dependence of focal length. However, in a chromatic confocal system, the objective is specially designed to introduce large longitudinal chromatic aberration which can provide a wide range of focal lengths for a given broadband light source [41]. Therefore, light with different wavelengths is focused at different depths.

2. Light source: Conventional confocal systems typically use narrow-band lasers as the light source. In contrast, chromatic confocal systems take advantage of broadband

light sources [42]. A broader range of wavelengths translates to a broader range of focal lengths due to the chromatic aberration introduced by the system's optics [43].

3. Detector: Instead of using a point detector, chromatic confocal systems employ a spectrometer [44]. The spectrometer retrieves depth information from the light passing through the confocal pinhole without requiring mechanical axial scanning. By analyzing the spectrum of the collected light, the system can reconstruct the axial information without physically moving the objective lens or the sample.

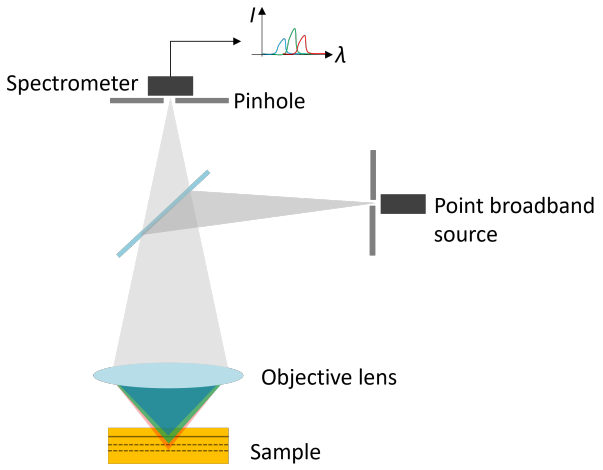

Figure 1.10: Schematic diagram of a chromatic confocal scanning microscope.

.

Figure 1.10 shows the schematic diagram of a chromatic confocal scanning microscope. Light from a broadband point source is focused at different depths in the sample plane by an objective lens designed with significant longitudinal chromatic aberration. The backscattered light from various layers of the sample is collected by the same objective lens and filtered through a pinhole, ensuring confocal operation. The filtered light is then focused onto a spectrometer, which analyzes the spectrum of the backscattered light. By decoding the

wavelength information from the detected spectrum, the system can reconstruct the axial depth information without the need for mechanical scanning along the axial direction. This process generates a single axial scan, commonly referred to as an A-scan. To create a 3D image of the sample, a lateral scanning mechanism, such as a galvanometric mirror, is employed. This scanner raster-scans the focused light across the lateral dimensions of the sample, allowing the system to acquire multiple A-scans at different lateral positions. By combining these A-scans, a complete three-dimensional reconstruction of the sample can be obtained [45]. The chromatic confocal scanning microscope eliminates the need for mechanical axial scanning, potentially offering faster acquisition rates and reduced system complexity compared to conventional confocal microscopes that rely on mechanical scanning in all three spatial dimensions.

1.3 Introduction to Optical Coherence Tomography

OCT is another in vivo 3D imaging modality that employs low coherence interferometry to obtain detailed cross-sectional images of optically scattering media [11]. By taking advantage of the short coherence length of a broadband light source, OCT performs high-resolution, cross-sectional, and three-dimensional volumetric imaging of the internal microstructure in biological tissues by measuring echoes of backscattered light [46]. Due to its non-invasive, cellular-level resolution and real-time capabilities, OCT has undergone rapid expansion and now finds extensive use in clinical applications [47, 48, 49].

The optical arrangement of OCT is very similar to that of a Michelson interferometer except that the monochromatic illumination is replaced by a broadband light source. Figure 1.11 shows the basic principle of OCT [50]. Firstly, a low temporal coherence light source,

such as a light-emitting diode (LED) or a supercontinuum laser, is employed as illumination. The light from the light source is divided into two arms, the reference and the sample arm. The sample arm directs the light towards the sample under investigation, where it interacts with the sample's internal structures, leading to reflections or backscattering of light. Concurrently, the light in the reference arm travels along a known path length and reflects off a mirror. The reflected or backscattered light from the sample in the sample arm is then combined with the light from the reference arm, resulting in an interference pattern. This interference signal is detected by a highly sensitive detector to analyze the depth information of the sample.

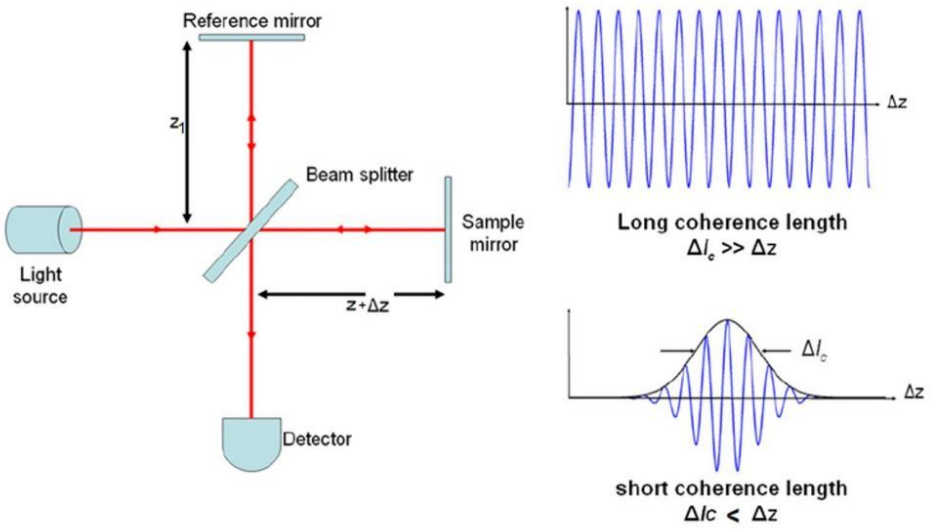

Figure 1.11: Schematic of OCT principle [50]

.

1.3.1 OCT Classification

In general, OCT can be classified into three types: time-domain OCT (TD-OCT), spectral domain OCT (SD-OCT), and swept-source OCT (SS-OCT) [51]. These classifications

are based on different choices of the light sources, reference arm configurations, and detection schemes, as demonstrated in Figure 1.12. For instance, in TD-OCT (Figure 1.12. (a)), the system captures the power density of the interference signal when employing broadband illumination. The back-reflected light from each arm is combined and only interferes if the optical path lengths match, therefore the time traveled by the light is nearly equal in both arms. The axial scanning of the reference mirror generates an interference fringe in the time domain [52]. Analyzing the demodulated signal envelope yields a one-dimensional depth profile of the sample, called A-scan (amplitude scan) [53]. In contrast to TD-OCT, FD-OCT(Figure 1.12. (b)) uses spectral information to generate A-scans without the need for mechanical scanning of the optical path length [54]. A spectrometer uses a diffractive element to spatially separate the different wavelength contributions into a line image which is recorded by a high-speed line scan camera. Each read-out of the camera constitutes a spectral interferogram with a superposition of fringe patterns. FFT (Fast Fourier transform) is used to transform the interference signal into the A-scan [55]. On the other hand, SS-OCT (Figure 1.12.(c)) adopts a different light source: the wavelength-swept laser source is essentially a rapidly tunable laser, which rapidly sweeps a narrow line-width over a broad range of wavelengths [56, 57]. During one sweep, each wavelength component of the interferometric signal is detected sequentially by a high-speed photo-detector. Each sweep produces a spectral interferogram containing fringe patterns, and the subsequent processing is similar to the SD-OCT to generate a single A-scan. For all three types of OCT systems, a 2D scanner like galvo mirror is required to create the cross-sectional image (B-Scan), or volume image. Comparing the three implementations of OCT, the acquisition speed of TD-OCT and SD-OCT are limited by the scanning reference mirror speed and linescan rate of the

camera, respectively. However, commercially available swept sources in SS-OCT can realize high sweep rates (>100 kHz), which is a good solution for volumetric and real-time imaging in clinical applications [58, 59].

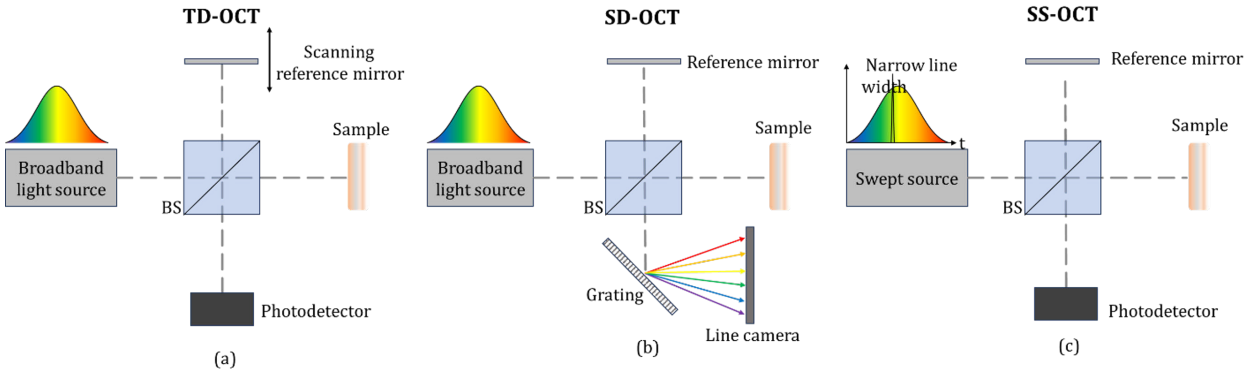

Figure 1.12: The schematics of three different types of OCT. (a) Time-domain OCT (TD-OCT), which uses a broadband light source along with a scanning reference mirror. The signal is detected by a photodetector. (b) Spectral-domain OCT (SD-OCT): the scanning reference mirror of the TD-OCT is replaced by a static mirror and a spectrometer is used to detect the interference signal. (c) Swept-source OCT (SS-OCT): a wavelength swept laser source is installed as the illumination. The scanning reference arm is made static, while the photodetector from the TD-OCT is kept.

.

1.3.2 Swept-source OCT Imaging Theory

The idea of low-coherence interferometry is the underlying principle for all OCT implementations. Interference only happens when the sample arm and reference arm optical lengths are matched within the coherence length L. Temporal coherence is a property of a light source and characterizes the temporal continuity of a wave emitted by the source and measured at a given point in space. For a Gaussian emission spectrum, the roundtrip coherence length L is given by equation 1.20 [60] :

$$L = \frac{2 \ln 2 \, \lambda_c^2}{\pi n \, \Delta\lambda} \tag{1.20}$$

where λ_c is the central wavelength, n is the group refractive index of the medium, and $\Delta\lambda$ is the (FWHM) spectral bandwidth of the spectrum of the light source. A light source with a broad spectral bandwidth is composed of a range of wavelengths. Such a broadband source has low coherence, while monochromatic laser light has a narrow spectral line and features a coherence length of at least several meters. For a single wavelength within the broad spectrum of the light source, the interference between the reference arm and the sample arm generates periodic interference fringes across space, with a specific spatial period. The detector can capture the interference signal at a particular location. Whether the detector registers bright or dark fringes depends on the optical path length difference between the two arms at that specific location. Different wavelengths within the source spectrum produce distinct interference modulation with varying spatial periods. The superposition of all these interference modulations from different wavelengths results in an overall interference pattern with varying fringe visibility across space.

Fringe visibility, quantified as the contrast of an interference pattern, is a measure of the difference in intensity between the bright and dark fringes relative to their average intensity, indicating the clarity and sharpness of the fringes [61].

The output OCT interference intensity can be represented by the following expression [62]:

$$I(k) = |E_S(k)|^2 + |E_R(k)|^2 + 2E_S(k)E_R(k)\cos(2k\Delta L + \varphi) + \text{c.c.} \tag{1.21}$$

where k is the wave number $2\pi/\lambda$, $E_S(k)$ and $E_R(k)$ are the electric fields from the sample arm and reference arm, respectively. ΔL is the optical path length difference between the sample arm and reference arm.

The interference signal consists of four terms. The first term on the right-hand side of the Equation denotes the autocorrelation term of the backscattered light from the sample arm, which is usually regarded as artifacts or noises in OCT images. The second term represents the autocorrelation term of the reflected light from the reference arm, which is considered the DC background. Fortunately, most OCT system is operated in shot-noise limited regime, where the first term is much smaller than the DC background and could thus be ignored. The third term, which is the interference term, provides the modulation information that we are looking after and the fourth term is its complex conjugate. In the third term, if the reference path length is scanned in TD-OCT [60], interference fringes will be generated as a function of scanning time or path difference. On the other hand, in SD-OCT and SS-OCT, the optical path difference ΔL is fixed. In order to generate the interference signal, SD-OCT performs a spatial scan of wave number k by means of a spectrometer and SS-OCT performs a temporal scan of wave number k by means of a swept source [63].

In swept source OCT, the expanded third term(interference term) could be further written as:

$$I_{\text{int}}(k) = S(k) \sum_{n} \left(\sqrt{R_S(z_n)} \overline{R_r} \cos(2kz_n + \varphi) \right) \tag{1.22}$$

Where R_r and R_s are the reflectivity of the reference arm and sample arm, respectively. $S(k)$ is the power density spectrum as a function of wavenumber k. z_n is the optical path difference (depth) at n^{th} layer of the sample. After the Fourier transform, detected back-scattered signals in the spatial domain could be reconstructed as:

$$I(z) = S(z) \otimes \sum_{n} \sqrt{R_S(z_n)} \overline{R_r} \left(\delta(z - z_n) + \delta(z + z_n) \right) \tag{1.23}$$

where $\bigotimes$ indicates the convolution operator, $S(z)$ is the autocorrelation function of the $S(k)$. In the equation, we can find that there are two mirror terms located in both z_n and $-z_n$, indicating the existence of the mirror image after the Fourier reconstruction. In addition, the obtained OCT image quality is determined by the convoluted version with a blurring kernel $S(z)$, which is the point spread function of the $S(z)$. Since $S(z)$ is a band-limited function, its spatial bandwidth Δz is related to the source temporal coherence length L as shown in equation 1.20. It could be concluded from equation 1.20 that the spatial bandwidth of the function $S(z)$ is proportional to the square of the central wavelength λ_c and inversely proportional to the $\Delta\lambda$. Therefore, a light source with a large wavelength bandwidth and a shorter central wavelength offer a higher axial resolution.

1.3.3 Swept-source OCT Performance Metrics

Several metrics are used to evaluate the performance and illustrate the limitations of the Swept-source OCT systems.

1. Axial resolution: The axial resolution shows the resolving power of SS-OCT along the depth direction. It is determined by the coherence length of the source, which is shown in equation 1.20. Based on this equation, the theoretical axial resolution is directly influenced by the central wavelength and the sweeping range of the swept source. However, in practical implementations, several factors can affect the effective spectral bandwidth of the detected signals, impacting the achievable axial resolution: 1) Transmission window and bandwidth limitations of the optical fiber, couplers, and lenses in the system. 2) Quantum efficiency of the photodetector. 3) Non-Gaussian spectral shape of the swept source, deviating from the ideal Gaussian profile assumed

in the theoretical equation. Moreover, if the detected signals are not linearly sampled in wavenumber (k) domain, the axial resolution will gradually degrade as the imaging depth increases. This is due to the non-linear relationship between the wavenumber and the depth position.

2. Lateral resolution: An important aspect to note regarding the lateral resolution in OCT is that it is independent of the bandwidth of the light source. Assuming a Gaussian distribution of the beam spot, the theoretical lateral resolution follows Abbe's criteria, which is given by:

$$\delta x = \sqrt{2\ln 2}\,\omega_0 = \frac{0.37\lambda_c}{\mathrm{NA}} \tag{1.24}$$

For a Gaussian beam profile, the spot size is defined as radius ω_0 of the beam waist, where the intensity drops to $1/e^2$.

3. Depth of Focus(DOF): DOF affects the imaging performance and the range over which the lateral resolution is maintained[64]. First, DOF determines the axial range over which high-quality, well-resolved images can be obtained. In applications requiring imaging over an extended depth range [65], such as retinal imaging or subsurface tissue imaging, a larger depth of focus is desirable to maintain consistent lateral resolution throughout the imaging depth. Second, DOF also impacts the signal sensitivity and SNR of the OCT system. Within the DOF, the signal is more concentrated, resulting in higher sensitivity and better SNR. Beyond the DOF, the signal becomes more dispersed, leading to a gradual decrease in sensitivity and SNR with increasing depth.

The theoretical value of DOF is given by the following formula [66]:

$$\mathrm{DOF} = \frac{2\pi \cdot n}{\lambda_c}\omega_0^2 = \frac{2n\lambda_c}{\pi \cdot \mathrm{NA}^2} \tag{1.25}$$

Since both DOF and lateral resolution are proportional to the central wavelength and inversely proportional to the numerical aperture of the objective, there is a trade-off between the choices of higher lateral resolution and higher DOF [66].

4. Total Measurement Range: The imaging depth of OCT is primarily limited by the depth of penetration of the light source in the sample. Additionally, in SS-OCT, the depth is limited by the number of sample points N during the wavelength sweeping over the bandwidth. As previously mentioned, the image in SS-OCT is obtained after Fourier transformation of the captured interference data. The total length or depth after Fourier transform is limited by the sampling rate of the spectral data, and is governed by the Nyquist theorem. The maximum imaging depth achievable in SS-OCT is:

$$z_{\max} = \frac{1}{4}\frac{\lambda_0^2}{\Delta\lambda}N \tag{1.26}$$

where N is also equal to the digitizer sampling rate/laser sweep rate.

1.4 Summary

In the first chapter, we provide an overview of the current 3D imaging techniques in biomedical applications. Then the first section introduced the basic theory and principle of confocal microscopy and extended further to Chromatic confocal microscopy. The second

section discussed the principles, imaging theory and key performance metrics of OCT. Three types of OCT, including time-domain, spectral domain and swept source OCTs, were briefly discussed.

Chapter 2 covers the development of the DMD-based chromatic confocal microscope. It is a digital scanning chromatic confocal microscope. We will discuss the principle, setup of the system, system calibration, experiment results, and modeling of an improved DMD-based chromatic confocal microscope with freeform prisms.

Chapter 3 covers the development of the MicroLED-based chromatic confocal microscope. It has a similar principle and scanning strategy as the DMD-based one. We will discuss the advantages of using MicroLED and its limitations.

Chapter 4 focuses on the designs of the hyperchromatic confocal objectives. We will present three different hyperchromatic objective lenses with specific application scenarios and specs.

Chapter 5 presents the development of a multimodal intraoral screening system for oral cancer. We will demonstrate the system-building procedures, including optical design, mechanical design, SS-OCT setup, software design and final system integration and packaging.

Chapter 6 concludes the dissertation with a summary and potential future directions.

Chapter 2

DMD-based Chromatic Confocal Microscope

In the conventional confocal systems, mechanical point-by-point scanning in three directions to realize the 3D structure reconstruction, and the system is not only complex and bulky, but also slow in image acquisition. Numerous efforts have been made to enhance the speed of confocal imaging systems. Traditional methods, such as polygon scanners [67, 68]and spinning-disk systems [69, 70], enable high-speed lateral scanning of the sample, while axial scanning is achieved through separate mechanisms. In recent years, new lateral scanning devices, like microelectromechanical systems (MEMS) scanners [71] and fiber scanners [72], have been developed to reduce the size and complexity of the scanning apparatus, although they still lack axial scanning capabilities. Similar to the spinning-disk approach, various multipoint scanning methods have been developed to increase imaging speed. These include the use of slit apertures [37], pinhole arrays [73], liquid crystal displays (LCDs) [74], and digital micromirror devices (DMDs) [75, 76, 77] for parallel acquisition of multiple focal points simultaneously. To improve axial scanning speed, several techniques have been explored, including piezoelectric objective scanners, tunable lenses, and deformable mirrors. These devices enable rapid and precise adjustment of the focal plane, allowing for sequential imaging of the sample at different depths along the axial dimension. By combining

advancements in lateral and axial scanning technologies, researchers aim to develop confocal imaging systems that offer higher acquisition rates, reduced complexity, and improved overall performance, enabling more efficient and detailed exploration of three-dimensional structures.

Chromatic confocal technique was developed to obtain depth information simultaneously [37, 78]. In the chromatic confocal system, the objective is specially designed to introduce large axial chromatic aberration so that different wavelengths are focused at different depths. The key advantage of chromatic confocal imaging is that the surface and internal structural information at each point can be obtained simultaneously by measuring the peak locations of the calibrated spectrum obtained from a spectrometer, without axial scanning. Some chromatic confocal approaches employ the DMD as point source array [34,35] or pinhole array [36] to realize fast, no-mechanical two-dimensional (2D) scanning.

In this chapter, we propose a compact DMD-based chromatic confocal microscopy for 3D imaging without any mechanical scanning. The lateral scanning is enabled by DMD, which is used as the point source array and pinhole array, and the depth scanning is achieved by the chromatic confocal technique. The principle and system setup of the proposed system will be discussed in Section 2.1. In the proposed configuration, the micromirror array is not perpendicular to the confocal imaging axis. This potential limitation and proposed solution will be discussed in Section 2.1. The system demonstration will be discussed in Section 4.

2.1 Principle of the DMD-based Chromatic Confocal System

2.1.1 DMD-based Chromatic Confocal Model

The DMD-based chromatic confocal system is based on a 4f confocal configuration. The unfolded chromatic confocal model is shown in Figure 2.1.

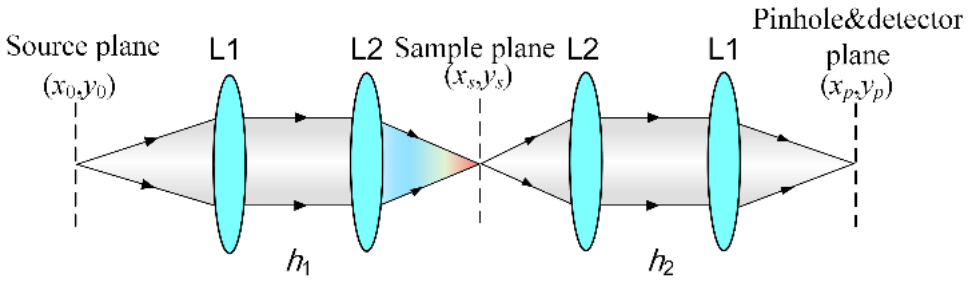

Figure 2.1: Unfolded configuration of chromatic confocal microscopy. L1 is the tube lens, and L2 is the microscope objective with chromatic aberrations.

.

Considering the beam with wavelength λ, the point spread functions of the illumination system $h_1(x, y, z, \lambda)$ and detection system $h_2(x, y, z, \lambda)$ are [20]:

$$\begin{cases} h_1(x,y,z,\lambda) = \iint P(x,y) \exp\left[\dfrac{j\pi(x^2+y^2)}{\lambda f_2^2}\right] \exp\left\{-\dfrac{j2\pi}{\lambda} W(x,y,\lambda)\right\} \\ \qquad\qquad \times \exp\left[-\dfrac{j2\pi}{f_2}(xx_o + yy_o)\right] dx\, dy \\ h_2(x,y,z,\lambda) = \iint P(x,y) \exp\left[\dfrac{j\pi(x^2+y^2)}{\lambda f_2^2}\right] \exp\left\{-\dfrac{j2\pi}{\lambda} W(x,y,\lambda)\right\} \\ \qquad\qquad \times \exp\left[-\dfrac{j2\pi}{f_1}(xx_s + yy_s)\right] dx\, dy \end{cases} \tag{2.1}$$

where $P(x, y)$ is the common pupil function, f_1 and f_2 are the focal lengths of L1 and L2, respectively, and $W(x, y, \lambda)$ is the aberration of the whole system. In the chromatic confocal system, the remaining aberration is the longitudinal chromatic aberration. Based on the

convolution of the field in the sample plane with the point spread function of the reversed system, the irradiance in the pinhole is given by [79]:

$$I_p\left(x_p, y_p, x_s, y_s, z\right) = \int_\lambda S(\lambda) \left| \iint h_1\left(x_0, y_0, z, \lambda\right) O\left(x_0 - x_s, y_0 - y_s, z, \lambda\right) h_2\left(\frac{x_p}{M} - x_0, \frac{y_p}{M} - y_0, z, \lambda\right) \mathrm{d}x_0 \mathrm{d}y_0 \right|^2 \mathrm{d}\lambda. \tag{2.2}$$

The $S(\lambda)$ is the normalized spectrum function, and $O(x, y, z, \lambda)$ is the interaction function of light with the measurement sample. The key characteristic of confocal imaging is to use a pinhole placed in front of the detector to block the out-of-focus light [80]. The irradiance I_{det} on the detector plane is given by

$$I_{\mathrm{det}}\left(x_p, y_p, x_s, y_s, z\right) = \iint I_p\left(x_p, y_p, x_s, y_s, z\right) \mathrm{d}x_p \mathrm{d}y_p. \tag{2.3}$$

According to equations 2.2 and 2.3, Figure 2.2 shows the simulation results of the detected normalized irradiance distribution when the object is at different axial positions. In the simulation, the object is a perfect plane mirror, which means $O(x, y, z, \lambda)$ is set as 1 in the unfolded system. The focal lengths of L1 and L2 are 90 mm and 16 mm, respectively, and the pinhole is a square 7.6×7.6μm pinhole, which is the pixel size of the micromirror in DMD.$S(\lambda)$ is the calibrated normalized spectrum, which is shown in Figure 2.7 of Section 2.2.1.

The vertical cross-section at each axial position in Figure 2.2(a) and (b) refers to the irradiance contribution of different wavelengths. Figure 2.2(c) plots the cross section at the axial position of 0.0 μm with a square pinhole, showing the dominated wavelength is 0.58

μm at the corresponding axial position. The horizontal cross-section at each wavelength in Figure 2.2(a) and (b) refers to its corresponding axial response curve. Figure 2.3 plots the axial response curve of the spectrum at 580 nm, showing the irradiance distribution of the light along the axis position. As a comparison, the distributions with circular apertures and without pinhole are plotted as well.

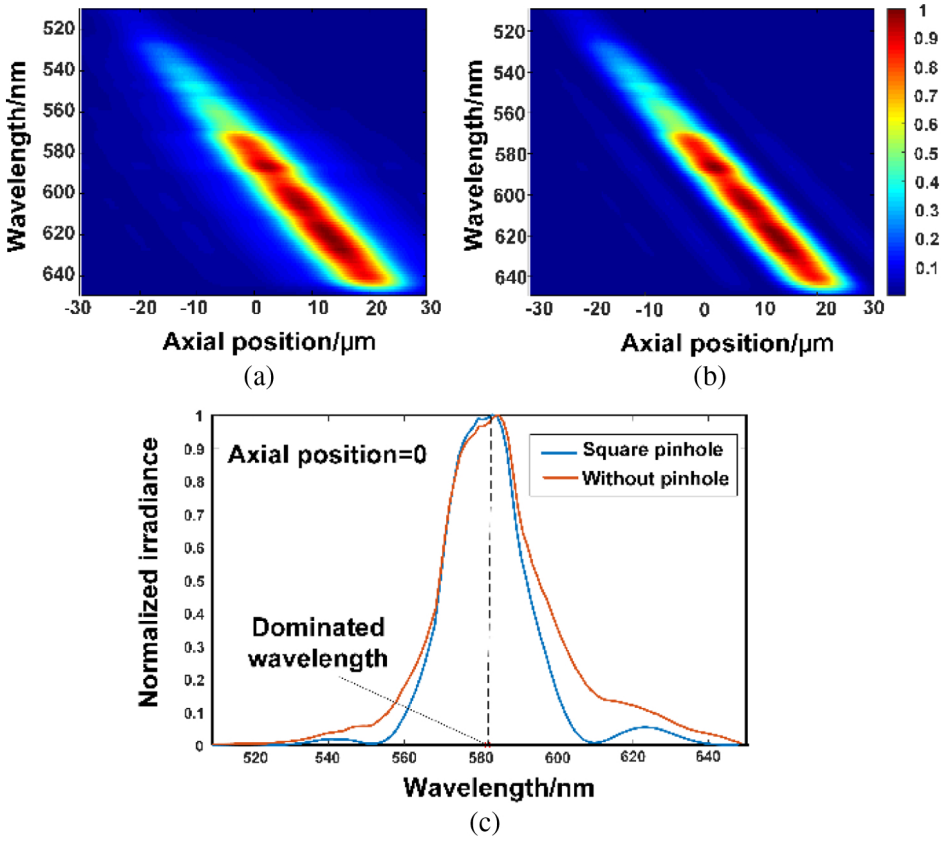

Figure 2.2: Normalized simulated irradiance distribution when the object is at different axial positions: (a) without and (b) with detection pinhole; (c) irradiance contribution of spectrum at the axial position of 0.0 μm.

.

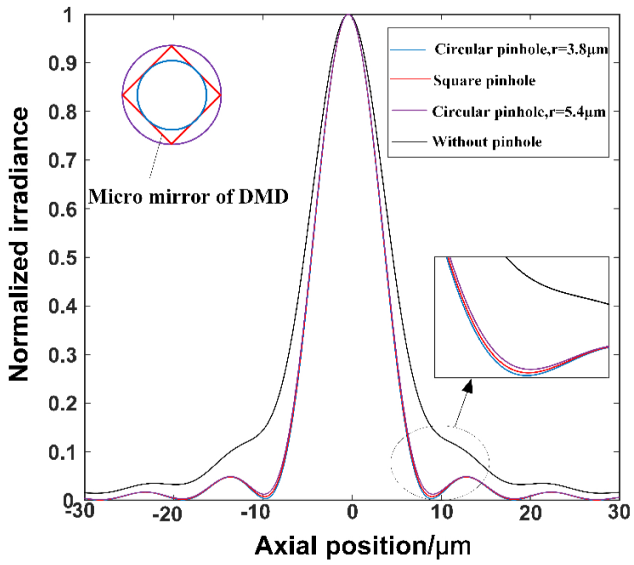

Figure 2.3: Irradiance distributions of the focused 580 nm light along the axis without pinhole and with square and circular pinholes.

.

2.1.2 System Setup

The schematic diagram of the chromatic confocal system is shown in Figure 2.4. A wideband plasma lamp with a 450–650 nm bandpass filter (Semrock, FF01-550/200-25) is used as the light source. The light passes through an integrating bar and becomes a uniform rectangular distribution. Lens L1 (Thorlabs AC254-050-C, focal length=50mm) images the output surface of the integrating bar onto the DMD surface, illuminating the micromirror array uniformly. The polarization beam splitter (PBS) is used to separate the illumination light and the signal reflected from the sample, and remove specularly reflected light from the window, micromirror, and internal structure in DMD. A folding mirror is used to redirect the reflected light from DMD to the objective with residual chromatic aberration. Due to the working principle of DMD, the incoming illumination light and the outgoing modulated reflected light form an angle of 2 times of the tilt angle of the micromirror, which is 12 deg

for the DMD used in the system. Therefore, the DMD is not perpendicular to the optical axis of the objective. The reflected light from the ON pixels (as the point sources) in DMD is first collimated by the tube lens L2 (Singlet, focal length=90mm) and then focused by the objective (Meiji MA623 10x Plan Achromat Objective) to a tilted plane, according to the Scheimpflug principle [81]. A quarter-wave plate is used to convert the linear polarized light from the DMD to circular polarized light and also to convert the circular polarized light reflected from the sample to orthogonal linear polarized light.

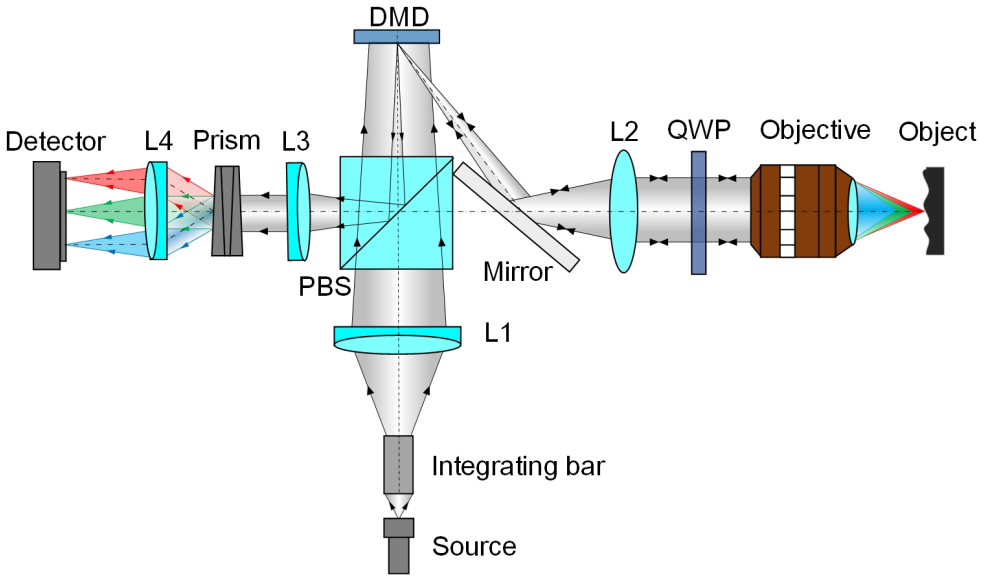

Figure 2.4: Schematic diagram of the DMD-based chromatic confocal microscope. L1–L4, lenses; DMD, digital micromirror device; PBS, polarization beam splitter; and QWP, quarter-wave plate.

.

Owing to the residual chromatic aberration from the tube lens L2 and the microscope objective, the light with different wavelengths is focused to different depths. Light reflected from the object is first collected by the objective and then imaged onto the DMD by lens L2. The ON pixels will work as the pinholes and reflect the light from the focal point to the imaging path. After passing through the quarter-wave plate twice, the reflected light from

the object turns to s-polarized light and is reflected by the PBS to the detector. On the other hand, the light directly reflected from the window, OFF pixels, and internal structure in the DMD remains p-polarized light and transmits through the PBS. The signal light from ON pixels in the DMD is first collimated by lens L3 (Thorlabs AC254-075-C, focal length=75mm) and then dispersed into different directions by a custom-made dispersion prism. Light with different wavelengths is focused onto different lateral positions in the monochromatic detector camera (FLIR, BFS-U3-51S5M-C, 2448×2048 pixel resolution, 3.5 µm pixel pitch) by lens L4 (Doublet, focal length=105mm). The depth information of each corresponding point on the object can be obtained by finding the peak location of the calibrated spectrum. 3D information of the object can be obtained by scanning the ON pixels across the entire object.

2.1.3 Scanning Method

To maximize the imaging speed, an array of micromirrors is turned ON at the same time. The pattern of the ON pixels is optimized in consideration of image contrast, imaging speed, and spectral resolution. The pattern of ON pixels will scan across the entire DMD to obtain 3D information of the object.

In our demonstration, DLP3000 DLP 0.3 WVGA Series 220 with a frame rate of 60 Hz is used. The DMD consists of 608×684 pixels (7.6×7.6µm). Each pixel represents a single point source and detection pinhole. Figure 2.5 shows the pattern of ON pixels used in the experiment and the corresponding detected spectrum. The gap between ON pixels in the x direction is determined by the spectral resolution. The larger the gap is, the more pixels in the detector that can be used to improve the spectral resolution, but the imaging speed is

lower. The gap in the y direction is limited by the image contrast. The gap cannot be too small for fast imaging because the image contrast will be degraded due to the cross-talk.

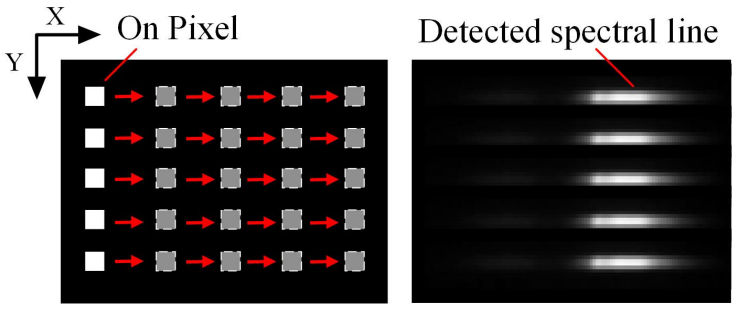

Figure 2.5: Schematic diagram of the DMD-based chromatic confocal microscope. L1–L4, lenses; DMD, digital micromirror device; PBS, polarization beam splitter; and QWP, quarter-wave plate.

.

2.2 System Calibration

2.2.1 Spectrum Normalization

In our experiment, we use a plasma lamp as the light source and a bandpass filter to limit the working spectrum. A single-point source will generate a spectral line in the detector. In general, the length (pixel) of the spectral line is determined by the spectrum of the light source, the dispersion prism, and the focal length of the imaging lens. The spectrum of the light source, transmissions of the optical system over different wavelengths, and quantum efficiency of the detector determine the irradiance distribution of the detected spectral line. Since the depth information is extracted from the peak location of the calibrated spectrum, it is necessary to normalize the spectrum first. As shown in Figure 2.6, the pixel position in the detected spectral line represents the wavelength, and the gray value means the irradiance. As the first step in calibration, a set of bandpass filters with 10 nm bandwidth is placed in

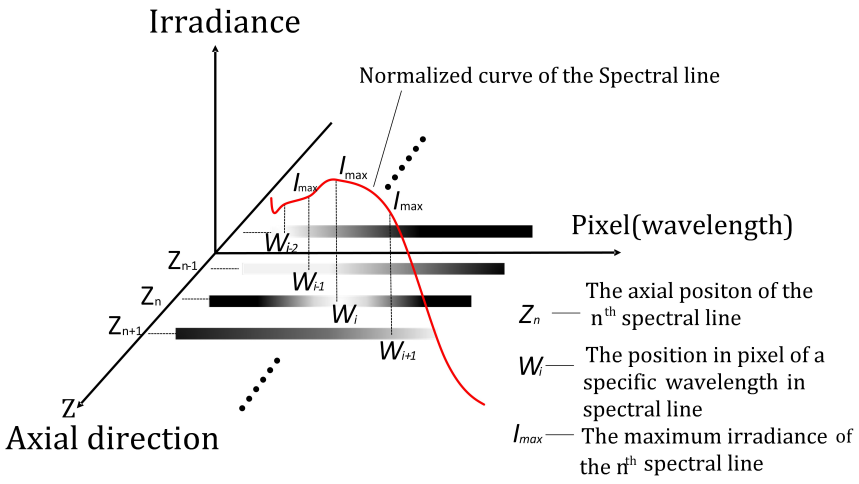

Figure 2.6: Calibration method for the detected spectrum.

.

front of the light source to calibrate the pixel location of the corresponding wavelength in the detected spectral line. To calibrate the detected spectrum, we place a mirror on the object plane and open the pixel in the center of the DMD, which will generate a single spectral line in the camera. Driving the mirror to move in the axial direction and recording images of the spectral line continually, we could find the maximum irradiance I_{max} for each pixel position W_i. By normalizing the detected irradiance and corresponding pixel location and wavelength, we can obtain the normalized spectrum (Figure 2.7), which considers the light source spectrum, the transmission of the optical system, and the quantum efficiency of the detection. The normalized spectrum for the full field can be obtained by turning on all pixels sequentially and performing the same measurement.

In the experiment, we only use the spectrum between 505 and 650 nm, and the spectrum covers 110 pixels. The reason is that light irradiance lower than 500 nm is relatively low as shown in Figure 2.7. Normalizing with small intensities would dramatically amplify the noise.

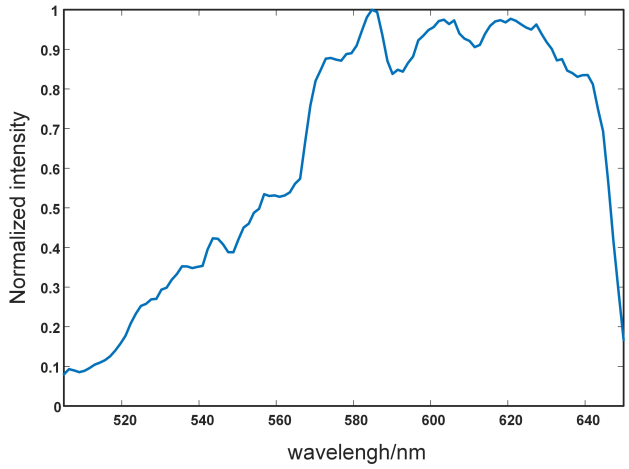

Figure 2.7: Normalized detected spectrum of the central pixel in the DMD.

.

2.2.2 Chromatic Shift and Spectrum Calibration

Measurement range and the relationship between the axial position of the object and the detected spectrum in the sensor are two critical factors in depth measurement. Chromatic confocal microscopy measures the depth through chromatic shift, and the chromatic shift is characterized by the position of the pixel with the maximum normalized irradiance in the detected spectral line. Thus, a relationship between the imaging depth and the pixel location of the spectral line needs to be established.

To establish the relationship between the imaging depth and the corresponding detected spectrum, similar to the process for obtaining the normalized spectrum, we use a flat mirror as the object and scan it through the focus. For each position, we take an image and identify the pixel with the highest normalized irradiance. We can then establish the relationship between the mirror position (imaging depth) and the pixel location Z_n. Figure 2.8 plots the

relationship between the imaging depth and the peak spectrum, which is obtained from the central DMD pixel.

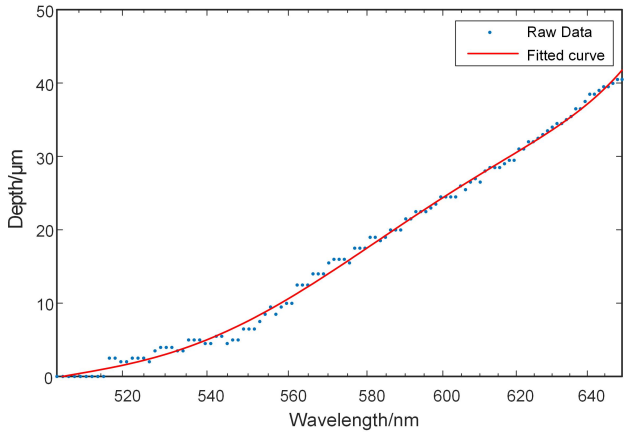

Figure 2.8: Relationship between the axial position of the object and peak of the detected spectrum.

.

2.2.3 Surface Calibration

The optical path of the confocal illumination and detection for the DMD-based confocal system is shown in Figure 2.9. Since the micromirror of the DMD rotates by 12° when it is in ON state, the illumination plane (DMD plane) is tilted by 24°, not perpendicular, to the unfolded optical path as the conventional imaging system. Thus, the corresponding imaging plane is tilted as well.

As shown in Figure 2.9, the width of the DMD is 6.5 mm, and it is at an angle of 24° to the plane perpendicular to the optical axis. The edge offset of the DMD on the optical axis is $d_z = 2.64$ mm, and the projection width of the DMD is $h = 5.94$ mm. The tilt angle

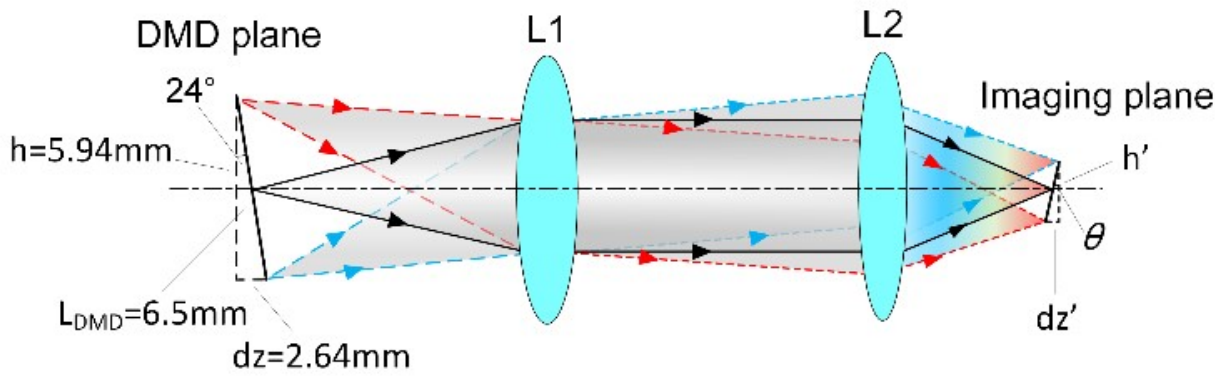

Figure 2.9: Schematic diagram of the confocal optical path under Scheimpflug angle condition.

.

θ of the imaging plane can be calculated by

$$\begin{cases} \tan\theta = m \times \tan 24^\circ \\ m = \frac{f_2}{f_1} \end{cases}, \tag{2.4}$$

where m is the magnification of the system, and f_1 and f_2 are the focal lengths of L1 and L2, respectively. In the experiment setup, f_1 is 90 mm, and f_2 is 16 mm, so the tilt angle θ is 4.53°, meaning the imaging plane is tilted 4.53°. Therefore, a surface calibration is needed to construct the 3D surface correctly. We use a flat mirror to map the slanted plane. The reference plane (Fig. 10) can be fitted from the raw data and saved as $H_{ref}(x, y)$, where x, and y are the coordinates in the x and y directions, respectively. Since the system is telecentric on both sides, the final surface profile data $H(x, y)$ can be obtained by

$$H(x, y) = H_{\text{obj}}(x, y) - H_{\text{ref}}(x, y), \tag{2.5}$$

where $H_{obj}(x, y)$ is the raw surface data extracted from the spectral line.

Based on the best-fitted surface equation in Figure 2.10, the normal vector of the reference plane is (-0.003789, 0.0827, 1). The actual tilt angle θ can be calculated as 4.73°, which is very close to the theoretical prediction.

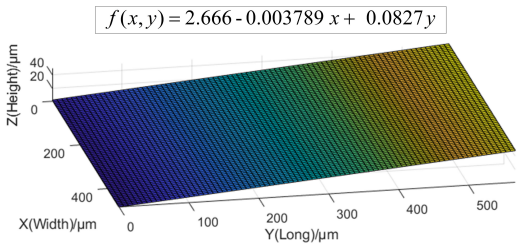

Figure 2.10: Measured reference slanted plane for the system in Figure 2.9

.

2.3 Experiment

2.3.1 System Characterization

The axial resolution of the chromatic confocal system is determined by the NA of the objective and the spectral resolution of the spectral imaging subsystem. In our system, the chromatic shift is 45 µm, and the spectral line consists of 110 pixels. The theoretical pixel spectral resolution is about 0.41 µm. The theoretical confocal lateral resolution is determined by equation 1.3. With a 0.25 NA objective, the lateral resolution is 0.81 µm at 570 nm.

A standard 1951 USAF resolution target is used to measure the lateral resolution. By scanning the resolution target with the 2 × 2 pinhole array, the confocal image is shown in Figure 2.11. Both vertical and horizontal bars in the first element in Group 9 and the

vertical bars in the second element can be resolved, and the corresponding resolution of the first element in Group 9 is 0.98µm.

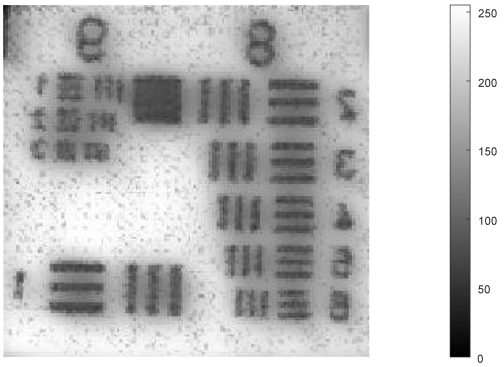

Figure 2.11: Confocal image of the standard USAF resolution target.

.

In order to obtain the axial resolution of the confocal system, an axial scanning with a flat mirror is performed with the light of 570 nm. The experimental data is shown in Figure 2.12. Based on the curve fitting analysis with a Gaussian function (red line in Figure 2.12), the confocal axial resolution Δz is determined to be 12.63 µm when it is defined as the full width at half-maximum (FWHM) in the depth profile.

2.3.2 System Demonstration

To verify the surface profiling capability of the proposed DMD-based chromatic confocal imaging system, we measure a copper multistep sample made by diamond turning machine. By turning all the pixels of the DMD on and removing the dispersion prism, the wide-field image of the step sample is captured and shown in Figure 2.13(a). Then, based on the scanning method discussed in Section 2.1.3, we turn on 80 pixels simultaneously in a single column and shift the pattern to scan the sample. With 0.05 ms exposure time of camera, the full field image can be obtained in 8 s and is plotted in Figure 2.13(b).

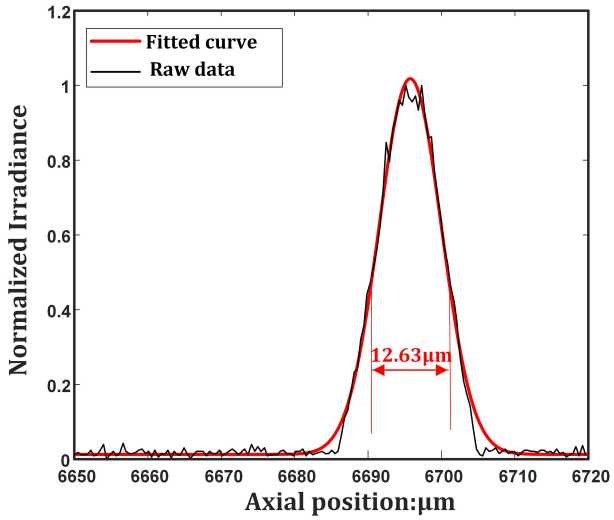

Figure 2.12: Experiment data for estimating axial resolution. System demonstration.

.

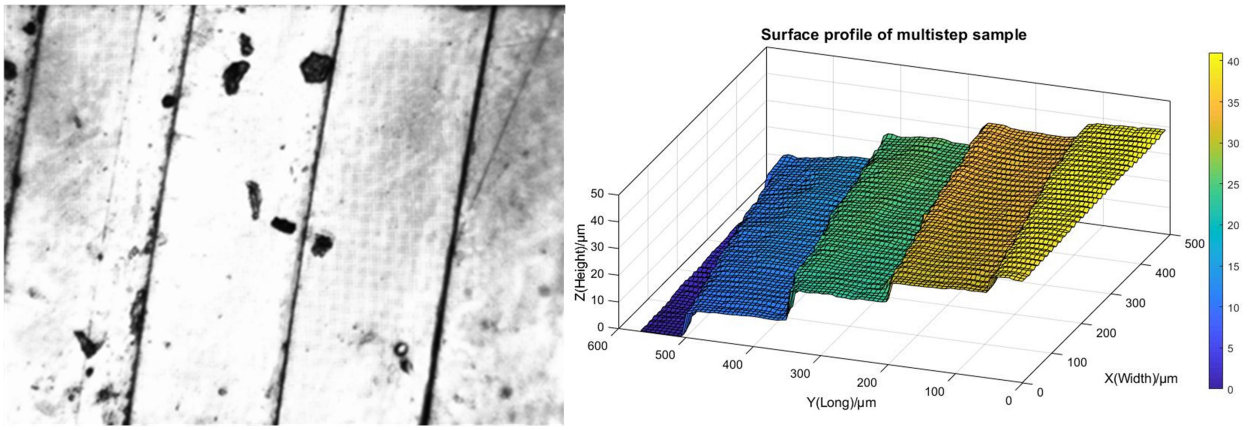

(a) (b)

Figure 2.13: Measured copper multistep sample: (a) Wide-field image and (b) surface profile.

.

We also measure the same test sample with Zygo NewView 8300 optical profilometer. Figure 2.14 compares the surface profiles from two measurements, demonstrating that the proposed system has the same performance as the white light interference microscopy. As shown in Figure 2.14, the total height of the sample is 36 µm, which contains four steps: 7 µm, 8 µm, 10 µm, and 11 µm. The standard deviation of the measured height differences for four steps is 0.039 µm. It can be seen that the cross section measured by the DMD-based system and Zygo are accordant. We determine the height of each step to be 10.01 ± 0.22 µm,10.98 ± 0.25 µm, 7.96 ± 0.23 µm, and 7.06 ± 0.22 µm. The scanning time is 8 s to get the 3D surface profile, which is restricted by the exposure time of the camera.

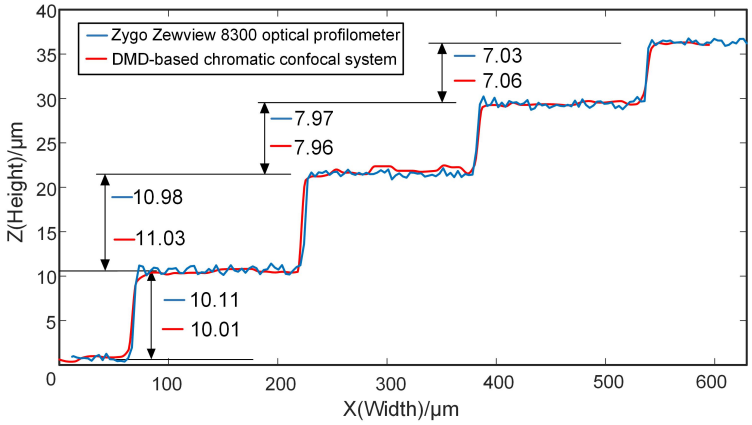

Figure 2.14: Cross-section surface profiles of the test sample by a DMDbased chromatic confocal system and Zygo NewView 8300 optical profilometer.

.

We also test the DMD-based confocal imaging to measure the surface topography of a diffuse printed circuit board (PCB). The same scanning procedure is used to obtain the surface profile of the board. The wide-field image of the surface of PCB board is shown in Figure 2.15(a), and the corresponding reconstructed surface profile with 114,660 pixels (= 390×394 pixels) is shown in Figure 2.15(b). In summary, the experiments demonstrate

the 3D imaging capability of the proposed DMD-based confocal imaging system without mechanical scanning.

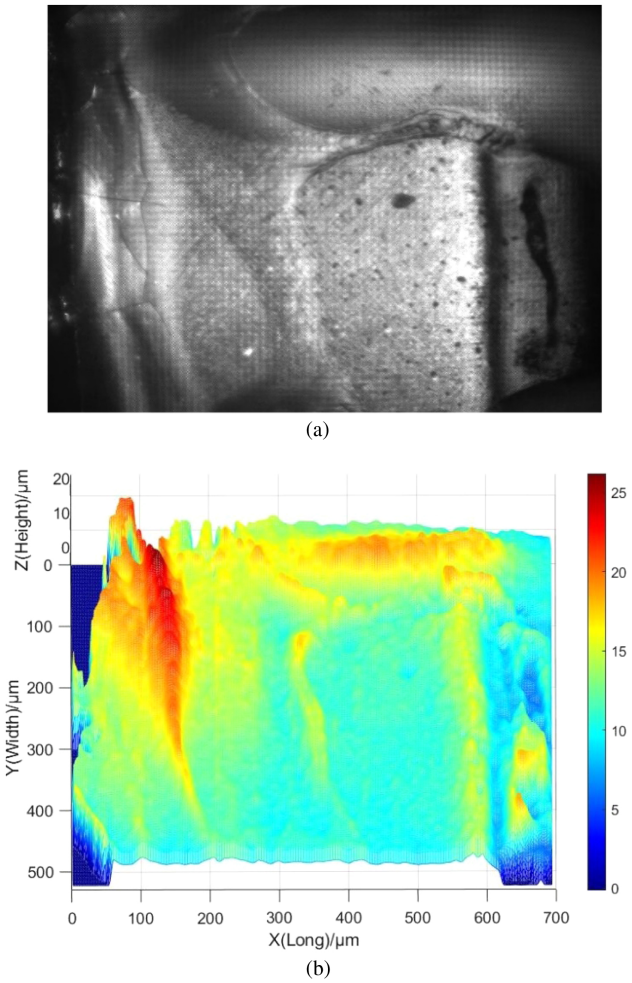

Figure 2.15: Measured surface of PCB board: (a) wide-field image and (b) surface profile.

.

2.4 Modeling of Improved DMD-based Chromatic Confocal Microscope with Freeform Prisms

Section 2.1 proposed a compact DMD-based chromatic confocal microscope for 3D imaging without any mechanical scanning [82]. The lateral scanning is enabled by DMD, and the axial scanning is achieved by the chromatic confocal technique. However, in the previous system, DMD is not perpendicular to the optical axis and thus causes a tilted imaging plane and keystone distortion [83]. The depth measurement range is short due to the small chromatic aberration and the tilted object plane.

In this section, we present an improved DMD-based chromatic confocal microscope model in LightTools. First, a designed hyperchromatic objective lens is used to increase the depth measurement range. Second, we use a group of freeform prisms to correct the tilted imaging plane and keystone distortion [84]. In addition, the prisms also provide the dispersion that the previous system needed. By doing so, the system becomes more compact and has better 3D imaging performance. LightTools can be used to model the entire system and validate the performance, which is important for guiding further research and improvement. In Section 2.4.1, the basic system configuration and working principle are briefly discussed. Section 2.4.2 shows the illumination module of the system, and Section 2.4.3 demonstrates the chromatic confocal imaging module. Then Section 2.4.4 and Section 2.4.5 focus on system validation, some simulation results are presented and analyzed to show the 3D imaging ability.

2.4.1 System Overview

Figure 2.16 shows the system layout of the improved DMD-based chromatic confocal microscope. It consists of an illumination module and a chromatic confocal imaging module. In the illumination module, a broadband light source SLS205 (240-1200nm, Thorlabs) is used to generate a collimated beam. Then an object fly's eye lens array images the source at the following field lens array. The field array reimages all of the fields with a condenser lens, so they overlap and create a uniform illuminance on the DMD plane. A beam splitter in the system is used to transmit the illumination path and reflect the spectrum imaging path simultaneously. As for the DMD panel itself, each pixel has a dimension of 7.6 µm. The micromirror of DMD rotates by 12° when it is in the on state, thus the DMD plane is tilted by 24° relative to the source plane. The on-state micromirrors of DMD redirect the light to a designed water-immersed microscope with an amount of chromatic aberration, leading the light with different wavelengths focused to different depths. Light reflected from the sample images on the DMD plane again; the on-state micromirrors will work as the pinhole array and reflect the light from the focal point to the spectrum imaging path. In the spectrum imaging path, owing to the 12° tilt of the DMD micromirror, the image of the DMD panel on the imaging plane is also a tilted plane relative to the detector plane according to the Scheimpflug principle as shown in Figure 2.9. The mismatch between the imaging plane and the detector plane can cause defocus for different fields and introduce keystone distortion. In order to solve these issues, three plane-symmetric freeform prisms are designed as a special collimator and disperser. They not only correct those aberrations but also offer dispersion ability. Therefore, the light after passing the prisms will be dispersed and imaged on the

detector plane by the imaging lens. Light with different wavelengths is focused onto different lateral positions on the detector plane.

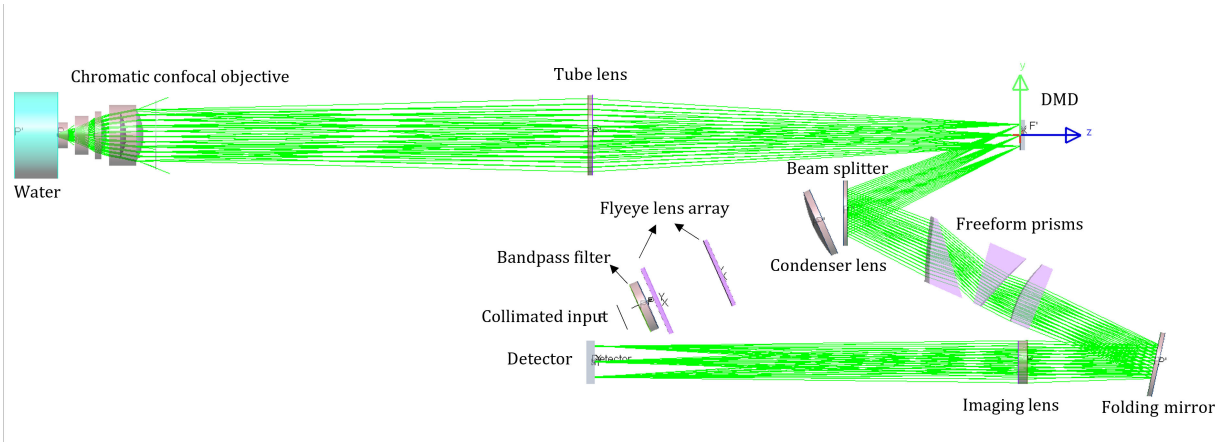

Figure 2.16: System layout of DMD-based chromatic confocal microscope.

.

In a word, a single on-state pixel on DMD, would be a point source with a broadband wavelength. It then would be a reflection pinhole and reflect the light from the position that a specific wavelength focuses on. The light would finally be a spectral line on the detector. By finding the dominant wavelength and its relative position in the calibrated spectral line, depth information can be obtained. 3D information of the sample can be obtained by scanning the on-state pixels across the entire DMD.

2.4.2 Illumination Module

The illumination path is shown in Figure 2.17. After passing the bandpass filter(450nm-650nm), the spectrum of the incoming collimated beam becomes a uniform white light from 450 nm to 650 nm. The source spectrum and filtered spectrum are shown in Figure 2.18.

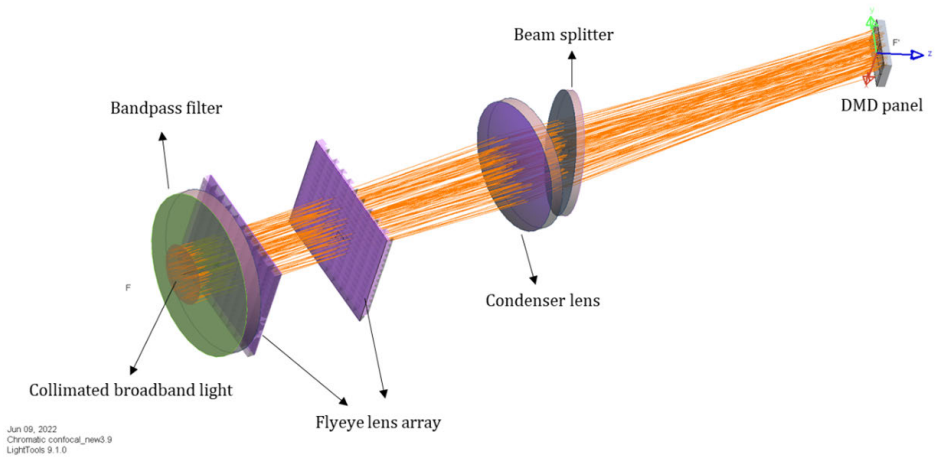

Figure 2.17: Illumination module layout.

.

The first lens array images the source at the second array. A condenser lens and the second array produce a uniform illuminance. The final irradiance on the DMD plane (effective area 6 mm×3 mm) is shown in Figure 2.19.

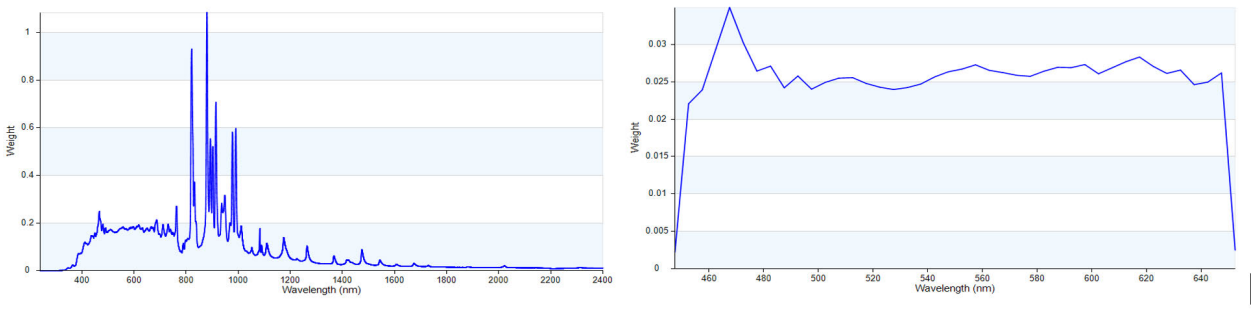

(a) (b)

Figure 2.18: The source spectrum (a) and the filtered spectrum (b) in the system.

.

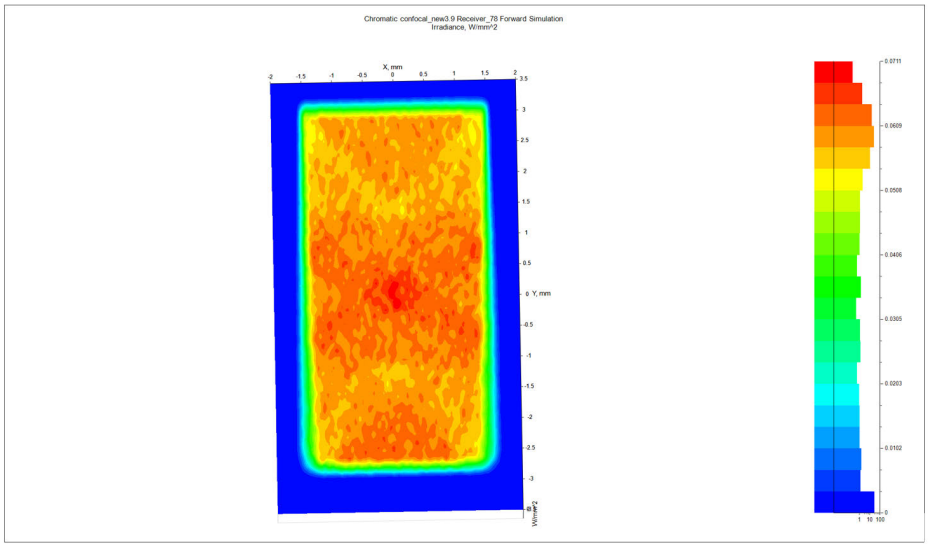

Figure 2.19: The irradiance on the DMD plane.

.

2.4.3 Chromatic Confocal Imaging Module

The objective is the key component of the chromatic confocal microscope. It is used to generate axial chromatic aberration. In this reported model, the designed objective is a water-immersed objective made of PMMA and OKP4HT. The major specification is listed in table 2.1. And the Non-sequential ray tracing result for the objective is shown in Figure 2.20 to demonstrate the chromatic shift.

In order to demonstrate the 3D imaging ability, a DMD consisting of 5 × 5 On-state mirror array is modeled in LightTools to simulate 25 different field points. Each mirror array has 3 × 3 micro-mirror pixels to work as a pinhole pixel. The pixel size is 7.6 µm × 7.6 µm. Figure 2.21 shows the modeled DMD panel by LightTools. The effective area of the DMD is 6 mm × 3 mm.

Table 2.1: Main specification of designed objective

NA (in water)	0.5
Slit	132.5
Effective focal length	11.95 mm
Wavelength	450 nm
FOV	±0.5 mm
Wavelength	450 nm∼650 nm
Chromatic shift	∼300 nm
Working distance	50 μm ∼ 350 μm

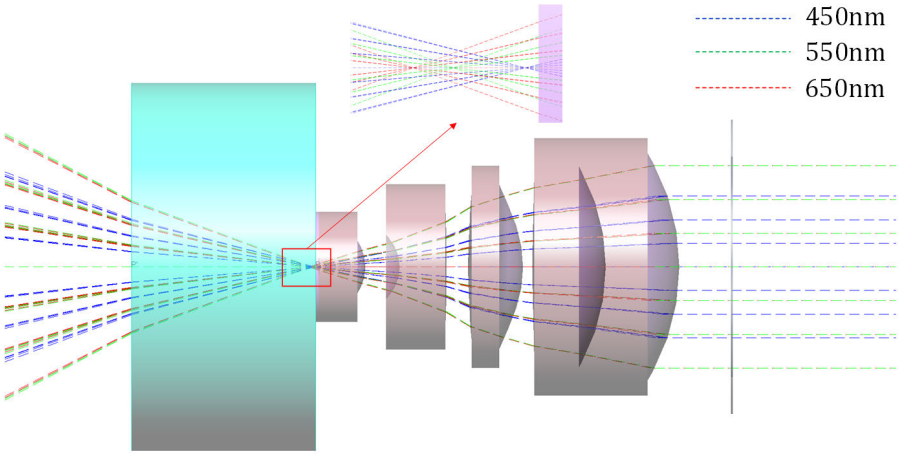

Figure 2.20: Ray tracing results of the chromatic confocal objective.

.

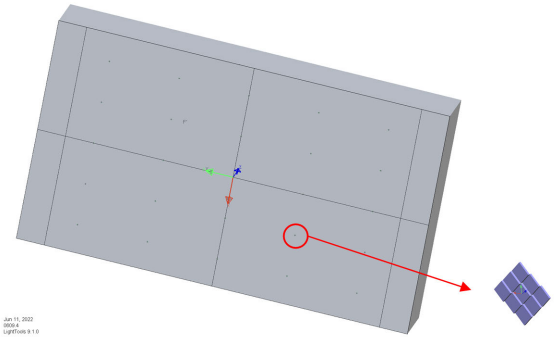

Figure 2.21: The layout of the modeled DMD and micro mirror.

.

2.4.4 Spectrum Imaging and Calibration

In our system, three plane-symmetric freeform prisms made of PMMA and OKP4HT are used to collimate the light from DMD and correct the tilted imaging plane and keystone distortion. Each of the prisms has one tilted plane surface and another plane-symmetric polynomial surface. By using two materials, we make the system only has dispersion without deviation. Therefore, 5×5 pinhole pixels will generate 5×5 spectral lines in the detector if the incoming light has multiple wavelengths. These spectral lines would be parallel along the dispersed direction(y-direction) and have the same spacing in both x and y directions. In general, the length (pixel) of the spectral line is determined by the spectrum of the incoming light, the dispersion prisms, and the focal length of the imaging lens. The spectrum distribution, transmissions of the optical system over different wavelengths, and quantum efficiency of the detector determine the irradiance distribution of the detected spectral line. To find the spectral line length and its irradiance distribution over 450nm to 650nm. Assume the light reflected by the pinhole pixel has a uniform spectrum as shown in Figure 2.18(b), the on-axis spectral line irradiance is shown in Figure 2.22. Figure 2.22(a) shows the true color distribution and Figure 2.22(b) shows the grayscale irradiance distribution.

According to Figure 2.22, the spectral line is dispersed around 1.3 mm over a 200 nm bandwidth in the detector. Moreover, the irradiance of blue light is weaker than the green and red light. The reason is the materials of the prisms have a lower transmission in the short wavelength. The cross-section of the on-axis spectral line in Figure 2.22(b) is shown in Figure 2.23, it also means the real spectrum after passing the whole system. The x-axis

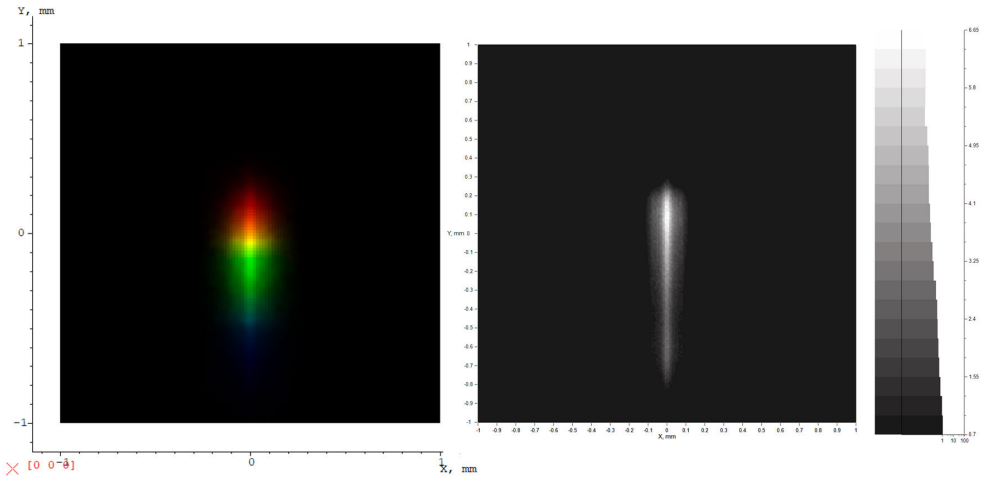

(a) (b)

Figure 2.22: Irradiance distribution of the on-axis spectral line: (a) true color chart (b) grayscale irradiance.

.

is the detector position and the y-axis means the irradiance. It's necessary to calibrate and normalize the spectrum in the real experiment based on the plot in Figure 2.23.

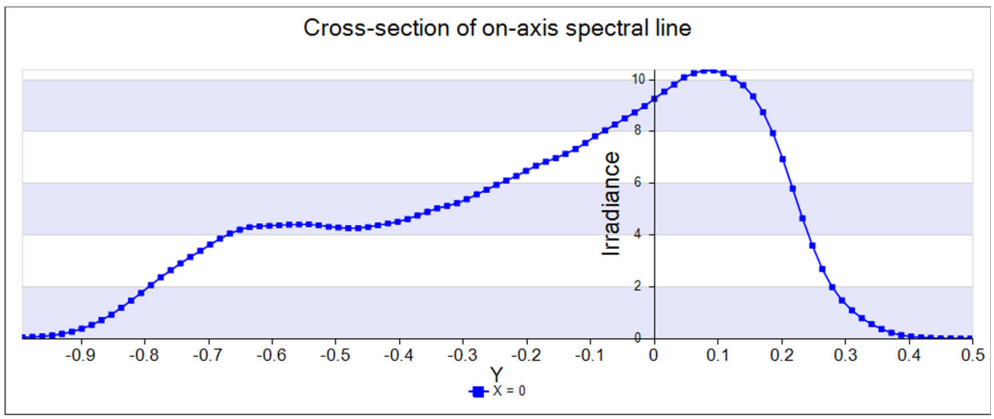

Figure 2.23: Cross-section of the real on-axis spectral line.

.

In fact, due to the confocal effect, the pinhole pixel would reflect the light from where a specific wavelength is focused on. Thus, there would be a dominant wavelength in the detected spectral line. The depth information can be extracted from the peak location of

the calibrated spectrum. To demonstrate that, three point sources are set on the sample plane B, G, R where 450nm, 550nm, and 650nm are focused. After ray tracing, the results from LightTools are shown in Figure 2.24. The rows in Figure 2.24 mean the source at different focal planes for different wavelengths. The columns in Figure 2.24 show the true color chart, grayscale irradiance, and spectral distribution, respectively.

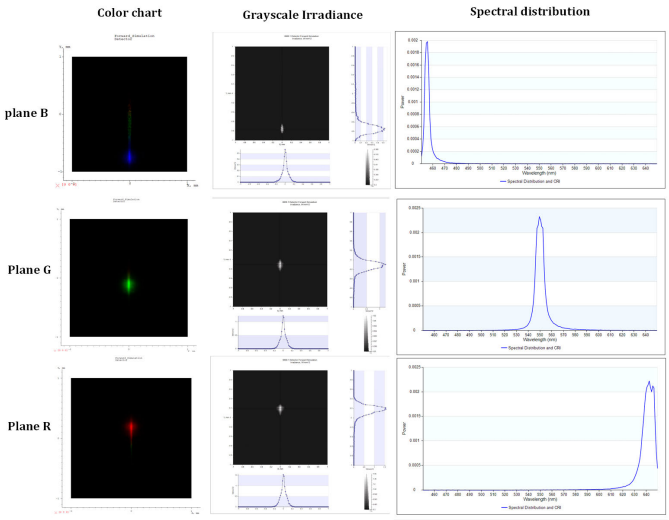

Figure 2.24: True color chart, grayscale irradiance, and spectral distribution for point source from three different sample planes.

.

The calibrated spectrum can be obtained by

$$I_{\text{cal}}(\lambda) = \frac{I_{\text{det}}(\lambda)}{I_{\text{normalized}}(\lambda) + 1} \tag{2.6}$$

Where I_{det} is detected spectrum from arbitrary sample plane,$I_{normalized}$ is the real normalized spectrum in Figure 2.23. Figure 11 shows the calibration results for the three sample planes and how to obtain their axial position. Chromatic confocal microscopy measures the depth through the chromatic shift, and chromatic shift is characterized by the position of the pixel

with the maximum normalized irradiance in the calibrated spectral line. The horizontal axis in Figure 2.25, represents the pixel location of the spectral line, wavelength, and axial position simultaneously. Thus, a relationship between the imaging depth and the pixel location of the spectral line can be established to guide the depth retrieving. For instance, in Figure 2.25, by finding the pixel location of P1, P2, and P3, we can obtain their corresponding axial position.

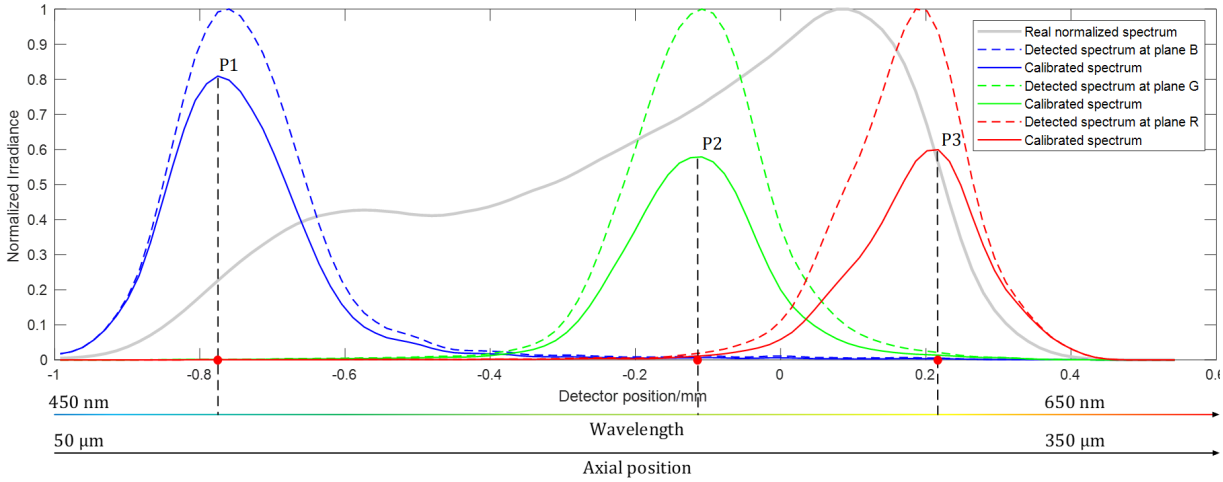

Figure 2.25: Demonstration of spectrum calibration and axial position retrieving for point source from three different sample planes.

.

2.4.5 3D Imaging Demonstration

To demonstrate the 3D imaging capabilities of the proposed system, 25 point sources that correspond to the 25 pinhole pixels as mentioned before are set in the water in LightTools. First, we set all the axial positions of the 25 point sources as the same, which means they are all located on the same flat sample plane. After tracing 5000000 rays, the color chart and irradiance distribution in the detector are shown in Figure 2.26. The white dash

box in Figure 2.26 means the spectral line length and the axial position for each field point can be obtained by finding the peak location in the calibrated spectrum as discussed. It can be seen that all of the field points have the same color and the same peak location in the spectral line, meaning they have the same axial position.

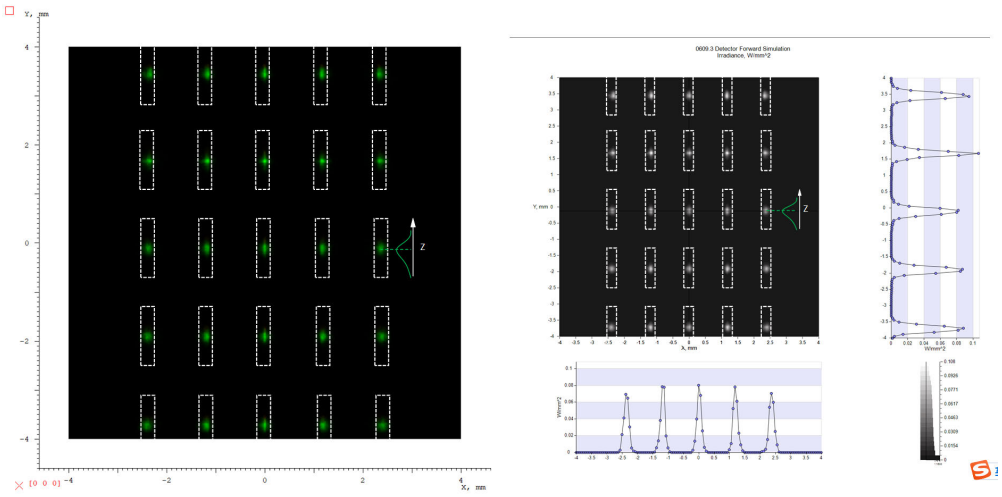

(a) (b)

Figure 2.26: Distribution of (a) color chart and (b) irradiance in the detector for a flat sample plane.

.

Furthermore, we change the axial position for each point source through MATLAB-LightTools API. Finally, we get 25 point source at 25 different axial positions as shown in Figure 2.27. After tracing 5000000 rays, the final system and its ray path are shown in Figure 2.28. The color chart and irradiance distribution in the detector are shown in Figure 2.29. In Figure 2.29, the white dash box means the spectral line length as well, and the axial position for each field point can be obtained by finding the peak location in the calibrated spectrum as discussed in section 3.2.3. It can be seen that 25 field points have different colors and peak locations in the calibrated spectrum, which means they come from different axial locations.

The accurate depths for the 25 field points can be retrieved from the relationship between the axial position and pixel location of the spectral line, which is not shown in this report. By scanning the on-state pixels across the entire DMD, we can obtain the 3D information of the sample without any mechanical scanning. However, due to the lower transmission of the short wavelengths, the irradiance for blue light is not high enough compared to green and red light. It decreases the SNR in short-depth measurements, which need to be further improved.

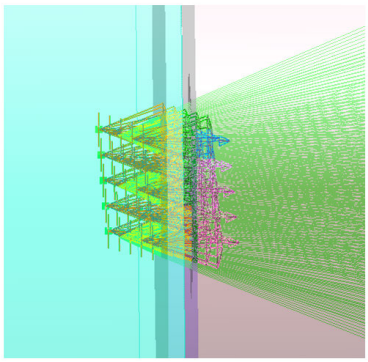

Figure 2.27: Schematic diagram of the 25 point source at 25 different axial positions. After tracing 5000000 rays, the final system and its ray path are shown in Figure 2.28.

.

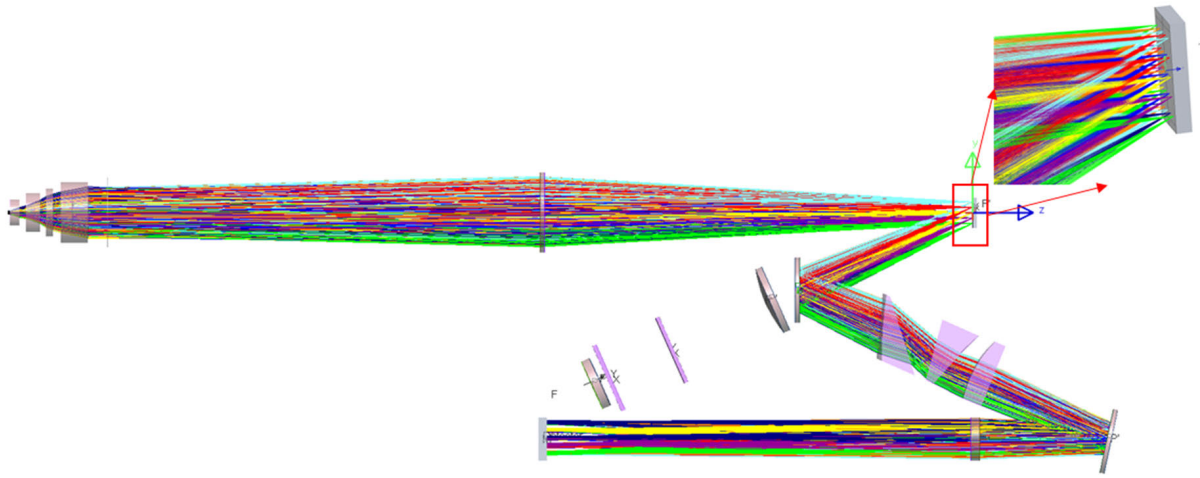

Figure 2.28: System ray path overview for 25 point source at 25 different axial positions. The color chart and irradiance distribution in the detector are shown in Figure 2.29.

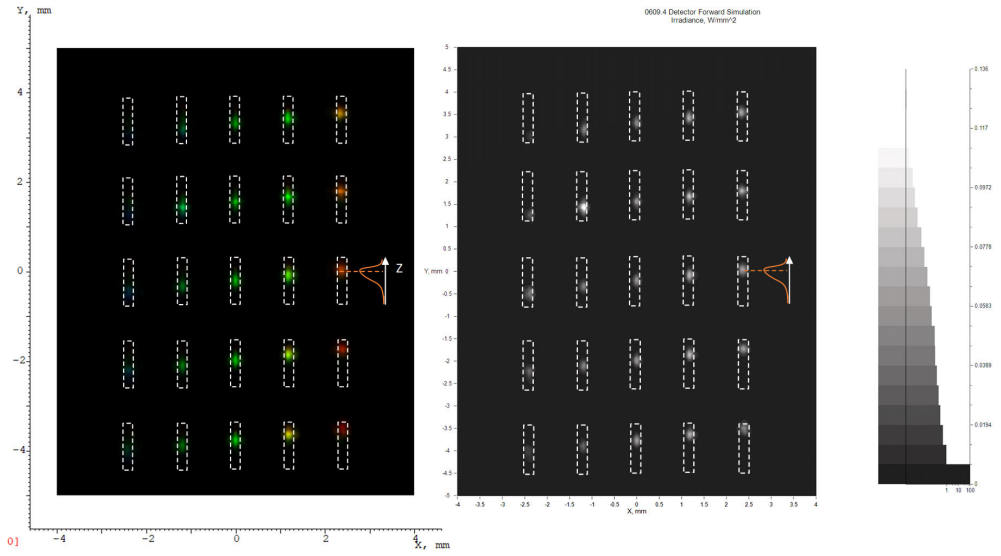

(a) (b)

Figure 2.29: Distribution of (a) color chart and (b) irradiance in the detector for a 25 different sample plane.

.

2.5 Summary and Outlook

In this chapter, we propose a compact DMD-based chromatic confocal system without moving components for surface profiling. The DMD works as the multipoint light source and detection pinhole array simultaneously. By the scanning point array pattern displayed on the DMD, lateral scanning can be achieved. Axial scanning is avoided by using residual chromatic aberrations of the microscope objective and a singlet. The measurement range of the system is 45 µm and can be increased by using the custom optical system with large chromatic aberration. However, the trade-off between the dynamic range and resolution always exists and must be carefully balanced. Since the DMD can generate patterns at rates up to 32.5 kHZ, potentially the proposed system can achieve real-time confocal measurement with a high-speed camera. Combining the freeform prisms, another improved DMD-based chromatic confocal microscope is modeled in Lighttools. The simulation results illustrate the system's working principle, calibration method, and 3D imaging capabilities. The current limitation is the material's transmission for short wavelengths, making it difficult to measure short depths. This could be improved by changing the material of the prisms. On the other hand, higher NA and larger chromatic shift objectives can be designed to further increase the 3D imaging performance.

Chapter 3

MicroLED-based Chromatic Confocal Microscope

3.1 Overview

In the previous chapter, we demonstrate a DMD-based chromatic confocal microscope for 3D imaging. The entire scanning process can be controlled digitally to avoid introducing additional mechanical scanning parts into the system. One remaining limitation of LCD- and DMD-based chromatic confocal approaches is the necessity for an external light source, which restricts the overall compactness and form factor of the system. Addressable organic light-emitting diode (OLED) and microLED panels are two potential solutions for improved system compactness and potential higher resolution. OLED shares some common properties as microLED, each pixel can emit light of a specific color independently and can be controlled independently. However, OLED has some limitations, such as low speed, low brightness, and short life time, it is not suitable for high speed measurement. In contrast, with the recent significant advances, microLED is recognized as the next-generation and ultimate display technology and is one of the fastest-growing technologies globally [85, 86]. With the potential high speed, high brightness, tunable spectrum, and small pixel, microLED is particularly suitable for high speed, compact, and low-cost confocal imaging system.

In this chapter, we propose a microLED-based chromatic confocal microscope with a virtual confocal slit for 3D imaging without any mechanical scanning or external light source. Lateral scanning is achieved by a microLED panel acting as a switchable point source array, and depth scanning is performed by the chromatic confocal technique. A virtual pinhole technique is utilized to reduce stray light interference from out-of-focus planes in object space [87]. A custom color microLED panel with a 25.6 µm pixel pitch is used to demonstrate the concept. Due to the varying intensities between the panel's red, green, and blue channels, only blue pixels are used in this Letter to demonstrate the potential of microLEDs in confocal imaging. The measured effective spectrum range is 430 to 490 nm, so the challenge is to generate relatively large axial chromatic aberration over this short 60 nm bandwidth. In this Letter, an aspherical singlet is used as the objective, since it has large axial chromatic aberration. This results in a smaller effective field of view due to the inevitable large off-axis aberrations of a singlet.

3.2 Method

3.2.1 System Setup

The proposed experimental setup is shown in Figure 3.1. Light from the microLED (pixel size, 25.6 µm; pixel number, 480×320) is first collimated by lens L1 (Thorlabs AC254-100-C, focal length=100mm). It then passes through a polarization beam splitter (PBS) and a quarter-wave plate (QWP); and finally, it is focused on the sample by an aspherical singlet objective (Thorlabs APL0609-A, focal length=9.07mm). An achromatic QWP (Thorlabs, AQWP05M-600) is used to remove the strong specular surface reflection. The lateral reso-

lution is 2.3 µm. Due to the residual chromatic aberration from the tube lens L1 and the objective, the light with different wavelengths is focused at different depths. The reflected light from the sample is first collected by the objective and then passes through the QWP to the PBS again. After passing through the QWP twice, the reflected light from the object is converted to s-polarized light and gets reflected by the PBS. A custom dispersion prism is used to disperse the reflected light in different directions, which are focused at different lateral positions on the detector camera (IDS, UI-3080SE-C-HQ, 2456×2054-pixel resolution, 3.45 µm pixel pitch) by lens L2 (Thorlabs AC254-150-A-ML, focal length=150mm). A spectral line is thus formed on the detector plane for a single illuminated point on the object. The depth information of the object can be obtained by finding the peak location of the calibrated spectrum. 3D information can be obtained from the object by scanning the ON pixels of the microLED across the entire object.

The light irradiance function of acquired signals on the detector plane without a pinhole can be described as:

$$\begin{aligned} I(x_d, y_d, x_s, y_s, z) = \int_\lambda S(\lambda) \Big| \iint h_1(x_0, y_0, z, \lambda) O(x_0 - x_s, y_0 - y_s, z, \lambda) \\ h_2\left(\frac{x_d}{M} - x_0, \frac{y_d}{M} - y_0, z, \lambda\right) \mathrm{d}x_0 \, \mathrm{d}y_0 \Big|^2 \, \mathrm{d}\lambda \end{aligned} \tag{3.1}$$

where the $S(\lambda)$ is the normalized spectrum function, $O(x, y, z, \lambda)$ is the interaction function of the light with the measurement sample, and h_1 and h_2 are the point spread functions of the illumination and detection paths. (x_o, y_o), (x_s, y_s) and (x_d, y_d) are the spatial coordinates at the source plane, sample plane, and detector plane, respectively.

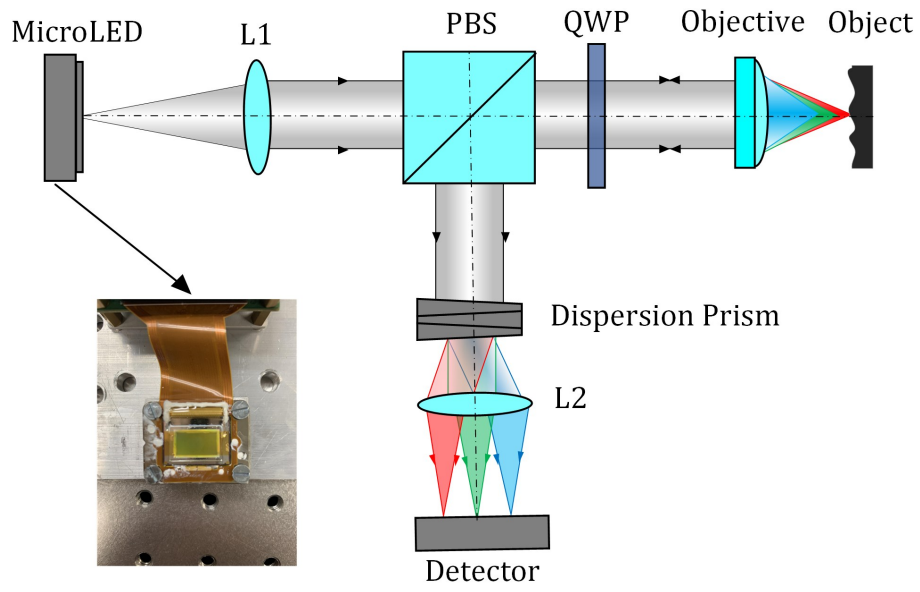

Figure 3.1: Experimental setup for the microLED-based chromatic confocal microscope. L1–L2, lens; PBS, polarization beam splitter; and QWP, quarter-wave plate.

.

Due to the dispersion of the prism, a single-pixel source will generate a spectral line in the detector plane. The length of the spectral line is determined by the spectrum of the microLED, the dispersion prism, and the focal length of the imaging lens (L2). Since the optical components in the system have different transmissions over different wavelengths, and the detector has its inherent quantum efficiency, it is necessary to calibrate and normalize the spectral line. Figure 2(a) shows the normalized spectrum of the blue microLED pixel, and Fig. 2(b) plots the relationship between the imaging depth and the peak spectrum. The total chromatic shift in the experiment is 84.4 µm over the spectrum from 430 to 490 nm. Since the spectral line covers 246 pixels on the detector, the pixel resolution for the system is estimated as 84.4µm/246pixels=0.343µm/pixel.

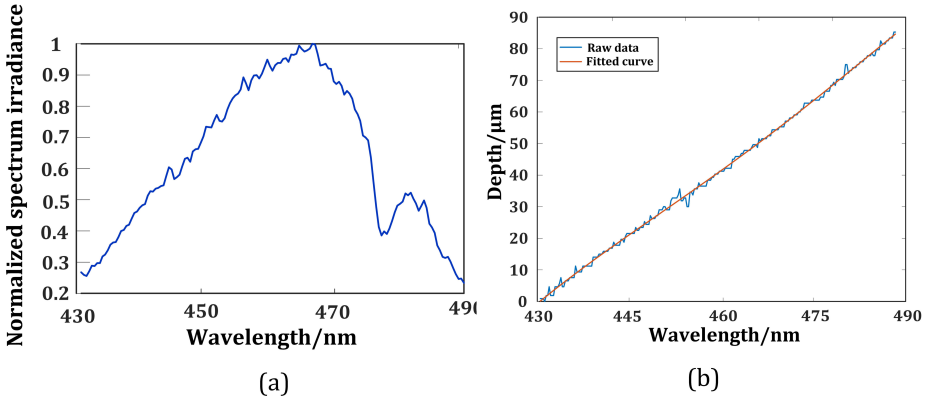

Figure 3.2: (a) Normalized detected spectrum of the central pixel in microLED, and (b) the relationship between the axial position of the object and the peak of the detected spectrum.

.

3.2.2 Virtual Pinhole Strategy

The virtual aperture is implemented in software on a host computer. It's possible, with this system, to adjust key parameters (such as effective aperture size) to optimize the image even after the basic data are acquired [88]. The proposed method employs the virtual pinhole technique to reduce out-of-focus light and improve axial resolution. The principle is to estimate the pinhole signal by numerical integration of light energy collected by the selected active pixel in the detector [87]. In the chromatic confocal method, a single point is dispersed to a spectral line on the detector. Thus, we use a rectangular digital pinhole (slit) to cover each spectral line. The axial position of the measured point can be obtained by locating the peak of the normalized spectrum across the spectral line. According to the principle of confocal microscopy, the axial resolution and image contrast are optimal when the pinhole size is similar to or slightly smaller than the size of the Airy spot. In our system, the pitch of the microLED array is 25.6 μm. The diffraction-limited spot size w_s in the detector plane is ∼38 μm based on the system magnification. Hence, the width of the

virtual pinhole w_p can be normalized by the calculated diffraction-limited spot size w_s. The detected normalized virtual pinhole energy is given by [89]

$$I_d(y_d) = \frac{\int_{-\frac{w_p}{2}}^{\frac{w_p}{2}} I(y_d)\mathrm{d}y_d}{\int_{-\frac{w_s}{2}}^{\frac{w_s}{2}} I(y_d)\mathrm{d}y_d}. \tag{3.2}$$

Figure 3.3 plots the normalized detected spectral line for different virtual pinhole sizes (the number of pixels in the detector) for a flat mirror. The pinhole size has a direct impact on the depth resolution [90]. To test the impact of pinhole size on the accuracy of our system, we axially scanned the flat mirror and estimated the depth when imaging with different virtual pinhole sizes. The standard deviations of the differences between measured depths and actual positions at 160 different axial positions are shown in Figure 3.4. This demonstrates that a pinhole size of 11 pixels, which corresponds to 38 µm, has the best performance.

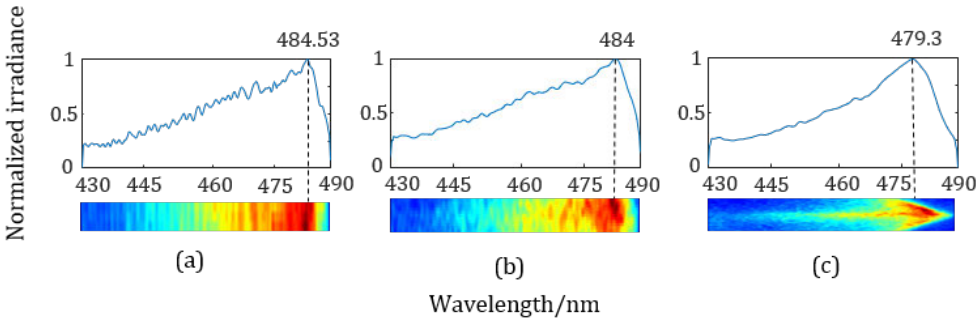

Figure 3.3: Normalized spectrum peak location for different virtual pinhole sizes: (a) three pixels, (b) 11 pixels, and (c) 101 pixels.

.

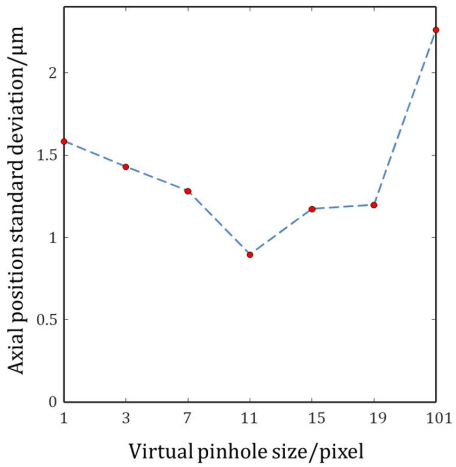

Figure 3.4: The standard deviation of the difference between measured depth and actual position for different virtual pinhole sizes.

.

3.3 Experiments

To acquire a 3D image using the microLED-based chromatic confocal imaging system, a strategy similar to the method discussed in Section 2.3 is employed., the strategy is similar to the method discussed in section [**C2S4**]. Since the detailed calibration method and experimental steps have already been discussed previously, here is a brief summary of the experimental process.The acquisition of a 3D image involves the generation of a series of pixel-array patterns that collectively cover the entire scanning region to achieve lateral scanning. During the exposure of each microLED pattern, a corresponding chromatic confocal image stack is recorded. Crucially, the pattern of ON pixels is carefully optimized to strike a balance among three key factors: image contrast, imaging speed, and spectral resolution. In the demonstration, the on-pixel pattern contains 80 $\times$ 72 pixels. Figure 4.1 shows an example of the scanning pattern. The pitches in x- and y- directions are determined by the spectral resolution and the image contrast, respectively.

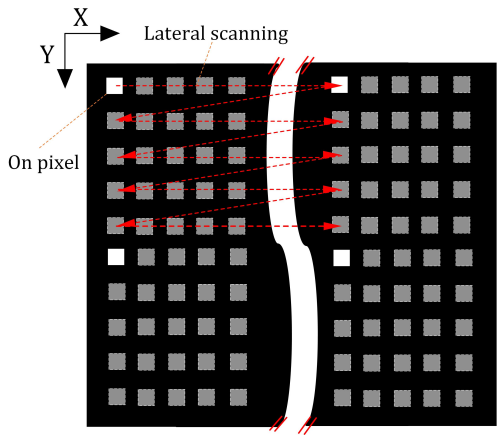

Figure 3.5: Schematic pattern of the scanning microLED array.

.

To verify the profile measurement performance, a diamond-turned copper step sample with an 8 µm step is measured by changing the scanning pattern in an orderly manner and applying the virtual pinhole detection method. The reconstructed 3D profile and corresponding cross-sectional plots are shown in Figure 3.6 and Figure 3.7 The virtual pinhole size is set at 11 pixels as optimized above. The scanning area is 186×167µm based on the magnification of the system. As shown in Figure 3.7, the measured height of the sample is 8.025 µm with a standard deviation of 0.055 µm.

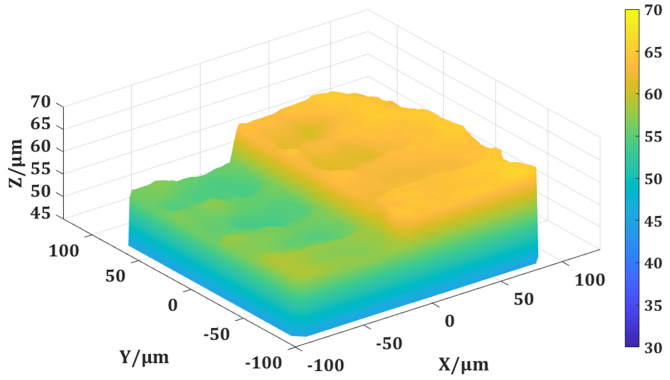

Figure 3.6: Reconstructed 3D profile of the 8 µm step sample.

.

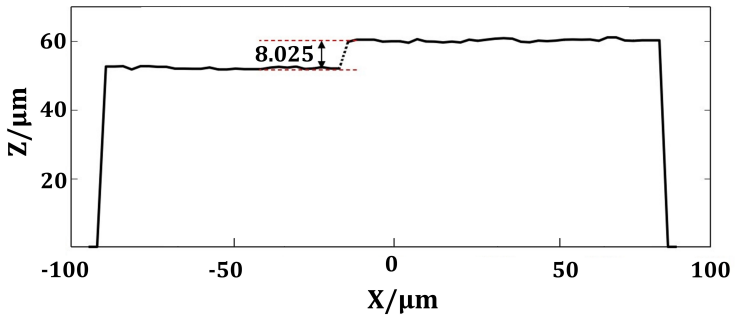

Figure 3.7: Cross-sectional surface profile of the 8 µm step sample.

.

To demonstrate the potential application of the proposed microLED chromatic confocal microscope, we also measured an onion epidermis with a microLED array that has a brightness of 1.6×106 nits. Figure 3.8(a) shows a reconstructed image of the onion epidermis, and Figure 3.8(b) shows the volume image. This experiment further demonstrates the 3D imaging capability of the proposed confocal imaging system without any moving components.

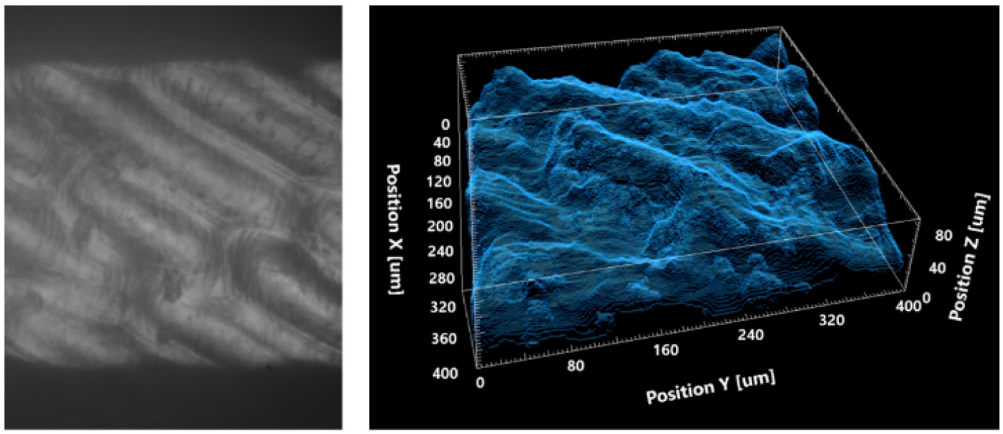

(a) (b)

Figure 3.8: (a) Reconstructed 3D image of an onion epidermis and (b) its volume image.

.

3.4 Summary

In this chapter, a new confocal imaging method based on microLED illumination is introduced and demonstrated. The advantages include (1) the entire scanning process is controlled digitally without any moving mechanical parts, (2) no external light source is needed, and (3) the system is compact and low in cost.

There are several limitations associated with the current chromatic confocal system due to the specifications of the employed microLED panel. Firstly, the pixel size of the microLED panel is not sufficiently small, imposing constraints on the achievable lateral resolution. Secondly, the spectral characteristics of the current microLED are primarily optimized for color display applications, which is suboptimal for chromatic confocal imaging. In the demonstration, only blue pixels were utilized, severely restricting the measurable depth range. To further enhance the depth range, a hyperchromatic confocal objective lens is required, which is covered in Chapter 4. The third limitation pertains to the brightness of individual microLED pixels, which may hinder a wide range of applications involving objects with low reflectivity. The fourth, but not the final, limitation is the relatively low frame rate, rendering the system unsuitable for high-speed imaging applications.

For a practical chromatic confocal imaging system, a custom microLED panel should be developed with the following properties: (1) the pitch should be smaller than 3 µm to achieve 0.5 µm lateral resolution with a 0.5 NA objective; (2) the spectrum should be larger than 150 nm to increase the measurable depth range; (3) the brightness should be higher for applications with low reflectivity (for example, skin tissue) than for display; and (4) the frame rate should be higher than 240 Hz so that the entire imaging process can be finished

within 1 s. With the above optimal properties, we believe that the proposed microLED-based chromatic confocal imaging system will have a wide range of applications, from industry to clinical care.

Chapter 4

Design of the Hyperchromatic Confocal Objectives

4.1 Overview

In the Chapter2 and Chapter 3, two distinct types of digital scanning chromatic confocal systems were introduced. However, these systems share two common limitations: the relatively short measurable depth range and the small NA of the objective lens, which results in inadequate resolution. Meanwhile, in the microLED-based chromatic confocal system [91], an aspheric singlet lens was employed to generate a substantial amount of longitudinal chromatic aberration over a bandwidth of approximately 50nm. While this approach introduced a significant amount of longitudinal chromatic aberration, it also led to the introduction of substantial off-axis aberrations, thereby limiting the FOV of the system.

To address these limitations, there is a strong motivation to develop a specially designed objective lens tailored to our biomedical applications. Such an objective lens should possess the following key characteristics:

1. Large longitudinal chromatic aberration: The objective lens should exhibit a substantial amount of longitudinal chromatic aberration, enabling the encoding of depth information over a broad spectral range. This feature is crucial for achieving an extended measurable depth range, which is desirable for various biomedical imaging applications.

2. Well-corrected monochromatic aberrations over a broad spectral bandwidth: While longitudinal chromatic aberration is desired, the objective lens should be well-corrected for other monochromatic aberrations for each wavelength, such as spherical aberration, coma, astigmatism, and field curvature. This ensures that the system can maintain diffraction-limited performance at each individual wavelength within the operational bandwidth.

3. Adequate NA and FOV: The designed objective lens should offer a larger NA, enabling higher resolution and improved light collection efficiency. Additionally, it should provide an appropriate FOV, minimizing off-axis aberrations and enabling the imaging of larger sample areas without compromising image quality or resolution.

Consequently, we are eager to develop a specially designed objective lens that meets the specific requirements of our biomedical applications. This objective lens should possess a large longitudinal chromatic aberration to facilitate extended depth range measurements, while simultaneously being well-corrected for other monochromatic aberrations. In this Chapter, we will present three hyperchromatic objective lenses for different application scenarios.

4.2 Design Strategies and Consideration

Based on equation 1.18, low abbe number materials are preferred for designing the hyperchromatic objective lens. However, in some of our applications, such as the MicroLED-based chromatic confocal microscope discussed in Chapter 3, the dispersion provided by material refraction alone may not be sufficient to generate the desired large chromatic shift.

Our design also utilizes diffractive surfaces to enhance chromatic shift. Meanwhile, image quality at each wavelength is well optimized by multiconfiguration in OpticsStudio (Zemax).

The main design criteria for the chromatic confocal objective include:

1. Working bandwidth
2. Chromatic shift
3. Working distance
4. NA of the objective lens
5. Material and fabrication availability

The chromatic shift is influenced by the bandwidth of the light source, the optical layout, and the dispersion characteristics of the optical components. It is defined as the difference between the working distances for the minimum wavelength λ_{min} and the maximum wavelength λ_{max} of the source spectrum. Combining equation 1.16 and 1.18, the longitudinal chromatic shift $Deltas'_n$ can be approximated as:

$$\Delta s'_n = -\frac{4F_{\#}^2}{n'} \sum_{i=1}^{n} \frac{\Phi_i y_i^2}{V_i}. \tag{4.1}$$

The dispersive behavior of the refractive and diffractive and optical elements is defined by the Abbe number V_i:

For a refractive lens, the focal power ϕ is given by equation 1.14. $n(\lambda)$ is the refractive index of the lens, usually dependent on the Abbe number of the material. To enhance chromatic aberrations, preferential use of low Abbe number glasses with significant refractive

index differences across various wavelengths is recommended. The Abbe number ν_{ref} for the refractive lenses is determined by the refractive index of the lens material at selected wavelengths as [92]:

$$V_i = \begin{cases} \frac{n(\lambda_d)-1}{n(\lambda_F)-n(\lambda_C)} & \text{for refractive elements,} \\ \\ \frac{\lambda_d}{\lambda_F-\lambda_C} & \text{for diffractive elements.} \end{cases} \tag{4.2}$$

For example, the Abbe numbers of Schott preferred glasses range approximately from 21 to 85 [93]. By contrast, diffractive elements always have an Abbe number of -3.45 for these wavelengths. Thus, they are very well suited for the realization of an increased chromatic shift of the chromatic confocal system within a short bandwidth.

In Zemax, diffractive surfaces bend rays according to the grating equation. The Binary 2 surface allows the grating period to vary as a rotationally symmetric polynomial. It uses the phase advance or delay to change the direction of the propagation of the ray. The binary 2 surface adds phase to the ray according to the following equation no matter what the wavelength is:

$$\phi(\rho) = m \sum_{i=1}^{n} A_i \rho^{2i} \tag{4.3}$$

Where $\phi(\rho)$ is the phase in periods at radius ρ, n is the number of the polynomial coefficients in the series, A_i is the coefficient on the 2^{ith} power of ρ, which is the normalized radial coordinate, m is the diffraction order. The coefficient A1 of equation 4.3 is the determinant of the diffractive surface optical power when m= 1, which is equal to $1/f = \lambda A_1$. It means that different wavelengths will give different optical powers.

It is worth noting that the chromatic shift is also proportional to the $F_{\#}$ based on equation 4.1. This implies that achieving significant hyperchromatization becomes increasingly challenging for fast optical systems with high numerical apertures (low F/#). Consequently, for such high-performance, high-NA applications, a more complex hybrid diffractive-refractive optical design is often required. The synergistic combination of diffractive and refractive components in a hybrid optical design allows for greater flexibility in manipulating the chromatic behavior and aberration control of the system, enabling the simultaneous achievement of high numerical apertures and significant chromatic shifts. By well optimizing the focal power distribution between the diffractive and refractive elements, the lens shape, and the diffractive surface, a high-performance hyperchromatic objective lens could be achieved.

The hyperchromatic objective lenses are designed and optimized in Zemax using multiconfiguration. Related merit functions are established to control longitudinal chromatic aberration and image quality between wavelengths. Meanwhile, the NA, focal length of the lens and other intrinsic restrictions are locked to reach the specification. In the optimization, the terms of diffractive surface are well controlled to make the diffractive zones not too dense to fabricate by a diamond turning machine.

4.3 Hyperchromatic Objective Lens for MicroLED

The first design is to develop a hyperchromatic objective lens for a MicroLED-based chromatic confocal system. The target MicroLED is from Jade Bird Display (JBD), which is shown in Figure 4.1(a). The main specification of the MicroLED is shown in table 4.1. It can be seen that the working bandwidth is from 500 nm to 550 nm, only 50 nm.

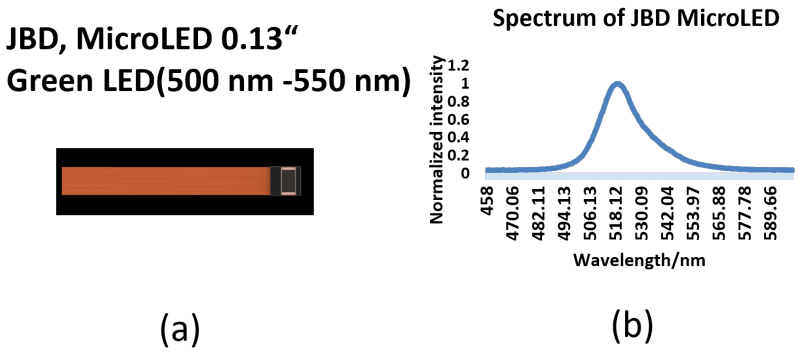

Figure 4.1: (a)JBD MicroLED and (b)Corresponding spectrum

.

Table 4.1: Main specification of target MicroLED

Resolution	640 × 480
Pixel pitch	4 µm
Dimension of the active area	0.13″
Wavelength	525±25 nm
Fresh rate	100Hz

To achieve subcellular resolution, confocal microscopes typically use large NA (> 0.5) objective lenses. The final specification of the designed objective lens is listed in Table 4.2. The designed chromatic shift is around 300 µm over only 50 nm bandwidth. When considering the materials available for diamond turning manufacturing, we have PMMA (glass code: 491579) and OKP4HT (glass code: 632233). While OKP4HT has an Abbe number of 23, indicating relatively strong dispersion, it is challenging to generate a large chromatic shift solely through refraction dispersion. Additionally, another factor to consider is that the transmission performance of OKP4HT is not as good as PMMA, limiting the number of elements that can be fabricated using OKP4HT. So we decided to use a combination of

diffractive and refractive components as discussed in section 4.2. Figure 4.2 shows the layout of the designed objective lens. The 1^{st} and 2^{nd} are diffractive elements made by PMMA. The 3^{rd} and 4^{th} elements are even aspherical lenses made by OKP4HT and PMMA, respectively. The last one is a commercial optical window made by SAPPHIRE. The air gap between 3^{rd} element and 4^{th} element is designed to make the system work for both front view and side view by adding a folding mirror.

Table 4.2: Main specification of designed objective

NA (in water)	0.5
Effective focal length	10.6 mm
FOV	±0.4 mm
Wavelength	500 nm∼550 nm
Chromatic shift	∼ 300 µm
Working distance	64 µm∼364 µm
Material	PMMA and OKP4HT
OD	25.4 mm

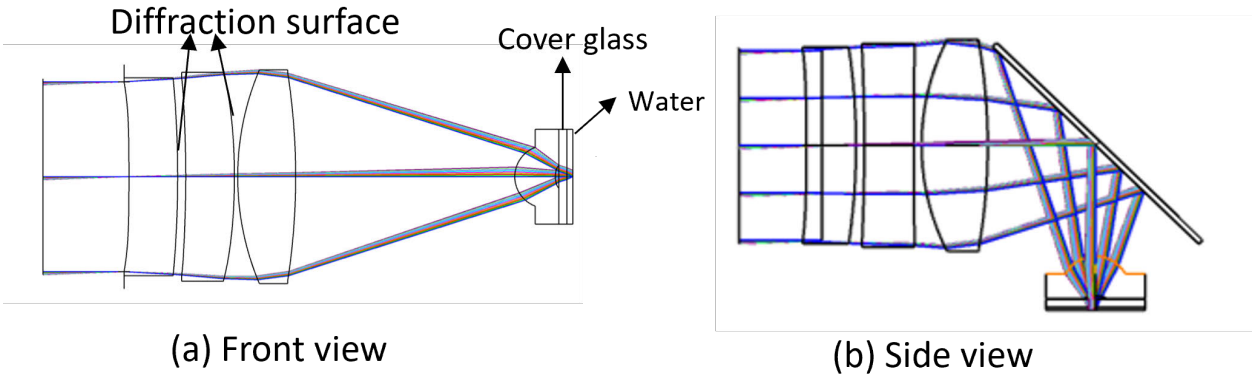

Figure 4.2: Layout of the hyperchromatic objective lens. (a) Front view configuration and (b)Side view configuration

.

By controlling the spot size on the image plane, the final optical performance simulation results at 525 nm of the objective are shown in Figure 4.3. The RMS wavefront error over the entire FOV is less than 0.07 waves. Based on Figure 4.3 (a0,(b), and (C), the system has a diffraction-limited performance. Meanwhile, the first-order chromatic shift is around 300 µm, which meets the spec.

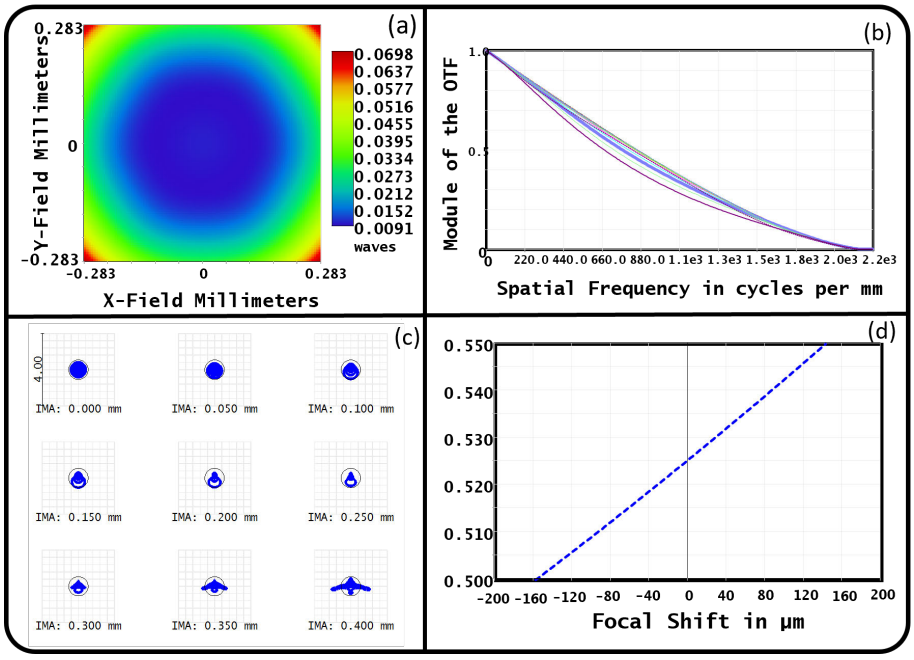

Figure 4.3: Performance of the hyperchromatic objective lens. (a) RMS wavefront error, (b)MTF, (c) Spot size, and (d) Chromatic shift

.

After optimization, the diffraction element exhibits a minimum local period of 14 µm at the outer rims of the elements. The diffraction surface has a sag of 1.05 µm. The manufacturing of the objective lens was carried out by our lab mate, Dr. Wenjun Kang. He employed a snap-on mounting strategy for the assembly of the lens components. The final fabricated objective lens is depicted in Figure 4.4. Another lab mate Shuyuan Guan helped us test the performance of the objective lens by measuring multilayer films, the result is shown in Figure

4.5. While the experiments showed promise in initial tests, biomedical tissue imaging revealed several challenges. Firstly, the signal strength from the MicroLED was insufficient for efficient tissue penetration. Although the chromatic shift of approximately 300 µm seemed favorable, the absorption and scattering properties of tissue at the 525 nm wavelength limited the achievable imaging depth. Furthermore, the scattering of light within the tissue significantly reduced image contrast, compromising the overall image quality. These factors have highlighted the need for further improvements in the source intensity, and wavelength selection to mitigate the effects of penetration and scattering.

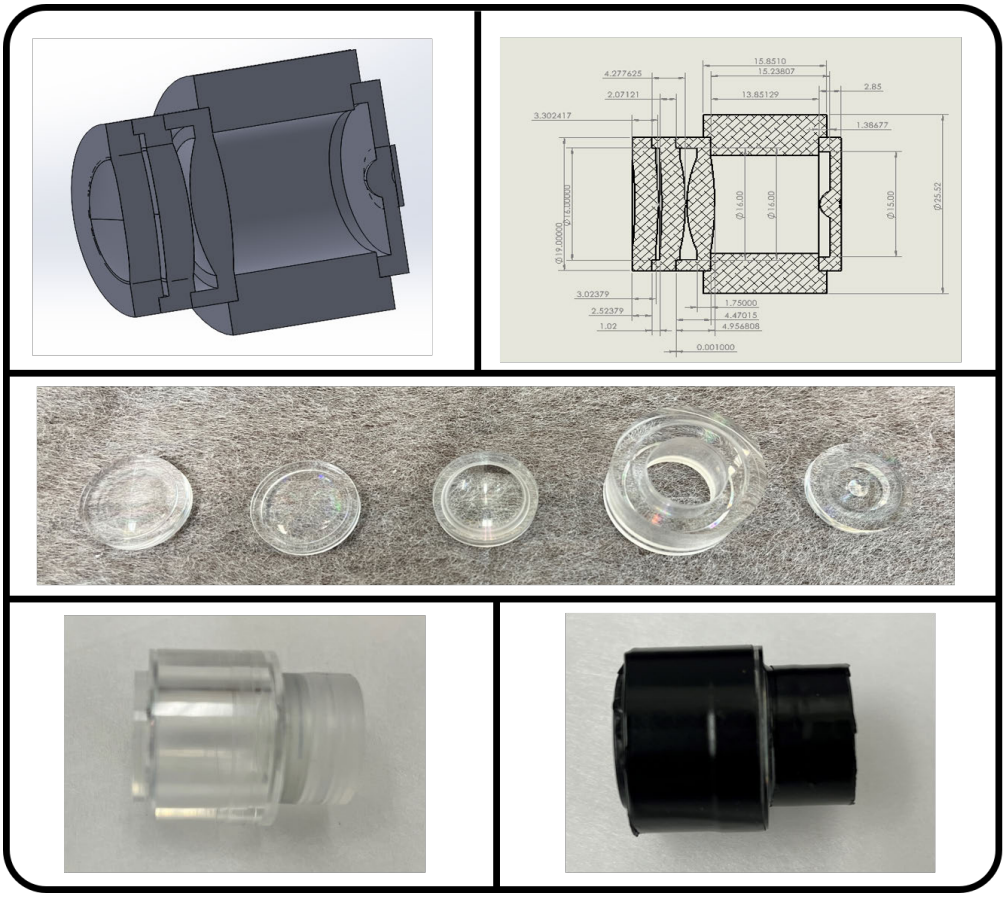

Figure 4.4: Fabricated objective lens

.

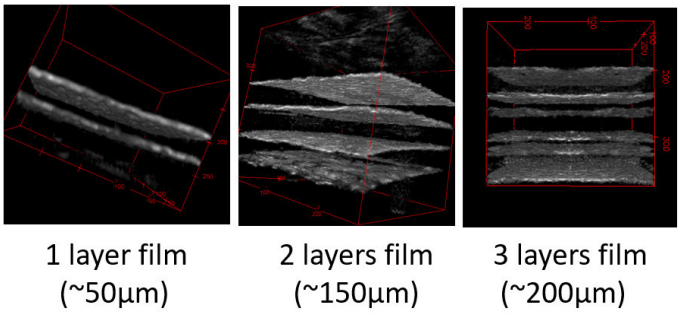

Figure 4.5: 3D imaging of multilayer films by our objective lens

.

4.4 Hyperchromatic Objective Lens for Laser Scanning

To address the issue mentioned in the previous section, we considered designing another hyperchromatic objective lens that works in the Near Infrared (NIR) range. The major specification is listed in Table 4.3. The bandwidth of the source is selected from 600 nm to 810 nm to reduce speckle noise from the tissue. The corresponding chromatic shift is∼750 µm. The designed hyperchromatic objective has NA of 0.7 in water across ±0.4 mm lateral field. It offers 40x magnification through a tube lens with a 200 mm focal length.

Table 4.3: Main specification of designed objective

NA (in water)	0.7
Effective focal length	5 mm
FOV	±0.4 mm
Wavelength	600 nm∼810 nm
Chromatic shift	∼ 750 µm
Working distance	50 µm∼800 µm
Material	PMMA

To reduce the number of elements to be manufactured, we decided to combine off-the-shelf lenses and two pieces of diamond-turned lenses to realize the final design. Figure 4.6 shows the layout of the hyperchromatic objective lens. The objective lens has a total length of 160 mm and an outer diameter of 60 mm. It was composed of 5 off the shelf lenses (L1, L2, L3, L5, L6) and two diamond-tuned PMMA lenses(L4, L7) as shown in Figure 4.6A. L4 is the system stop. It employs front-surface even aspheric terms and a rear diffractive surface to correct spherical aberrations and enhance chromatic shift. L7 is also an aspheric lens which is used to correct off-axis aberrations. By controlling the spot size on the image plane, the final optical performance simulation results of the objective lens at 700nm are shown in Figure 4.7. Figure 4.7A, Figure 4.7C, and Figure 4.7D show the MTF, RMS wavefront, and spot diagram errors across the FOV, indicating that the lens has a diffraction-limited performance.

We have fabricated the objective lens as well by Dr.Kang and tested the preliminary performance. The diffractive lens L4 and aspheric lens L7 are made of PMMA by diamond tuning as shown in Figure 4.8A. Custom holders were designed for the objective lens assembly as shown in Figure 4.8B. The lens housing is divided into two parts at the air gap between L3 and L4. The reason is that this air gap is the least sensitive thickness after sensitive analysis. The axial distance between these two parts can be adjusted to actively align the objective lens, which is also considered a focus compensator.

We built a laser scanning chromatic confocal system to evaluate the objective performance [94]. Figure 4.9A shows the 2D image of the USAF resolution target. The line patterns in group 9, element 3 were well distinguished. Figure 4.9B shows the volume image

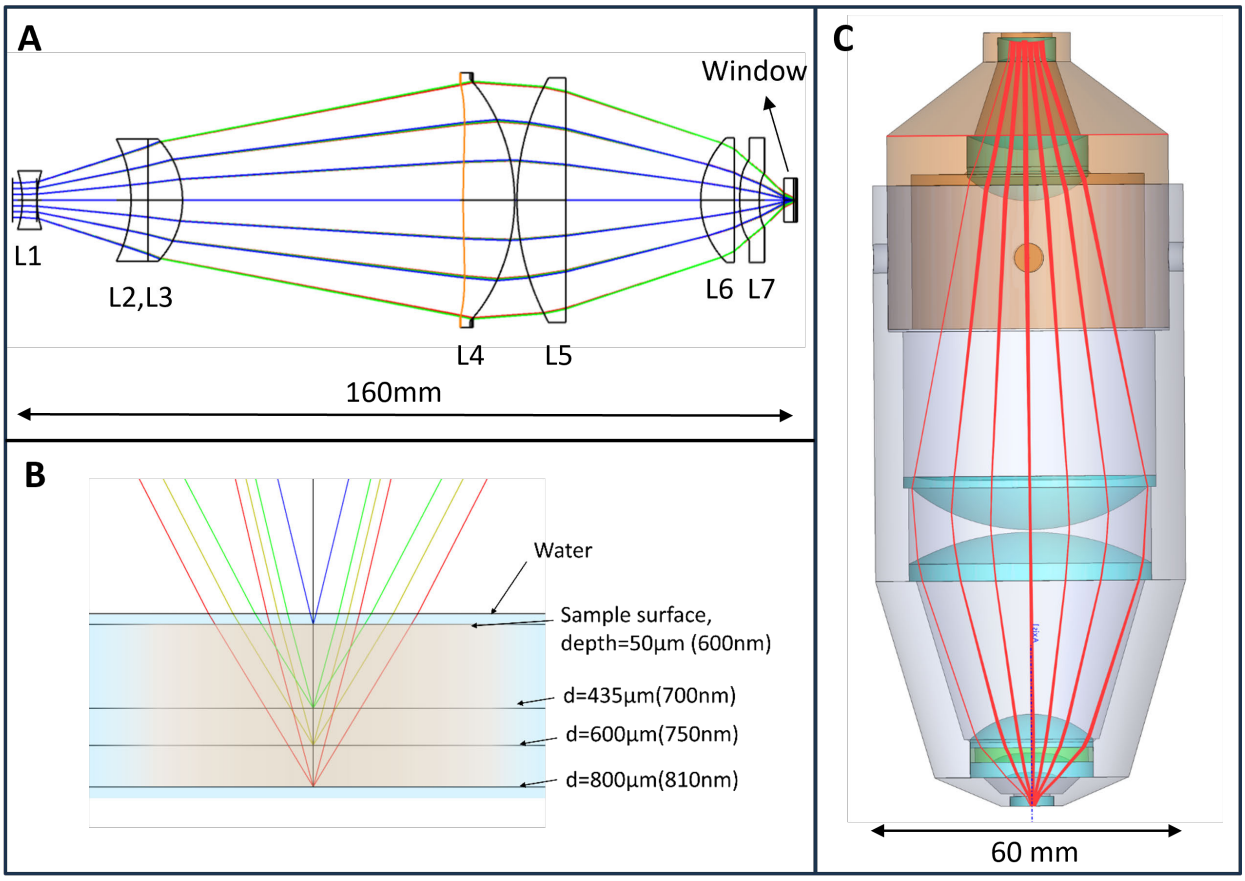

Figure 4.6: Layout of the hyperchromatic objective lens. A-Schematic; B-Magnified view showing chromatic shift along the tissue depth; C-Final objective lens with mechanical housing.

.

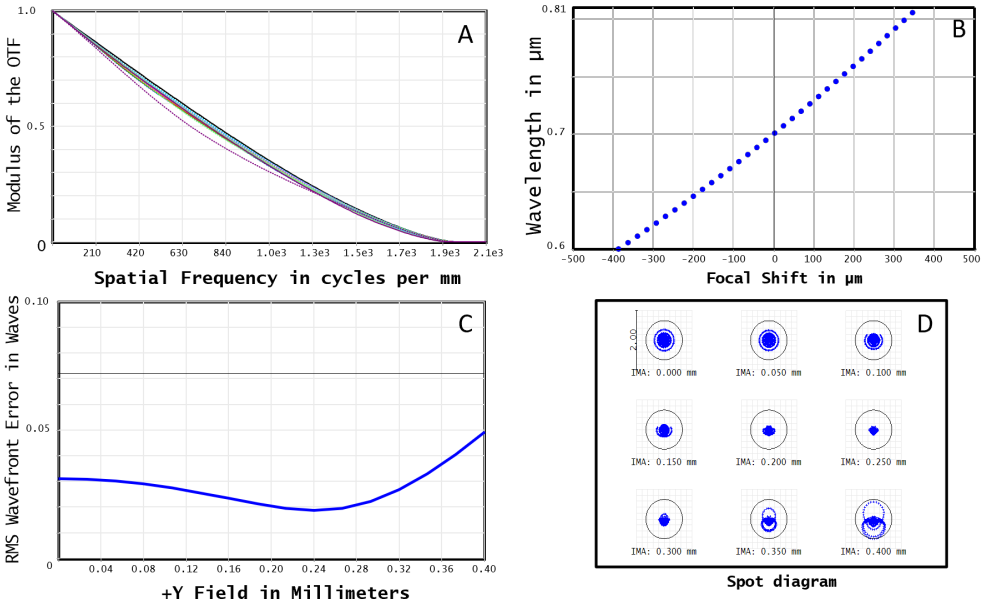

Figure 4.7: Performance of the designed objective lens at 700 nm. A-MTF; B-Chromatic shift; C-RMS wavefront error; D-Spot diagram.

.

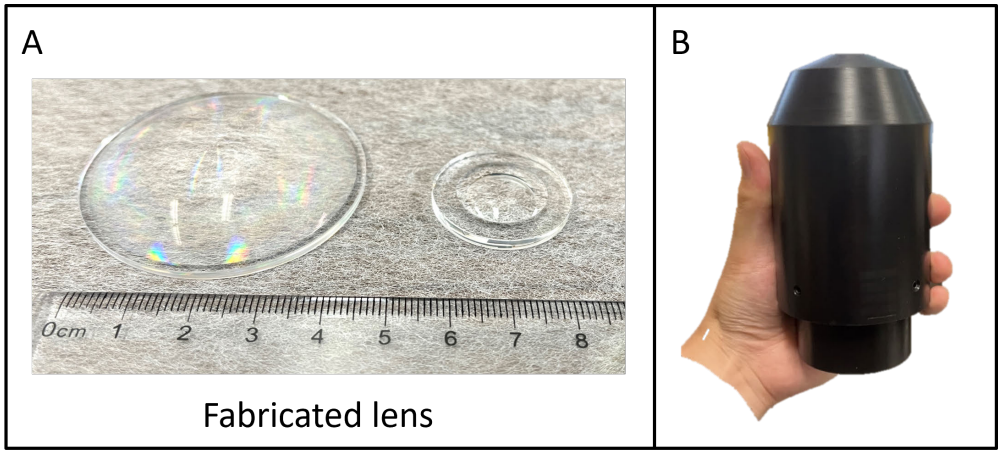

Figure 4.8: Fabricated objective lens. A-Diamond tuned diffractive lens and aspheric lens; B-Custom holders for objective lens assembly.

.

of the lens tissue captured by our objective lens, demonstrating the 3D imaging capabilities. We also test some tissue samples as shown in Figure 4.10.

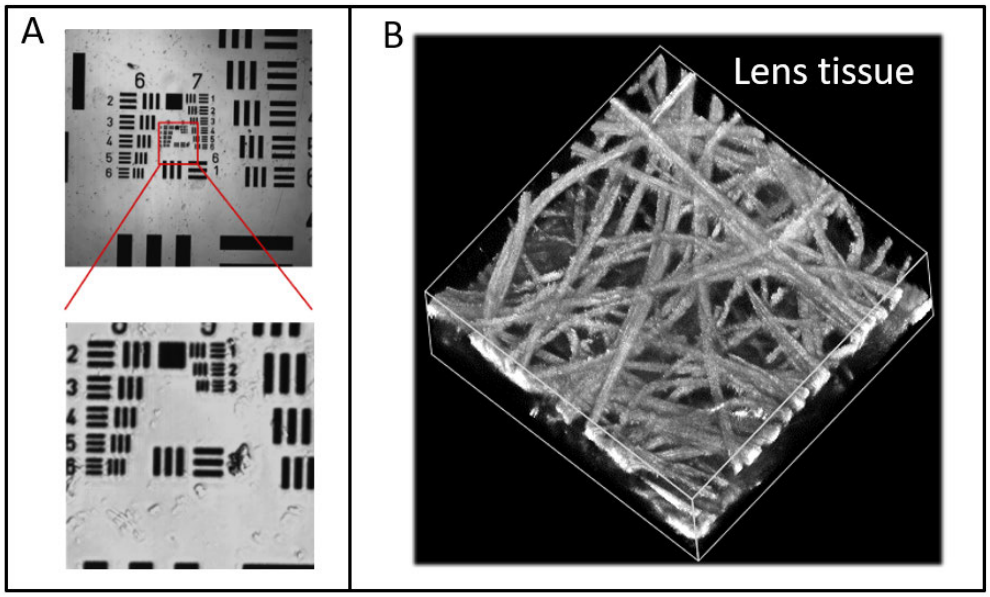

Figure 4.9: Image of the USAF resolution target (A) and 3D volume image of lens tissue (B).

.

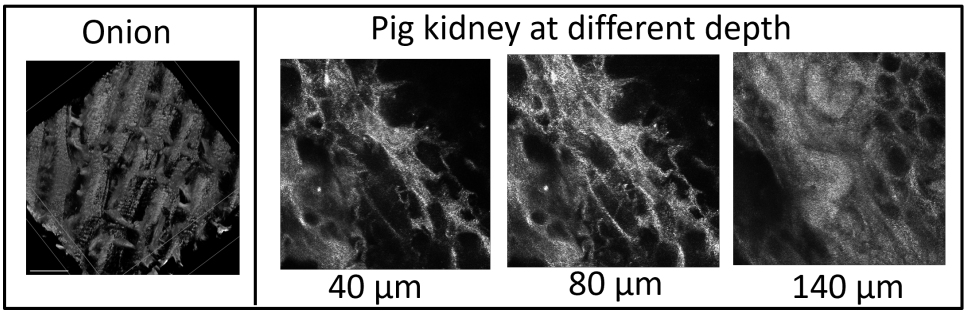

Figure 4.10: 3D Image of the onion, and pig kidney tissue at different depths.

.

However, there are still some downsides to this objective lens.

1. The fabricated lens housing fails to provide a sufficiently precise air gap control, compromising the desired accuracy. Concurrently, the peripheral surface profiles of the

commercially available off-the-shelf lenses are inadequate for high NA imaging applications. The measured NA is around 0.5 which is lower than the design target 0.7.

2. We increased the marginal ray height to introduce large longitudinal chromatic aberration, which sacrifices the overall form factor. The resulting 750 µm chromatic shift exceeds the requirements for biomedical applications but holds potential advantages in metrology applications, where such significant chromatic variation could prove beneficial.

3. The microscope design features a high magnification of 40x, which poses a challenge in initially locating the region of interest or identifying the imaging target within the relatively confined FOV. The narrow FOV resulting from the substantial magnification can hinder the initial search and acquisition of the desired sample area or object.

4.5 Dual View Chromatic Confocal Microscope Objective

To address the limitations of the current objectives, we propose a new type of microscope objective that has integrated wide-FOV imaging.

Waveguide plates have been developed to combine the see-through mode and virtual display mode in augmented reality (AR) applications [95, 96]. Waveguide is an optical combiner, made of a thin piece of clear glass or plastic with specific structures or surface features, which helps guide electromagnetic waves in particular directions, shapes, or patterns [97]. The waveguide core comprises three distinct parts: the input coupler, the propagating section, and the output coupler. The input coupler facilitates the transfer of light from the micro-display into the waveguide. Subsequently, the light propagates through the waveg-

uide's propagating section via total internal reflection (TIR). After the light reach the output coupler, it couples the light out of the waveguide, directing it towards the eye pupil [98].

By integrating the waveguide into the microscope, we can design a dual-view microscope objective lens with a small form factor. It will combine high-resolution microscope imaging mode and wide-FOV imaging mode. The basic idea is shown in Figure 4.11. In microscope imaging mode(blue light in Figure 4.11), the high NA light will go through all the elements in the objective. In this case, the waveguide itself will be treated as a parallel plate. In wide-FOV imaging mode(red light in Figure 4.11), the front group collimates the light from large FOV and then couples the light into the waveguide. The light then propagates inside the waveguide and exits the waveguide on the output surface. An imaging system will then focus the light onto a digital sensor.

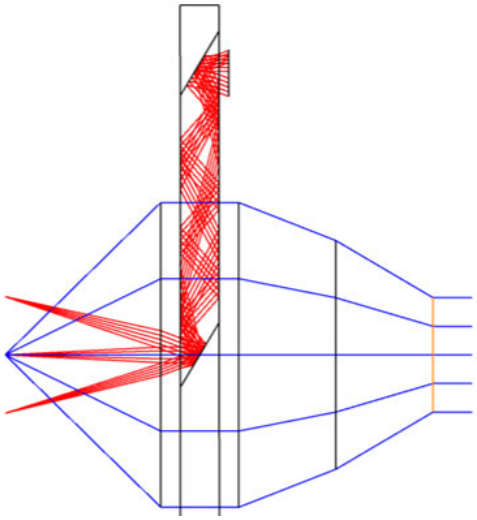

Figure 4.11: Schematic diagram of the proposed dual view objective .

.

Based on that, we designed a dual view chromatic confocal microscope objective. Table 4.5 lists the main specs of the objective. It is also a water-immersed objective that has NA of 0.75 and works at NIR range.

Table 4.4: Specification for High NA path of designed dual view objective

NA (in water)	0.75
Effective focal length	5.3 mm
FOV	±0.5 mm
Wavelength	650 nm∼950 nm
Chromatic shift	∼ 415 µm
Working distance	5 µm∼420 µm
Material	PMMA and OKP4HT
OD	30 mm

Table 4.5: Specification for Wide-FOV path of designed dual view objective

Working F/#	3
FOV	±5 mm
Wavelength	650 nm
Working distance	5 µm
Waveguide Material	N-BK7

Figure 4.12 shows the layout of the designed objective. The top and bottom of the figure show the basic ray path for the high NA mode and wide-FOV mode, respectively. In this design, we only use refractive elements due to the relatively large bandwidth 300 nm. The objective includes 4 aspheric lenses, 1 off-the-shelf lens(the negative lens), and one glass geometrical waveguide [99].

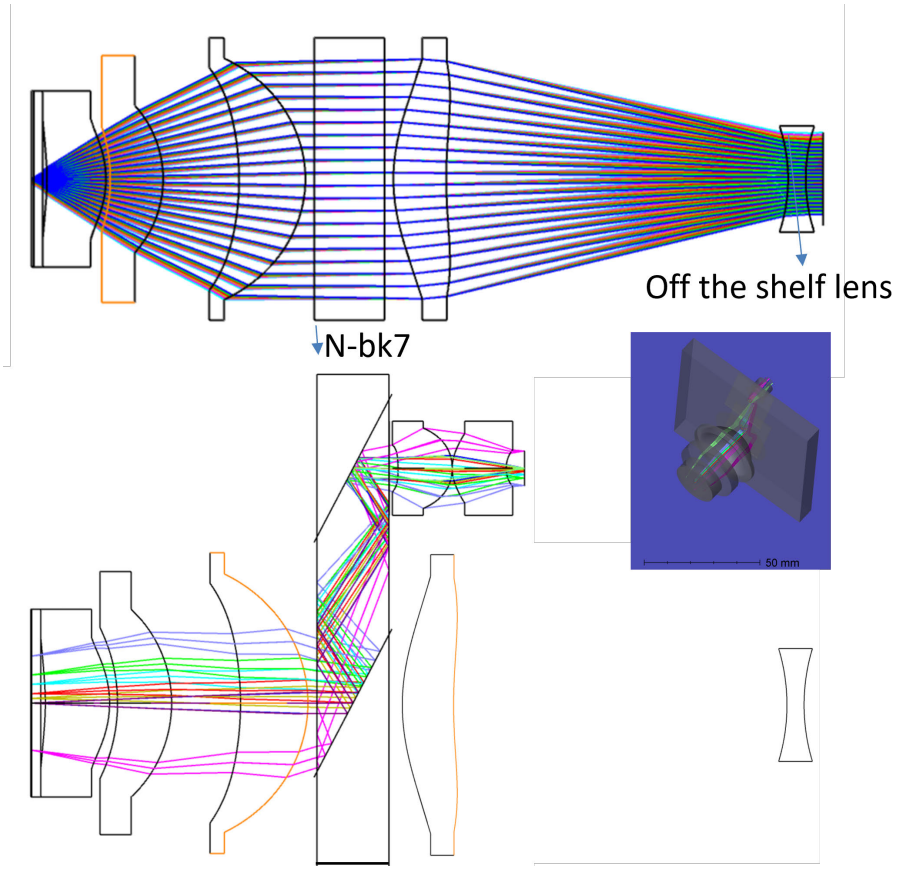

Figure 4.12: Layout of the dual view objective.

.

The designed performance of the objective is shown in Figure 4.13. According to Figure 4.13(a), (b), and (d), the high NA optical path demonstrates diffraction-limited performance across the designed FOV. The chromatic shift observed in this path is approximately 415 µm. Regarding the wide-FOV path, the imaging performance requirements are less stringent

compared to the high NA path, as its primary function is to provide a low NA viewfinder. The MTF for this path is deemed acceptable, and the pincushion distortion can be corrected through digital calibration techniques [100].

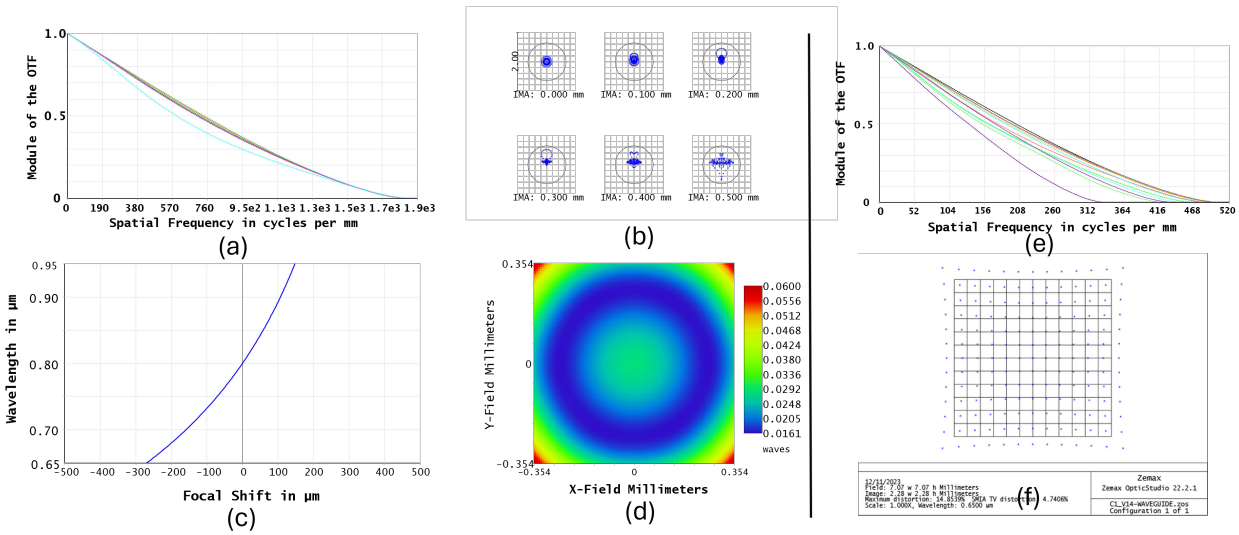

Figure 4.13: Performance of the designed objective lens in high NA mode:(a)-MTF; (b)-Spot size; (c)-Chromatic shift; (d)-RMS wavefront error. Performance of the designed objective lens in wide-FOV mode:(e)-MTF and (f)-Distortion

.

To analyze the potential stray light introduced by the waveguide, we performed non-sequential ray tracing simulations using LightTools software. Figure 4.14 illustrates the signal ray path and the strongest ghost ray path identified in the analysis. The most prominent ghost is caused by unwanted reflections from the in-coupler mirror. The signal-to-noise ratio (SNR), calculated as I_{signal}/I_{ghost}, is approximately 20, indicating that the noise contribution is relatively weak compared to the signal. Figure 4.15 demonstrates the image simulation of the final wide-FOV mode, where (a) displays the image in a linear scale, revealing pincushion distortion. The ghost image, however, is only visible in the logarithmic scale representation shown in Figure 4.15(b), where it appears to be negligible in magnitude.

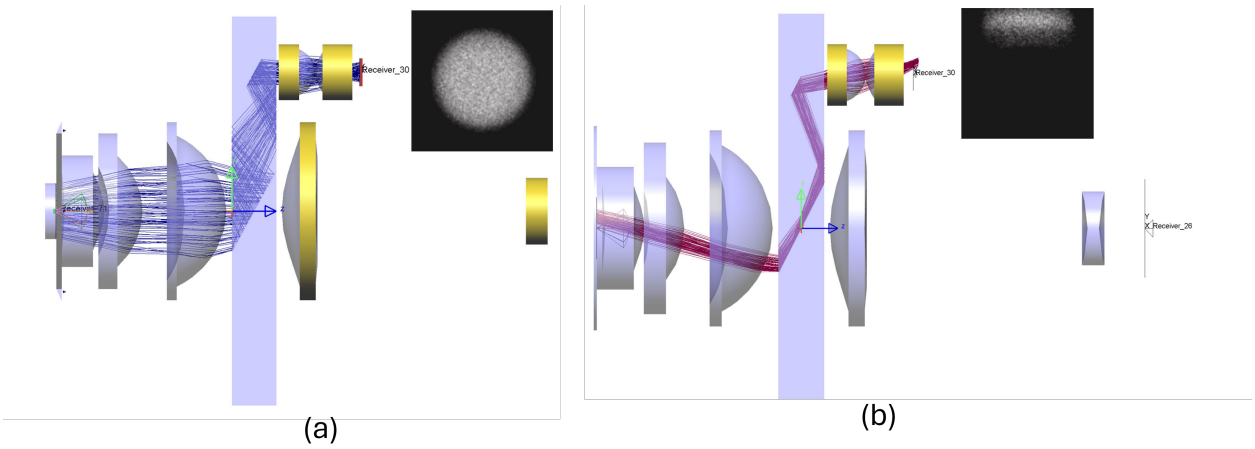

Figure 4.14: Ray path of (a) Signal path and (b) ghost path

.

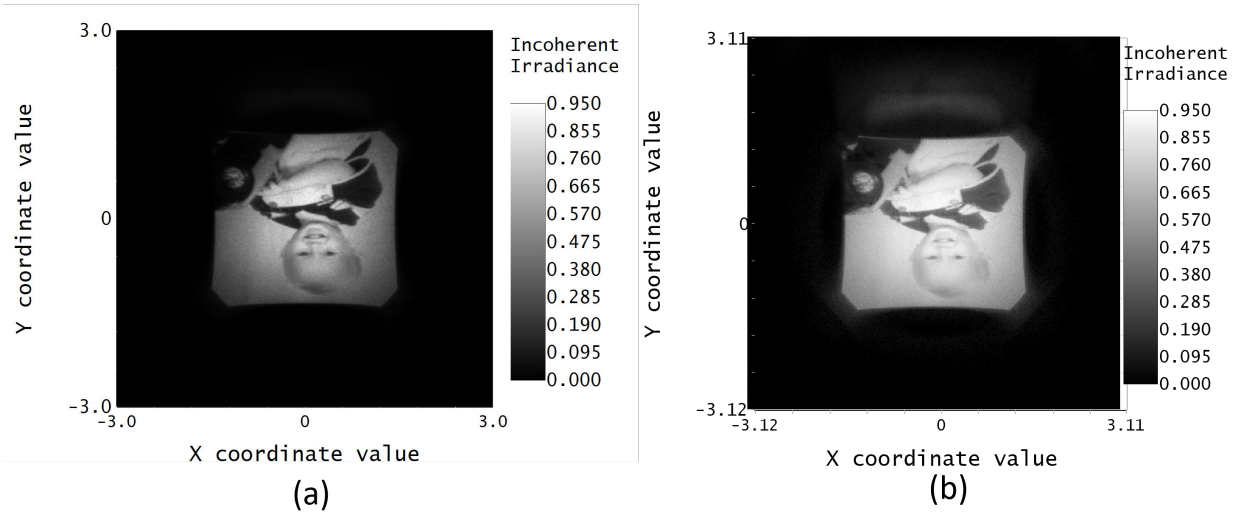

Figure 4.15: Simulation result of the wide-FOV mode. (a) Linear scale, (b) logarithmic scale

.

Chapter 5

Development of a Multimodal Intraoral Screening System for Oral Cancer

5.1 Motivation

Oral cancer occurs in the mouth or throat, causing considerable pain for the patient as shown in Figure [101]. Oral cancer poses a significant public health challenge globally, and its impact is particularly pronounced in LMICs due to limited healthcare resources and awareness [102]. In South and Southeast Asia countries, oral cancer is the most prevalent form of cancer [103]. The high mortality rates associated with oral cancer can be attributed to various factors, including lifestyle choices and geographic disparities. One particularly harmful practice prevalent in these regions is the consumption of betel quid, a combination of areca nut, betel leaf, and often tobacco, along with additional flavorings [104]. Early detection through screening programs holds the key to reducing the burden of this disease in these high-risk regions [105]. Currently, clinically viable in vivo detection methods such as conventional oral examination (COE) and Autofluorescence visualization (AFV) are widely used in oral cancer early detection [106]. Both of the methods mostly focus on the detection of lesions' surfaces with limited resolution. OCT (Optical Coherence Tomography) stands as a firmly established technique for depth-resolved imaging [11]. By taking advantage of the short coherence length of a broadband light source, OCT performs high-resolution,

cross-sectional, and three-dimensional volumetric imaging of the internal microstructure in biological tissues by measuring echoes of backscattered light [107].

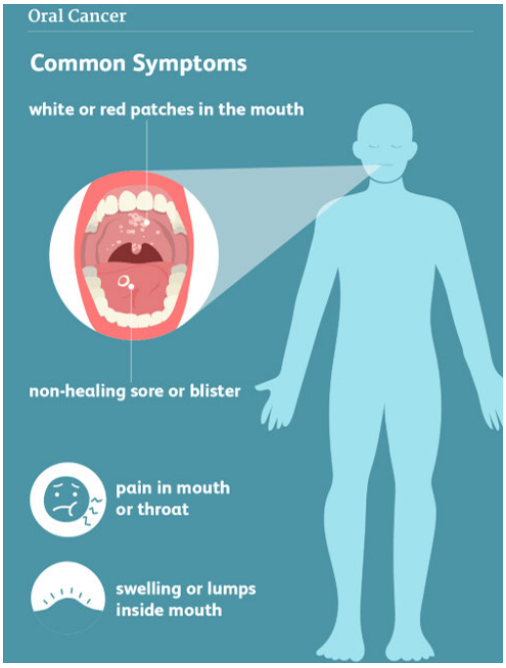

Figure 5.1: Illustration of Oral cancer[101]

.

We have already built a smartphone-based, dual-modal(COE and AFV) oral cancer screening platform [108]. The platform consists of a commercial Moto G5 Android smartphone, an intraoral imaging probe, a light-emitting diode (LED) driver, a rechargeable lithium battery, and a mobile application. The system utilizes four 405-nm Luxeon UV U1 LEDs (Lumileds, Amsterdam, Netherlands) to enable intraoral autofluorescence imaging and four 4000-K Luxeon Z ES LEDs for intraoral white-light imaging. The custom Android application provides the user interface, controls the phone and probe, and captures dual-modal intraoral images.

In this Chapter, we will demonstrate the development of a multimodal(COE, AFV, and OCT) intraoral screening system for oral cancer. The system includes:

1. Handhold multimodal intraoral probe;
2. Commercial laptop;
3. Swept source OCT system;
4. Portable carry-on case that carries the entire OCT system, and the illumination control module for autofluorescence imaging and white-light imaging;
5. The custom desktop software provides a user interface and controls the whole system.

5.2 Method

5.2.1 Optical Design of the Handheld Intraoral Probe

In this section, we discuss the optical design and mechanical design of the intraoral probe. To accommodate the intended application of intraoral imaging, the probe design is optimized for a long, slender form factor with a small outer diameter. This configuration enables easy insertion and maneuverability within the confined spaces of the oral cavity while minimizing patient discomfort. To reduce the form factor, we utilize a two-axis MEMS scanner mirror(A5L3.2, 3.6 mm integrated mirror, Mirroracle Technologies, USA) to perform the lateral scan. Compared with XY galvanometric mirror pair, this MEMS-based scanner is more compact and lower cost. The optical system was designed using OpticsStudio (Zemax). Figure 5.2 shows the layout of the designed lens system for OCT imaging and Table 5.1 lists the detailed specifications.

The total length of approximately 145 mm and the maximum diameter of 11 mm are configured to ensure the probe's sufficient extension for oral cavity insertion. Light from

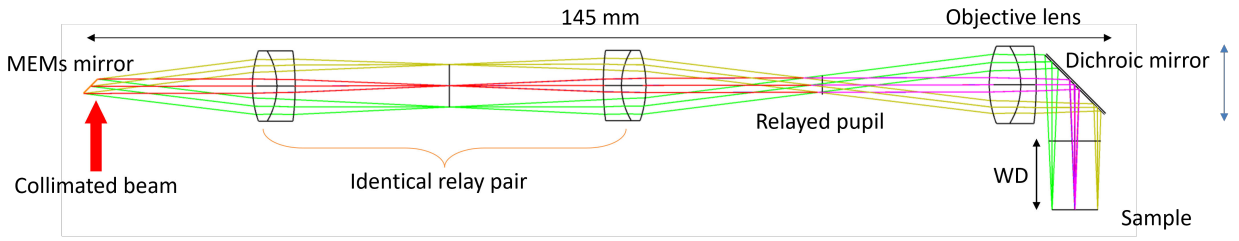

Figure 5.2: Layout of the probe lens system for the OCT imaging.

.

Table 5.1: Specification of the designed lens system.

NA	0.037
FOV	±8 degree
Bandwidth	1260 nm -1360 nm
EP	2 mm
WD	10 mm
Material	H-ZPK5, H-ZF13

a single-mode fiber is collimated and reflected by the MEMS mirror into a 4f relay pair composed of two identical achromats. The relay pair has a unit magnification and the relayed pupil is located at the front focal plane of the last achromatic doublet to achieve telecentric illumination with NA of 0.037. A telecentric optical system possesses the benefits of having a flat image plane, a constant magnification, and a constant spot size even off-axis [109]. Based on equation 1.24, the theoretical lateral resolution for our probe is ∼13.1 µm. Another consideration of NA is the depth of focus(DOF), which is given by equation 1.25. It shows the theoretical axial range is 1.2 mm when the refractive index is 1.3. Since both DOF and lateral resolution are related to the central wavelength and NA, there is a trade-off between the choices of higher lateral resolution and higher DOF. On the other hand, the MEMS mirror, with a rotational capacity within the range of ±4°, governs the system's Field

of View (FOV) at ±8°. The working bandwidth is aligned with the swept source laser output (1260nm to 1360nm). The entrance pupil diameter is 2mm, which is determined by the fiber collimator (F220APC-1310, Thorlabs, f=11.26 mm). The final layout system offers 10 mm working distance after folding by a dichroic mirror. The dichroic mirror selectively reflects near-infrared (NIR) light while transmitting visible light. By incorporating a dichroic mirror into the optical path, we can place an additional camera above the dichroic mirror to capture autofluorescence imaging and white light imaging, effectively combining OCT and these two imaging modalities into a single probe.

After optimization, the system performance is shown in Figure 4. The RMS wavefront error across the entire FOV remains below the diffraction limit, indicating excellent optical quality. Furthermore, chromatic aberration, a common issue with PSF degradation in OCT systems, has been effectively mitigated. The maximum distortion is less than 3%, which is highly favorable for raster scanning applications. Notably, the modulation transfer function (MTF) reaches the theoretical diffraction limit, signifying optimal image quality and resolution performance. The final designed achromatic doublets were fabricated by Shanghai Optics and coated with AR coating in the NIR range.

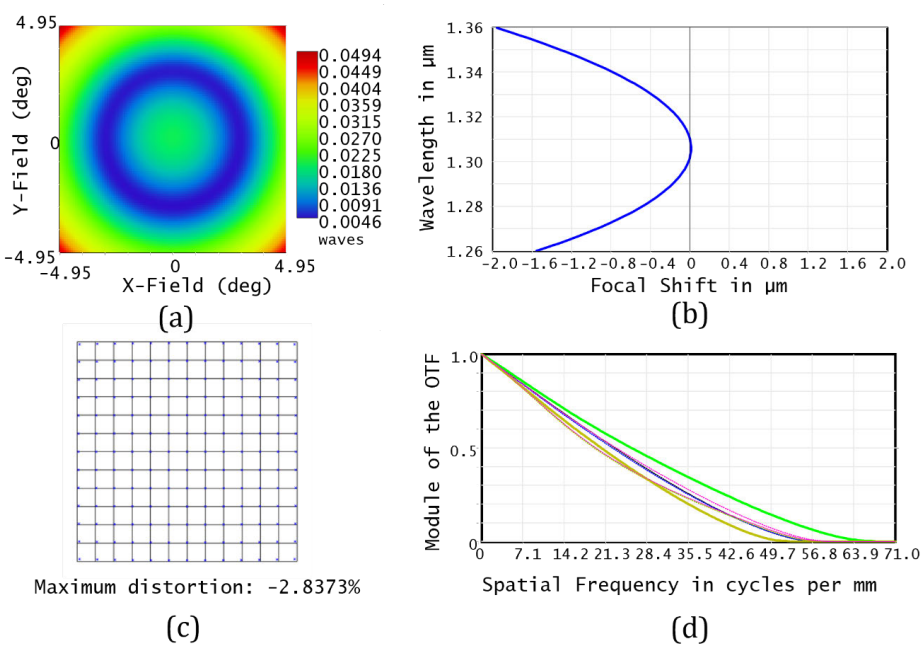

Figure 5.3: Optical performance of the designed lens system. (a) RMS wavefront over FOV, (b) Chromatic shift, (c) distortion over FOV, (d) MTF over FOV.

.

5.2.2 Swept-source OCT System Setup

SS-OCT module is truly the heart of the multimodal intraoral screening system. It provides the ability for the probe to penetrate the tissue and form volumetric imaging. As shown in Figure 5.4, the SS-OCT module employed a 1310 nm swept-source laser with a Michelson interferometer. The swept source 1310 nm laser was MEMS-VCSEL type (SL132121, Thorlabs Inc., NJ, USA), running at 200 kHz (line-scan rate), and 100 nm bandwidth. The bandwidth determines the axial resolution of our system as 7.5µm based on equation 1.20. The laser source also had an integrated A-trigger and K-clock that triggered the start of acquisition and the sampling interval for a linear k-sampling, respectively. The integrated K-clock was generated by a 32 mm Mach-Zehnder interferometer, giving a typical depth range of approximately 8 mm. This configuration serves to furnish a linear k-sampling clock

essential for data acquisition. As a consequence, the acquired signal manifests as an interferometric signal sampled in a linear wavenumber domain. The output laser from the swept

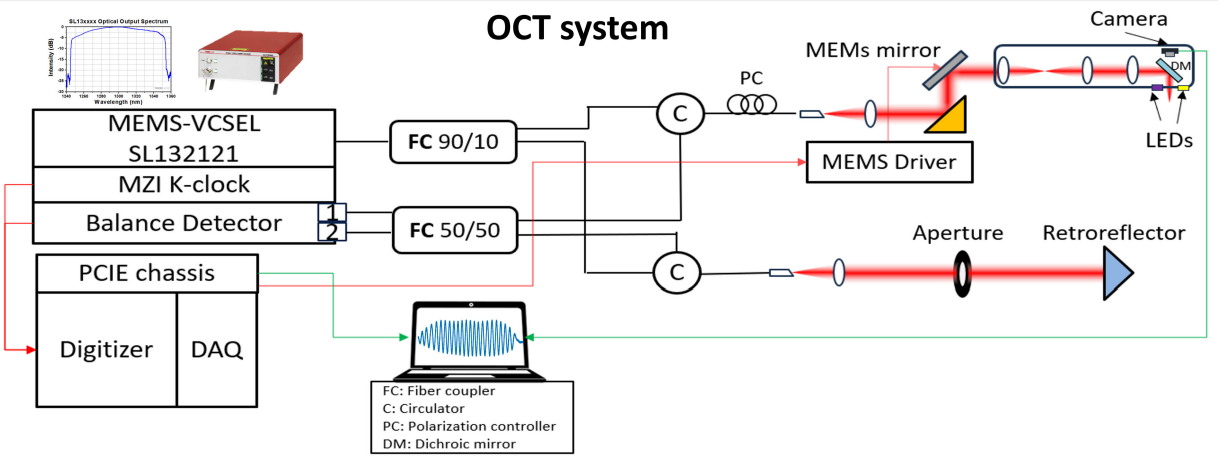

Figure 5.4: Schematics of the multimodal intraoral screening system.

.

source was divided into two optical paths by a 90:10 fiber coupler (TW1300R2A2, Thorlabs, NJ, USA): a sample arm carrying 90% of the optical power and a reference arm carrying the remaining 10%. In the sample arm, a dual-axis quasistatic MEMS mirror (A5L3.2, 3.6 mm integrated mirror, Mirroracle Technologies, USA) was paired with the custom probe to raster scan the laser beam over the sample. The MEMs rotation angle determines the actual FOV of the system, which corresponds to $\sim$ 7mm $\times$ 7mm on the sample plane. The power of the sample beam launched into in vivo tissues was $\sim$8 mW. In the reference arm, a reflective retroreflector was employed to redirect the optical beam back along its incident path, ensuring that the optical path length (OPL) in this arm precisely matched the OPL of the sample arm. The incorporation of a retroreflector in the reference arm enhances the portability and robustness of the OCT system, as it facilitates straightforward alignment procedures and ensures long-term stability as the entire system will go overseas. The backscattered light

from the sample arm and the reflected light from the reference arm were directed by two fiber optic circulators (CIR-1310-50-APC, Thorlabs, USA), and recombined in a fiber optic coupler (TW1300R5A2, Thorlabs, USA).The optically mixed outputs were detected by a high-speed balanced photodetector (PDB480C-AC, Thorlabs, USA).

The backscattered light for the sample arm and reflected light from the reference arm were directed by two fiber optic circulators (CIR-1310-50-APC, Thorlabs, USA), and recombined in a fiber optic coupler (TW1300R5A2, Thorlabs, USA). The optically mixed outputs were detected by a high-speed balanced photodetector (PDB480C-AC, Thorlabs, USA). Balanced detection is a method which enables the rejection of "common mode" laser noise [110]. Then a digitizer (ATS-9371, AlazarTech, QC, Canada) recorded the interference signal digitally and sent it to the host laptop for further data processing.

5.2.3 Data and Image Processing

For 2D cross-section scanning, we took 1024 A-lines $\times$ 1024 B-frames to display a Bscan image in real time(60Hz). For 3D imaging and en-face imaging, we took 1024 A-lines $\times$ 512 B-frames $\times$ 512 C-frames to display en-face image and volume in $\sim$ 2.5s, which is limited by the line-scan rate of the source. By utilizing k-clock sampling, the raw data saved in the host laptop RAM is linear in the wavenumber k domain. The k-space fringe data set was then transferred to a laptop GPU(NVIDIA RTX A2000,12GB) for fast parallel computing and post-processed in real-time. A flow diagram of data processing is given in Figure 5.5.

The procedure is described as follows:

1. Data conversion: The raw data captured by the digitizer are unsigned short(16-bit), we first convert them to float(32-bit), which is a general data type processed by GPU.

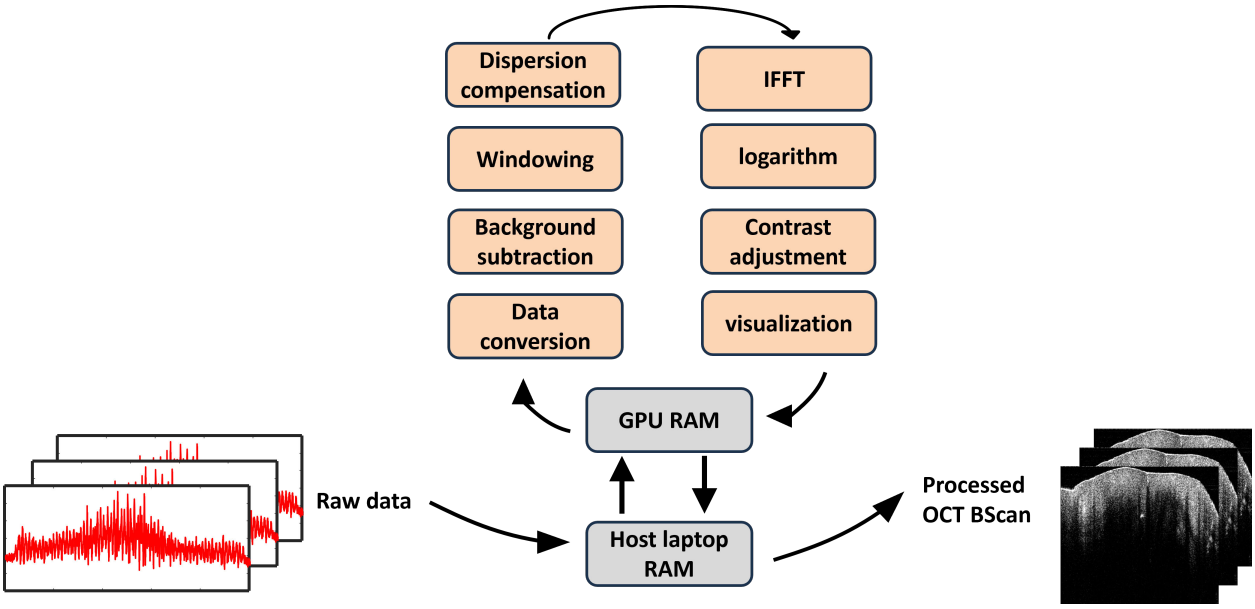

Figure 5.5: The flow diagram for processing SS-OCT data.

.

2. Background subtraction: The obtained OCT fringes from the SS-OCT system consist of AC terms of interference signals between reflected lights from reference and sample arms, and DC terms that originate from the self-interference of reference arm or sample arm. In this step, we remove the DC terms of interference signals to enhance image quality. There are two ways to perform background removal: (1) Average fringes from multiple A-ascans and subtract the averaged fringe from each original fringe. (2) Take separate OCT background data with the sample-arm light blocked. This background data will contain most of the DC terms from the self-interference of reference arm lights. Then, subtract the background data from the original data. Our system integrates both of the methods, allowing users to select the most suitable approach based on their specific use case.

3. Windowing: The convolution theorem states that the Fourier transform of the convolution of two signals is equal to the pointwise product of their Fourier transforms [111]. The implication of this is that the Fourier transform of the fringe envelope will be convolved with the image itself. This convolution operation can introduce undesirable effects, such as sidelobe artifacts and ringing patterns. Windowing is a technique employed to mitigate the effects of abrupt transitions at the boundaries of finite sequences acquired by the digitizer. It involves multiplying the time-domain signal by a finite-length window function whose amplitude varies smoothly, tapering gradually towards zero at the edges. This process ensures that the waveform's endpoints meet seamlessly, resulting in a continuous waveform without abrupt discontinuities or sharp transitions. We built several window functions in our system, like Gaussian window, hanging window and etc, allowing users to select the most suitable approach based on their specific use case.

4. Dispersion compensation: Dispersion is the phenomenon in which phase velocity of light traveling through a medium is dependent on wavelength [112]. Dispersion is related to optical materials that light propagates. For OCT, it is crucial to ensure that the dispersion in the reference arm precisely matches the dispersion in the sample arm. Differences in dispersion between the two arms will result in wavelength-dependent phase shifts in the fringe, which can degrade the image quality and introduce artifacts [113]. Dispersion compensation can be achieved physically by using the same optics for both reference and sample arms, or by adding compensating glasses in the reference arm. Another method is numerical dispersion compensation [114]. We can numerically

compensate the phase by adding the dispersion-related phase term described as [112]:

$$\Phi(\omega) = -\alpha_2(\omega - \omega_0)^2 - \alpha_3(\omega - \omega_0)^3 \tag{5.1}$$

which corrects both the 2^{nd} order and 3^{rd} order dispersion. In the post-processing procedure, it is done by multiplying the additional phase term $e^{i\Phi(\omega)}$ to the complex interference signals. By calibration, we can find the optimal α_2 and α_3 values by measuring the PSFs of the mirror images.

5. IFFT: To reconstruct an OCT image, the absolute value of the inverse Fourier transform of the acquired interference fringes is computed. However, due to the properties of the inverse Fourier transform, only half of the pixels within the resulting image will contain unique information. This is because the transformed fringe data contains two copies of the image: a real image and its complex conjugate counterpart. We simply crop half of the pixels to remove the conjugate part. We also have zero padding function to keep the data in the same pixel resolution, but the trade-off is the insufficient GPU memory.

6. Logarithm: Next the logarithm base 10 of the image is calculated. Converting the image to the logarithmic scale makes it easy to visualize the deep and dark regions of the tissue.

7. Contrast adjustment: The final step is to scale the image contrast to optimize the appearance of the OCT images.

After all the procedures, the OCT image data will be saved in GPU memory and displayed without transfer to RAM again by using the CUDA Toolkit. The detailed software is shown in Appendix A.

5.3 Results

5.3.1 System Integration

To develop a fully integrated system, we have designed the mechanical components and other necessary elements for prototyping a handheld multimodal intraoral probe. The schematic of the probe design is illustrated in Figure 5.6. As shown in Figure 5.6(a), the designed optical system is located in the middle of the probe head. A dichroic mirror(FF835-SDi01, Semrock) with Low group delay dispersion is employed to avoid the dispersion effect caused by the polarization difference [115]. The dichroic separates the NIR light from the OCT module and the visible light emitted by the LEDs. Finally, a camera(OV5648,5 megapixel, OmniVision) with a long-pass filter and an analyzer is employed to capture both cross-polarized bright-field and fluorescence images sequentially [116]. The final probe has a diameter of 20 mm and a working distance of 10 mm. Within the handle of the probe, a fiber collimator (F220APC-1310, Thorlabs), a right-angle mirror (Gold Coated, Edmund Optics Inc.), and a MEMS mirror are cascaded in a sequential arrangement to facilitate the delivery of the laser beam to the probe head. To achieve a compact design, a MEMS driver board and a Type-C breakout board are mounted at the bottom of the handle. The Type-C breakout board serves as a central interface, connecting all the electronic components within the probe, including the camera, LEDs, and MEMS driver board, to a laptop via a Thunderbolt

cable. In the front view, four 4000-K Luxeon Z ES LEDs equipped with polarizers are placed

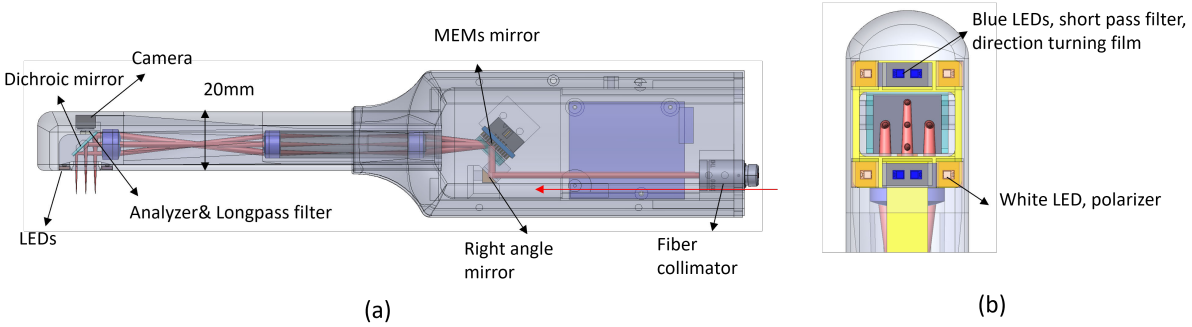

Figure 5.6: The schematic of the Multimodal intraoral probe. (a) Side view and (b) front view.

.

at four corners of the probe head, illuminating the oral cavity for conventional examinations. Four 405-nm Luxeon UV U1 LEDs (Lumileds, Amsterdam, Netherlands) are placed to serve as the excitation source for fluorescence imaging. To achieve more uniform excitation illumination, two direction-turning films (Luminit, LLC.) are employed to redirect the light from the blue LEDs toward the center of the imaging area. Figure 5.7 illustrates a comparison of the illumination under different conditions, clearly demonstrating that the direction-turning films enhance light concentration at the center of the sample plane, resulting in improved uniformity.

The handhold intraoral probe was fabricated using a 3D printer with biocompatible material. The final probe is shown in Figure 5.8. Most of the optical elements were passively aligned using a tight fit with the mechanical holders to ensure concentricity. A copper heat sink is integrated to cover the LED strip, maintaining a reasonable operating temperature for the LEDs. At the proximal end of the handle, a 2-meter single-mode fiber (SMF-28, Thorlabs) and a 2-meter Thunderbolt cable are provided to connect the probe with the

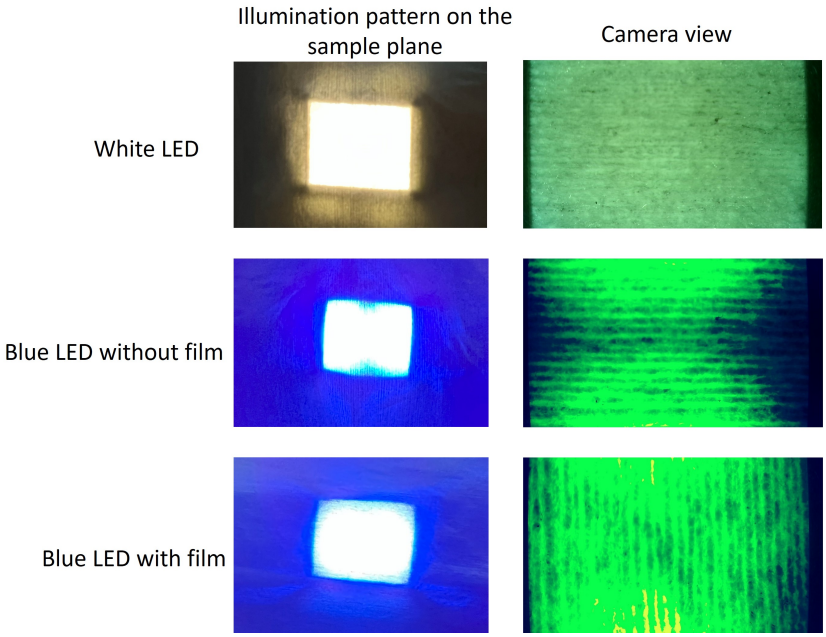

Figure 5.7: Comparison of the illumination under different conditions

.

SSOCT source and the laptop, respectively. This allows the user to operate the probe at a comfortable distance.

The Swept source laser, reference arm, fiber components, a NI data acquisition device (NI 6353, National Instruments) control panel, two LED control drivers (TPS92515HVEVM-749, Texas Instruments), and an LED power supply are integrated into a portable carry-on case, as shown in Figure 5.9(a). The complete multimodal intraoral screening system is depicted in Figure 5.9(b). The laptop comes with a PCIE chassis that contains the Alazar digitizer and the PCIE card for the NIDAQ card. The entire system was delivered to India for clinical evaluation in January 2024.

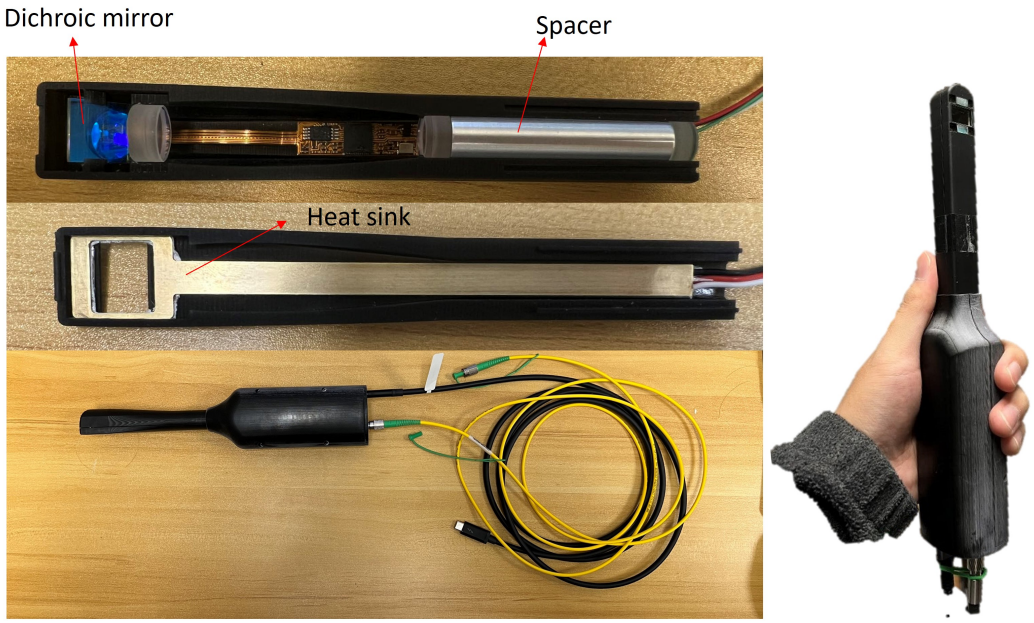

Figure 5.8: Photo of the multimodal intraoral probe.

.

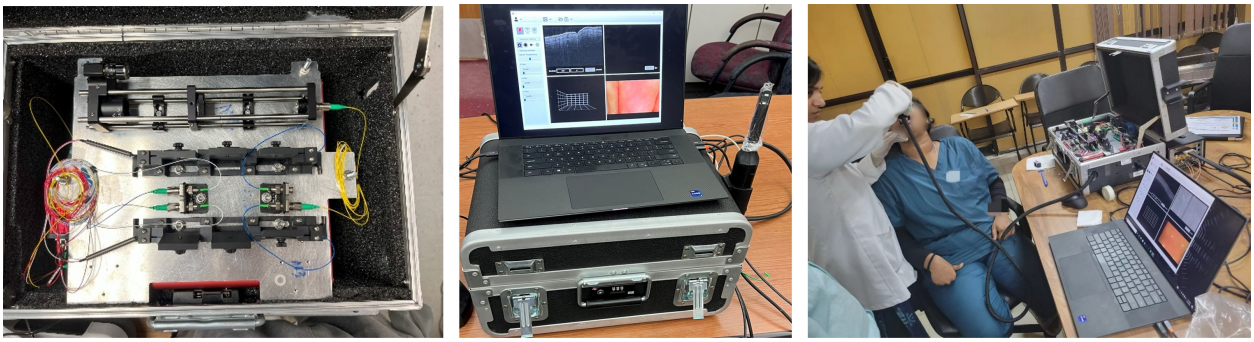

Figure 5.9: Packaging of the multimodal intraoral screening system.

.

5.3.2 Preliminary Results

Once the system was developed, we tested the intraoral probe with a USAF resolution target. The probe resolved up to group-5 element-4 when viewed with the en-face projection in real time as shown in Figure 5.10. There are 45.3-line pairs in group 5 element 4; therefore, the probe can resolve up to 22.0 µm, which is a little bit larger than the theoretical value of 13.1 µm. That may caused by the spherical aberration introduced by the probe window and protection sleeve.

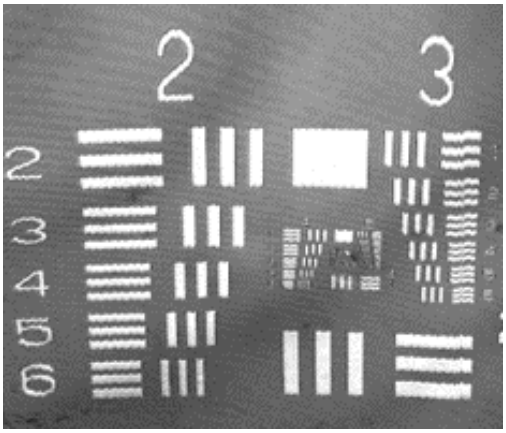

Figure 5.10: USAF resolution target, as observed under the en-face projection of SS-OCT.

.

Figure 5.11 shows the interface of the custom multimodal intraoral screening system, the detail of the software is demonstrated in Appendix A. The figure demonstrates the versatile multi-modality capabilities of the probe system, showcasing its ability to capture a comprehensive range of imaging data. This includes cross-sectional B-scans, en-face views, 3D volumetric reconstructions, as well as wide-field camera images for both conventional white light illumination and autofluorescence imaging modes.

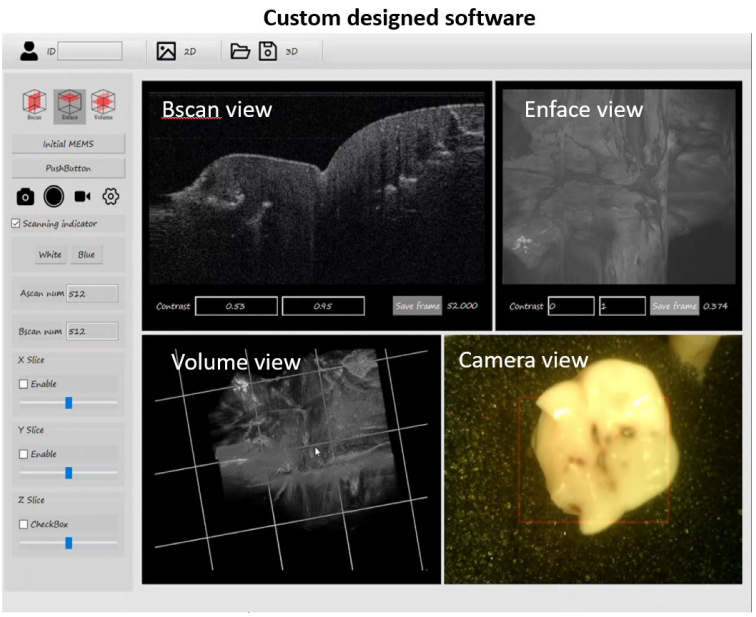

Figure 5.11: Custom multimodal intraoral screening system software

.

We validate and assess the performance of the multimodal probe through the acquisition of diverse samples. As depicted in Figure 5.12, the obtained healthy human intraoral images showcase both bright field and auto-fluorescent perspectives in (a) and (b), respectively.

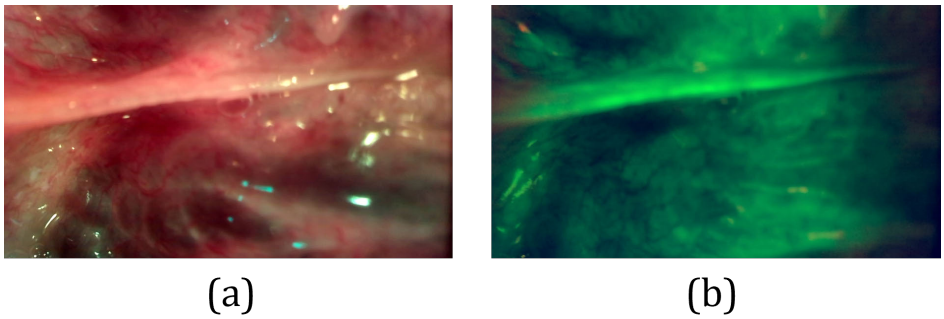

Figure 5.12: Human intraoral (a) bright field image and (b) autofluorescence image.

.

Figure 5.13 shows the cross-sectional Bscan images of different samples. The multi-layers in the tape in Figure 5.13 (a) and cracks in teeth in (b) are able to distinguish well.

The tissue structure depicted in (c) and (d) also shows the probe's capacity for producing high-quality images.

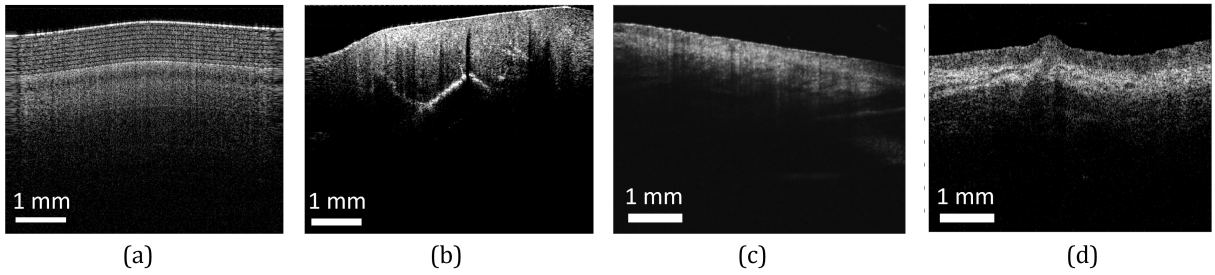

Figure 5.13: OCT Bscan images of (a) tape, (b) tooth, (c) skin, and (d) oral mucosa.

.

Figure 5.14 presents en-face and 3D images of various human samples, showcasing the versatility and potential of the imaging technique. Panels (a) and (e) display the en-face image and 3D volume, respectively, of a human finger. Panels (b) and (f) demonstrate the en-face image and 3D volume of a human tooth with visible cracks, highlighting the technique's ability to detect structural defects. Panels (c) and (g) depict the en-face image and 3D volume of the oral mucosa, providing insights into the anatomical structure of the oral cavity. Notably, panels (d) and (g) present the en-face image and 3D volume of OCTA data from (f), revealing the intricate vascular network beneath the oral skin. These comprehensive results underscore the 3D imaging capabilities of the technique and its promising future applications in oral cancer detection and diagnosis.

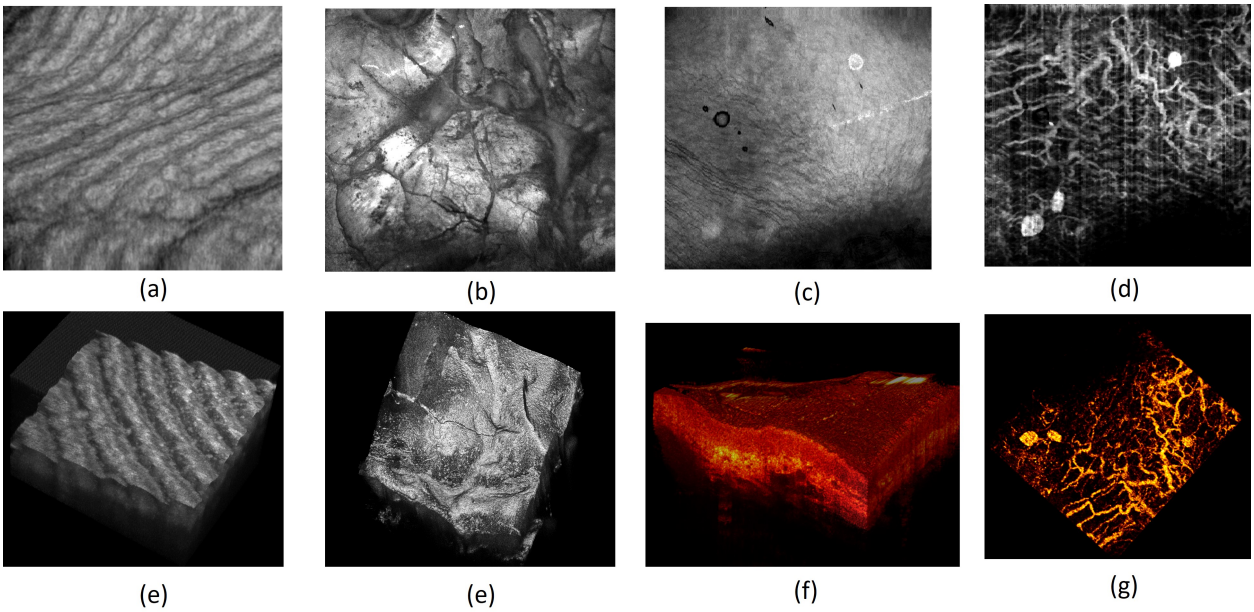

Figure 5.14: En-face and 3D images of various human samples.Panels (a) and (e) display the en-face image and 3D volume, respectively, of a human finger. Panels (b) and (f) demonstrate the en-face image and 3D volume of a human tooth with visible cracks, highlighting the technique's ability to detect structural defects. Panels (c) and (g) depict the en-face image and 3D volume of the oral mucosa, providing insights into the anatomical structure of the oral cavity. Notably, panels (d) and (g) present the en-face image and 3D volume of OCTA data from (f), revealing the intricate vascular network beneath the oral skin

.

5.4 Discussion

In this chapter, the development of a multimodal intraoral screening system capable of visualizing white light imaging, autofluorescence imaging, and OCT imaging was presented. First, a custom OCT lens system was designed to achieve NA of 0.037 with a diffraction-limited FOV of ±3.5 mm. The custom lenses were engineered to minimize chromatic aberration, ensuring a consistent PSF throughout the measurement range and reducing dispersion effects. The lens system achieved a lateral resolution of 13.1 µm and an axial resolution of approximately 7.5 µm over a depth range of 1.2 mm. The designed working distance of 10 mm facilitates a comfortable side-viewing experience. The output power from the probe is approximately 8 mW, providing a suitable SNR for tissue imaging. Secondly, the entire SSOCT setup and data processing pipeline were introduced, detailing the system's components and data acquisition methods. Furthermore, the system integration process was described, including mechanical design, fabrication, and assembly. The final system was integrated into a portable carry-on case, enabling convenient overseas travel and deployment. Preliminary results indicate that the multimodal intraoral screening system shows promise for oral cancer detection, offering a comprehensive imaging solution by combining white light imaging, autofluorescence imaging, and OCT imaging capabilities.

Admittedly, there are several limitations were found in the multimodal intraoral screening system.

1. While we have reduced the intraoral probe diameter to 20 mm, a smaller form factor would be desirable to adapt to more extreme conditions within the oral cavity.

2. The current probe provides a side-viewing capability, which may limit the ability to detect deep oral structures. A future design goal could involve a changeable probe head that supports both side-viewing and front-viewing configurations, enabling more comprehensive imaging of the oral cavity.

3. We observed that the OCT image quality is sensitive to the perpendicularity between the optical axis and the sample surface. Obtaining high-quality OCT images in certain locations of the oral cavity can be challenging due to the complex anatomy and varying surface orientations.

4. Capturing a 3D volume OCT image takes approximately 2 seconds, which can be challenging in terms of maintaining stability between the patient and the probe. To address this issue, we have designed probe caps that allow the probe to operate at a fixed working distance and easily cover the tissue without motion.

5. The current system control is achieved through the laptop's keyboard, making it difficult for the user to simultaneously operate the probe and laptop. In our next design iteration, we will integrate buttons on the probe itself, enhancing user-friendliness and streamlining the operation process.

Chapter 6

Conclusion

6.1 Summary

This dissertation explored the two 3D imaging techniques(Chromatic confocal microscopy and SS-OCT) with potential value for biomedical applications. The first chapter provided a comprehensive introduction to the fundamental principles underpinning these techniques and the necessary background information. To facilitate 3D imaging without mechanical scanning, two digital scanning chromatic confocal microscopes were developed. Three customized objective lens designs were thoroughly explored to aid in the construction of a more advanced chromatic confocal microscope with enhanced capabilities. Furthermore, a multimodal intraoral screening system was developed for oral cancer detection, enabling the seamless integration of white light imaging, autofluorescence imaging, and SS-OCT imaging modalities within a single platform.

Chapter 2 presented a compact DMD-based chromatic confocal microscope system that operated without any mechanical scanning components for surface profiling. The DMD served a dual role, functioning as both a multipoint source array and a detection pinhole array simultaneously. By displaying scanning point array patterns on the DMD, lateral scanning was achieved. Axial scanning was realized by the residual chromatic aberrations

inherent in the microscope objective and a singlet lens. Experiments have shown that it was capable of 3D imaging at a depth range of 45 µm. To address the issue of the tilted imaging plane caused by DMD, an improved DMD-based chromatic confocal microscope design was modeled and simulated using LightTools. The simulation results provided insights into the system's working principles, calibration methodologies, and 3D imaging capabilities.

Chapter 3 introduced a new MicroLED-based chromatic confocal microscope. Similar to the DMD-based system introduced in Chapter 2, this MicroLED-based chromatic confocal microscope employed a multipoint illumination strategy for lateral scanning and exploits longitudinal chromatic aberrations for axial scanning, eliminating the need for mechanical scanning components. The key advantages of this approach lie in its compact form factor, cost-effectiveness, and elimination of external light sources, as the MicroLED panel itself serves as the integrated illumination source. However, the limitations of the system were primarily dictated by the specifications of the employed MicroLED panel, including pixel size, pixel resolution, brightness, and spectral characteristics.

Chapter 4 explored the design and development of three water-immersed hyperchromatic confocal objective lenses aimed at extending the depth measurement range for chromatic confocal microscopy applications. The first design involved a hyperchromatic objective with a NA of 0.5 and a chromatic shift of 300 µm over a 50 nm bandwidth, specifically tailored for a MicroLED-based chromatic confocal system. The second design focused on a hyperchromatic objective with an NA of 0.7 and a substantially larger chromatic shift of 750 µm over a 300 nm bandwidth in the near-infrared (NIR) spectral range. The third design introduced a novel dual-view hyperchromatic objective that integrates both a high NA imaging mode and a wide-FOV imaging mode through a waveguide, enabling simultaneous acquisition of

both modalities. The first two objective lens designs employed diffraction elements and were successfully manufactured and tested to validate their performance. The third dual-view hyperchromatic objective, with its unique waveguide-based design, is slated for future fabrication and evaluation.

Finally, Chapter 5 focused on the development of a multimodal intraoral screening system capable of visualizing white light imaging, autofluorescence imaging, and OCT imaging. The chapter delved into the intricate details of optical system design, mechanical component engineering, SS-OCT system development, data processing pipeline, system integration, and final packaging. The culmination of these efforts resulted in a fully integrated and portable multimodal imaging platform housed in a compact carry-on case, facilitating convenient transportation and deployment, even for overseas applications. Preliminary results showcased the system's capabilities, demonstrating white light, autofluorescence, and OCT images acquired by the intraoral probe. These results show the potential promise of the system for oral cancer detection.

The future research directions, Firstly, we will build the new dual view chromatic confocal objective lens. This innovative design will enable simultaneous wide FOV visualization and high-resolution 3D imaging of tissue structures, facilitating efficient identification of regions of interest (ROIs) and detailed structural analysis within a single integrated platform. Another aspect that could be improved is to design and development of a dedicated spectrometer system with a matching bandwidth to the chromatic confocal system, while achieving high spectral resolution. This tailored spectrometer will enhance depth resolution and analysis capabilities, further improving the performance and accuracy of the chromatic confocal imaging modality. In terms of the multimodal intraoral screening system, efforts

will be directed towards designing a compact probe with a smaller form factor, capable of switching between side-view and front-view imaging modes. This versatile probe design will greatly benefit clinical practitioners by providing enhanced accessibility and visibility during intraoral examinations, ultimately improving the screening and diagnostic workflow. Moreover, the research endeavors will extend to the development of advanced OCT systems, focusing on OCT angiography [117] and polarization-sensitive OCT [118] techniques. These specialized imaging modalities hold significant potential for unique applications in oral cancer detection, enabling comprehensive evaluation of vascular and polarization properties of tissues, which could provide valuable insights into disease pathophysiology and aid in early diagnosis.

Appendix A

Multimodal Intraoral Screening System Software

One of the main contributions of my dissertation is developing a multimodal intraoral screening system from scratch. In this Appendix, I will mainly focus on the overall architecture design of software.

The multimodal intraoral screening system could be divided into three sub-systems: Hardware module, data acquisition module, and data processing module. The software is designed to integrate the hardware module, data acquisition module as well as data processing module in the host laptop and display the user interface to the user.

We choose QT(The Qt Company, Finland) as the application framework to design the GUI and handle its interaction with other sub-systems. Qt is a very popular framework used in GUI development. It is object-oriented and based on C++. Compared with the other potential candidate, Microsoft .NET Framework, it has the advantage of lightweight and cross-platform supportability. Unlike .NET, Qt supports literally all the operating systems ranging from Linux to Windows.

We take multithread strategy to arrange functions in the software. The application leverages a main thread dedicated to facilitating seamless user interaction with the graphical user interface (GUI). Additionally, multiple child threads are employed to handle var-

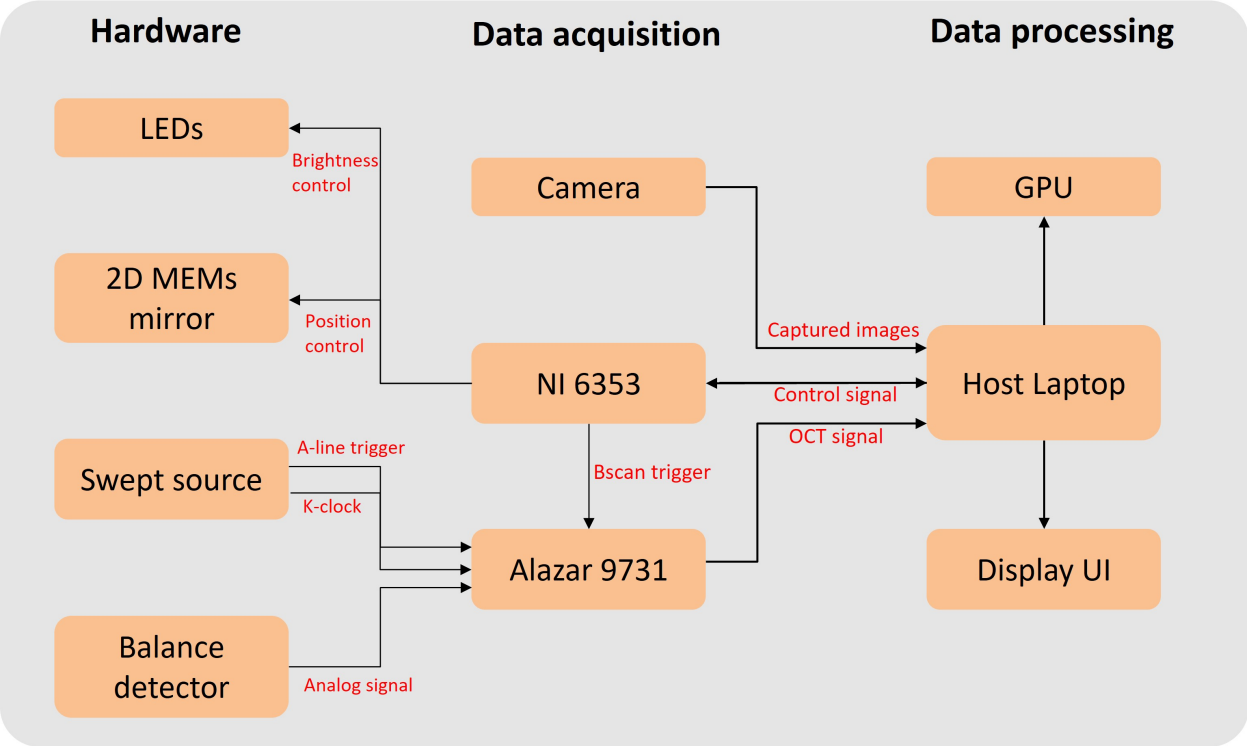

Figure A.1: The block diagram of the multimodal intraoral screening system. The system includes three sub-systems: Hardware module, data acquisition module, and data processing module.

ious functions concurrently, ensuring efficient and independent execution of distinct tasks, thereby enhancing the overall responsiveness and performance of the system. Each hardware component is controlled through its dedicated Application Programming Interface (API) implemented in C++. We have seamlessly integrated these individual APIs into our software, encapsulating them as distinct QObjects. This modular approach facilitates efficient hardware management and enables the software to leverage the capabilities of various hardware components seamlessly.

Our system seamlessly integrates the powerful OpenCV library, enabling precise camera control and high-quality 2D image rendering. Furthermore, we have incorporated CUDA, a cutting-edge parallel computing platform, to harness the computational power of graphics processing units. This strategic implementation significantly accelerates data processing speeds, resulting in a responsive and high-performance imaging solution.

The final UI is shown in Figure A.2. The top ribbon is a dedicated section that enables the user to input the patient's ID and create a folder. It also provides functionality to save and retrieve existing multimodal image data from the respective patient's folder. The left panel serves as the interactive interface, facilitating control over various imaging functions through intuitive buttons, configuring system parameters and display settings, etc. The right panel is divided into four sub-windows: Bscan view, Enface view, Volume view, and Camera view to display the captured image in real-time.

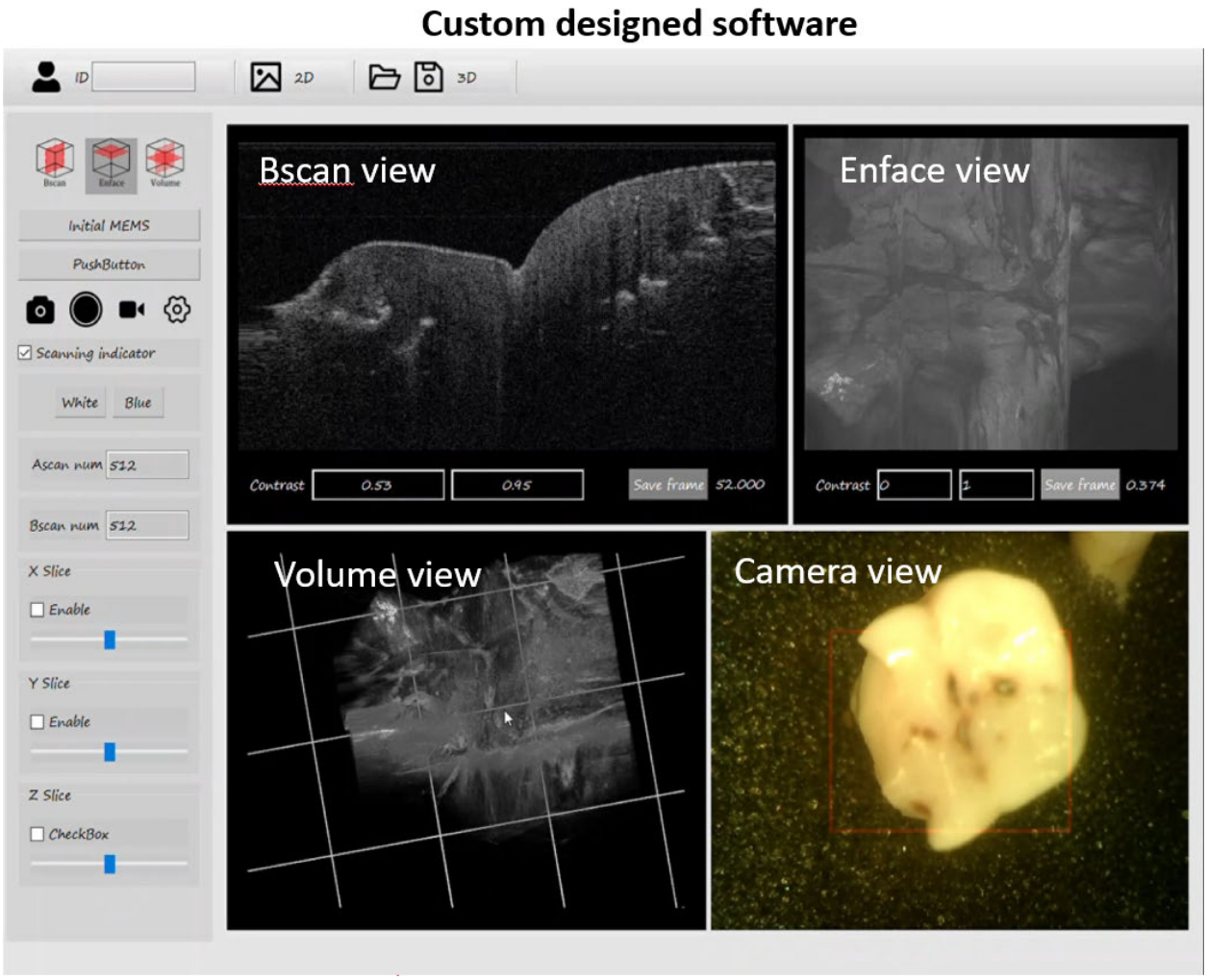

Figure A.2: The block diagram of the multimodal intraoral screening system. The system includes three sub-systems: Hardware module, data acquisition module, and data processing module.

Appendix B

Other Projects

This section includes the published manuscripts for other projects I involved in during my PhD program: 1) Mobile optical imaging platform for early cancer detection and diagnosis, 2) Portable smartphone-based Dark field microscope(DFM) device for Nanoparticle-enhanced EV immunoassays (NEI) assay. 3) Structured light dark-field microscope. The abstract of each manuscript is presented below:

(1) Mobile-based oral cancer classification for point-of-care screening:

Significance: Oral cancer is among the most common cancers globally, especially in low- and middle-income countries. Early detection is the most effective way to reduce the mortality rate. Deep learning-based cancer image classification models usually need to be hosted on a computing server. However, internet connection is unreliable for screening in low-resource settings.

Aim: To develop a mobile-based dual-mode image classification method and customized Android application for point-of-care oral cancer detection.

Approach: The dataset used in our study was captured among 5025 patients with our customized dual-modality mobile oral screening devices. We trained an efficient network MobileNet with focal loss and converted the model into TensorFlow Lite format. The final-

ized lite format model is ∼16.3 MB and ideal for smartphone platform operation. We have developed an Android smartphone application in an easy-to-use format that implements the mobile-based dual-modality image classification approach to distinguish oral potentially malignant and malignant images from normal/benign images.

Results: We investigated the accuracy and running speed on a cost-effective smartphone computing platform. It takes ∼300 ms to process one image pair with the Moto G5 Android smartphone. We tested the proposed method on a standalone dataset and achieved 81% accuracy for distinguishing normal/benign lesions from clinically suspicious lesions, using a gold standard of clinical impression based on the review of images by oral specialists.

Conclusions: Our study demonstrates the effectiveness of a mobile-based approach for oral cancer screening in low-resource settings.

(2) Diagnosis of paediatric tuberculosis by optically detecting two virulence factors on extracellular vesicles in blood samples *in vivo*

Sensitive and specific blood-based assays for the detection of pulmonary and extrapulmonary tuberculosis would reduce mortality associated with missed diagnoses, particularly in children. Here we report a nanoparticle-enhanced immunoassay read by dark-field microscopy that detects two Mycobacterium tuberculosis virulence factors (the glycolipid lipoarabinomannan and its carrier protein) on the surface of circulating extracellular vesicles. In a cohort study of 147 hospitalized and severely immunosuppressed children living with HIV, the assay detected 58 of the 78 (74%) cases of paediatric tuberculosis, 48 of the 66 (73%) cases that were missed by microbiological assays, and 8 out of 10 (80%) cases undiagnosed during the study. It also distinguished tuberculosis from latent-tuberculosis infections in non-human primates. We adapted the assay to make it portable and operable by a smart-

phone. With further development, the assay may facilitate the detection of tuberculosis at the point of care, particularly in resource-limited settings.

(3) Structured light dark-field microscope

A resolution-enhanced dark-field microscope by structured light illumination is proposed to improve resolution and contrast. A set of phase-shifted fringes are projected to the sample plane at large angle to capture modulated dark-field images, from which resolution- and contrast-enhanced dark-field image, as well as sectioned dark-field image, can be obtained. Human tissue samples are tested to demonstrate the resolution and contrast enhancement. The system can be implemented in transmission mode and reflectance-mode, with potential applications ranging from defect detection to biomedical imaging.

REFERENCES

[1] Adrien Depeursinge et al. "Three-dimensional solid texture analysis in biomedical imaging: review and opportunities". In: *Medical image analysis* 18.1 (2014), pp. 176–196.

[2] Jayaram K Udupa and Gabor T Herman. *3D imaging in medicine*. CRC press, 1999.

[3] Elliot K Fishman et al. "Three-dimensional imaging." In: *Radiology* 181.2 (1991), pp. 321–337.

[4] Maria Vinci, Carol Box, and Suzanne A Eccles. "Three-dimensional (3D) tumor spheroid invasion assay". In: *JoVE (Journal of Visualized Experiments)* 99 (2015), e52686.

[5] Nicholas J Mankovich et al. "Surgical planning using three-dimensional imaging and computer modeling". In: *Otolaryngologic Clinics of North America* 27.5 (1994), pp. 875–889.

[6] Karl H Höhne, Henry Fuchs, and Stephen M Pizer. *3D imaging in medicine: algorithms, systems, applications*. Vol. 60. Springer Science & Business Media, 2012.

[7] Hrebesh M Subhash and Ruikang K Wang. "Optical coherence tomography: technical aspects". In: *Biomedical Optical Imaging Technologies: Design and Applications* (2013), pp. 163–212.

[8] David A Agard and John W Sedat. “Three-dimensional architecture of a polytene nucleus”. In: *Nature* 302.5910 (1983), pp. 676–681.

[9] WB Amos and JG White. “How the confocal laser scanning microscope entered biological research”. In: *Biology of the Cell* 95.6 (2003), pp. 335–342.

[10] DK Hamilton and T Wilson. “Three-dimensional surface measurement using the confocal scanning microscope”. In: *Applied Physics B* 27 (1982), pp. 211–213.

[11] David Huang et al. “Optical coherence tomography”. In: *Science* 254.5035 (1991), pp. 1178–1181.

[12] Julia Welzel. “Optical coherence tomography in dermatology: a review”. In: *Skin Research and Technology: Review article* 7.1 (2001), pp. 1–9.

[13] JGDW Fujimoto and Wolfgang Drexler. “Introduction to optical coherence tomography”. In: *Optical coherence tomography: Technology and applications*. Springer, 2008, pp. 1–45.

[14] Vincent Chan and Anahi Perlas. “Basics of ultrasound imaging”. In: *Atlas of ultrasound-guided procedures in interventional pain management* (2011), pp. 13–19.

[15] Peter NT Wells. “Ultrasound imaging”. In: *Physics in medicine & biology* 51.13 (2006), R83.

[16] Thorsten M Buzug. “Computed tomography”. In: *Springer handbook of medical technology*. Springer, 2011, pp. 311–342.

[17] Girish Katti, Syeda Arshiya Ara, and Ayesha Shireen. “Magnetic resonance imaging (MRI)–A review”. In: *International journal of dental clinics* 3.1 (2011), pp. 65–70.

[18] Vincent S Khoo et al. "Magnetic resonance imaging (MRI): considerations and applications in radiotherapy treatment planning". In: *Radiotherapy and Oncology* 42.1 (1997), pp. 1–15.

[19] Jeff W Lichtman. "Confocal microscopy". In: *Scientific American* 271.2 (1994), pp. 40–45.

[20] Min Gu. *Principles of three dimensional imaging in confocal microscopes*. World Scientific, 1996.

[21] Robert H Webb and Fran Rogomentich. "Confocal microscope with large field and working distance". In: *Applied optics* 38.22 (1999), pp. 4870–4875.

[22] James Pawley. *Handbook of biological confocal microscopy*. Vol. 236. Springer Science & Business Media, 2006.

[23] Tony Wilson. "The role of the pinhole in confocal imaging system". In: *Handbook of biological confocal microscopy*. Springer, 1995, pp. 167–182.

[24] Min Gu, T Tannous, and JR Sheppard. "Effect of an annular pupil on confocal imaging through highly scattering media". In: *Optics letters* 21.5 (1996), pp. 312–314.

[25] Stephen W Paddock. "Principles and practices of laser scanning confocal microscopy". In: *Molecular biotechnology* 16 (2000), pp. 127–149.

[26] DK Hamilton, Tony Wilson, and CJR Sheppard. "Experimental observations of the depth-discrimination properties of scanning microscopes". In: *Optics letters* 6.12 (1981), pp. 625–626.

[27] T. Wilson and C. Sheppard. *Theory and Practice of Scanning Optical Microscopy*. Academic Press, 1984.

[28] David H Marimont and Brian A Wandell. "Matching color images: the effects of axial chromatic aberration". In: *JOSA A* 11.12 (1994), pp. 3113–3122.

[29] José Sasián. *Introduction to aberrations in optical imaging systems*. Cambridge University Press, 2013.

[30] Rudolf Kingslake. *Lens design fundamentals*. Elsevier, 2012.

[31] Hans Bach and Norbert Neuroth. *The properties of optical glass*. Springer Science & Business Media, 1998.

[32] Amicia D Elliott. "Confocal microscopy: principles and modern practices". In: *Current protocols in cytometry* 92.1 (2020), e68.

[33] Peng Xi, Yujia Liu, and Qiushi Ren. "Scanning and image reconstruction techniques in confocal laser scanning microscopy". In: *Laser Scanning, Theory and Applications*. IntechOpen, 2011.

[34] Luca Lanzanò and Enrico Gratton. "Orbital single particle tracking on a commercial confocal microscope using piezoelectric stage feedback". In: *Methods and applications in fluorescence* 2.2 (2014), p. 024010.

[35] Shaobai Li et al. "Rapid measurement and compensation method of eccentricity in automatic profile measurement of the ICF capsule". In: *Applied Optics* 57.14 (2018), pp. 3761–3769.

[36] Hanxu Wu et al. "Divided-aperture confocal Brillouin microscopy for simultaneous high-precision topographic and mechanical mapping". In: *Optics Express* 28.21 (2020), pp. 31821–31831.

[37] Paul C Lin et al. "Single-shot depth-section imaging through chromatic slit-scan confocal microscopy". In: *Applied optics* 37.28 (1998), pp. 6764–6770.

[38] G Molesini et al. "Focus-wavelength encoded optical profilometer". In: *Optics communications* 49.4 (1984), pp. 229–233.

[39] M Maly and A Boyde. "Real-time stereoscopic confocal reflection microscopy using objective lenses with linear longitudinal chromatic dispersion". In: *Scanning* 16.3 (1994), pp. 187–192.

[40] J Meneses et al. "Chromatic confocal microscopy by means of continuum light generated through a standard single-mode fibre". In: *Journal of Optics A: Pure and Applied Optics* 6.6 (2004), p. 544.

[41] H Ernst Keller. "Objective lenses for confocal microscopy". In: *Handbook of biological confocal microscopy*. Springer, 2006, pp. 145–161.

[42] Kebin Shi et al. "Chromatic confocal microscopy using supercontinuum light". In: *Optics Express* 12.10 (2004), pp. 2096–2101.

[43] Michael Zint et al. "Development and verification of a snapshot dental intraoral three-dimensional scanner based on chromatic confocal imaging". In: *Journal of Medical Imaging* 6.3 (2019), pp. 033502–033502.

[44] Cory Olsovsky et al. “Chromatic confocal microscopy for multi-depth imaging of epithelial tissue”. In: *Biomedical optics express* 4.5 (2013), pp. 732–740.

[45] Hans J Tiziani and H-M Uhde. “Three-dimensional image sensing by chromatic confocal microscopy”. In: *Applied optics* 33.10 (1994), pp. 1838–1843.

[46] A Gh Podoleanu. “Optical coherence tomography”. In: *The British journal of radiology* 78.935 (2005), pp. 976–988.

[47] Brett E Bouma and GJ Tearney. “Clinical imaging with optical coherence tomography”. In: *Academic radiology* 9.8 (2002), pp. 942–953.

[48] Abdullah Al-Mujaini, Upender K Wali, and Sitara Azeem. “Optical coherence tomography: clinical applications in medical practice”. In: *Oman medical journal* 28.2 (2013), p. 86.

[49] Caroline R Baumal. “Clinical applications of optical coherence tomography”. In: *Current opinion in ophthalmology* 10.3 (1999), pp. 182–188.

[50] NKT Photonics. *Optical Coherence Tomography, OCT*. Accessed on 26 March 2024. URL: https://www.nktphotonics.com/applications/bio-imaging-and-microscopy/optical-coherence-tomography-oct/.

[51] Silke Aumann et al. “Optical coherence tomography (OCT): principle and technical realization”. In: *High resolution imaging in microscopy and ophthalmology: new frontiers in biomedical optics* (2019), pp. 59–85.

[52] Victor XD Yang and I Alex Vitkin. “Principles of doppler oct”. In: *Optical Coherence Tomography in Cardiovascular Research*. CRC Press, 2007, pp. 321–334.

[53] Joseph M. Schmitt. "Optical coherence tomography (OCT): a review". In: *IEEE Journal of Selected Topics in Quantum Electronics* 5.4 (1999), pp. 1205–1215.

[54] Zahid Yaqoob, Jigang Wu, and Changhuei Yang. "Spectral domain optical coherence tomography: a better OCT imaging strategy". In: *Biotechniques* 39.6 (2005), S6–S13.

[55] Kevin C. Zhou, Ruikang K. Wang, and Steven G. Adie. "Unified k-space theory of optical coherence tomography". In: *Advances in Optics and Photonics* 13.2 (2021), pp. 462–514.

[56] Zofia Michalewska and Jerzy Nawrocki. *Atlas of swept source optical coherence tomography*. No. 25204. Springer International Publishing, 2017.

[57] S. R. Chinn, E. A. Swanson, and J. G. Fujimoto. "Optical coherence tomography using a frequency-tunable optical source". In: *Optics Letters* 22.5 (1997), pp. 340–342.

[58] Ines Lains et al. "Retinal applications of swept source optical coherence tomography (OCT) and optical coherence tomography angiography (OCTA)". In: *Progress in retinal and eye research* 84 (2021), p. 100951.

[59] Andrew J Tatham. "Clinical advantages of swept-source OCT and new non-damaging laser treatments". In: *Rev Ophthalmol* 2014 (2014), pp. 1–8.

[60] James G. Fujimoto and Joseph M. Schmitt. "Principles of OCT". In: *Optical Coherence Tomography in Cardiovascular Research*. CRC Press, 2007, pp. 35–50.

[61] Jukka T Hast et al. "Enhancing the OCT images by the low-coherence fringe envelope deconvolution method". In: *ALT'03 International Conference on Advanced Laser Technologies: Biomedical Optics*. Vol. 5486. SPIE. 2004, pp. 180–186.

[62] Wolfgang Drexler and James G. Fujimoto. *Optical coherence tomography: technology and applications*. Ed. by Wolfgang Drexler and James G. Fujimoto. Springer Science & Business Media, 2008.

[63] Lumbroso Bruno and Rispoli Marco. *Guide to interpreting spectral domain optical coherence tomography*. JP Medical Ltd, 2011.

[64] Max Born and Emil Wolf. *Principles of Optics, Sixth Edition*. Pergamon Press, 1980.

[65] Kazuhiro Sasaki et al. "Extended depth of focus adaptive optics spectral domain optical coherence tomography". In: *Biomedical optics express* 3.10 (2012), pp. 2353–2370.

[66] Wolfgang Drexler et al. "Optical coherence tomography today: speed, contrast, and multimodality". In: *Journal of biomedical optics* 19.7 (2014), pp. 071412–071412.

[67] JH Massig et al. "Real-time confocal laser scan microscope for examination and diagnosis of the eye in vivo". In: *Applied optics* 33.4 (1994), pp. 690–694.

[68] Sanghoon Choi et al. "Development of a high speed laser scanning confocal microscope with an acquisition rate up to 200 frames per second". In: *Optics express* 21.20 (2013), pp. 23611–23618.

[69] Takeo Tanaami et al. “High-speed confocal fluorescence microscopy using a nipkow scanner with microlenses for 3-d imaging of single fluorescent molecule in real time”. In: *Bioimages* 4.2 (1996), pp. 57–62.

[70] Akihiko Nakano. “Spinning-disk confocal microscopy—a cutting-edge tool for imaging of membrane traffic”. In: *Cell structure and function* 27.5 (2002), pp. 349–355.

[71] Christopher L Arrasmith, David L Dickensheets, and Anita Mahadevan-Jansen. “MEMS-based handheld confocal microscope for in-vivo skin imaging”. In: *Optics express* 18.4 (2010), pp. 3805–3819.

[72] Benno HW Hendriks et al. “High-resolution resonant and nonresonant fiber-scanning confocal microscope”. In: *Journal of biomedical optics* 16.2 (2011), pp. 026007–026007.

[73] Matthias Hillenbrand et al. “Chromatic confocal matrix sensor with actuated pinhole arrays”. In: *Applied optics* 54.15 (2015), pp. 4927–4936.

[74] Qi Cui and Rongguang Liang. “Chromatic confocal microscopy using liquid crystal display panels”. In: *Applied optics* 58.8 (2019), pp. 2085–2090.

[75] D Lee, D-G GWEON, and Hongki Yoo. “Multipoint scanning dual-detection confocal microscopy for fast 3D volumetric measurement”. In: *Journal of Microscopy* 270.2 (2018), pp. 200–209.

[76] Elliott L Botvinick et al. “In-vivo confocal microscopy based on the Texas Instruments digital micromirror device”. In: *Optical Diagnostics of Living Cells III*. Vol. 3921. SPIE. 2000, pp. 12–19.

[77] Qingqing Wang et al. “Parallel detection experiment of fluorescence confocal microscopy using DMD”. In: *Scanning* 38.3 (2016), pp. 234–239.

[78] MA Browne, O Akinyemi, and Alan Boyde. “Confocal surface profiling utilizing chromatic aberration”. In: *Scanning* 14.3 (1992), pp. 145–153.

[79] Tony Wilson. “Scanning optical microscopy”. In: *Scanning* 7.2 (1985), pp. 79–87.

[80] T Wilson and AR Carlini. “Three-dimensional imaging in confocal imaging systems with finite sized detectors”. In: *Journal of microscopy* 149.1 (1988), pp. 51–66.

[81] Lewis Larmore. “Introduction to photographic principles”. In: (1965).

[82] Shaobai Li and Rongguang Liang. “DMD-based three-dimensional chromatic confocal microscopy”. In: *Applied optics* 59.14 (2020), pp. 4349–4356.

[83] Jose M Sasian. “Image plane tilt in optical systems”. In: *Optical engineering* 31.3 (1992), pp. 527–532.

[84] James W Howard. “Formulas for the coma and astigmatism of wedge prisms used in converging light”. In: *Applied optics* 24.23 (1985), pp. 4265–4268.

[85] Yuge Huang et al. “Prospects and challenges of mini-LED and micro-LED displays”. In: *Journal of the Society for Information Display* 27.7 (2019), pp. 387–401.

[86] JY Lin and HX Jiang. “Development of microLED”. In: *Applied Physics Letters* 116.10 (2020).

[87] Emilio Sánchez-Ortiga et al. “Subtractive imaging in confocal scanning microscopy using a CCD camera as a detector”. In: *Optics letters* 37.7 (2012), pp. 1280–1282.

[88] JS George et al. *Virtual pinhole confocal microscope*. Tech. rep. Los Alamos National Lab.(LANL), Los Alamos, NM (United States), 1999.

[89] W Gray Jerome. "Digital image capture for confocal microscopy". In: *Basic Confocal Microscopy* (2011), pp. 133–155.

[90] AK Ruprecht, TF Wiesendanger, and HJ Tiziani. "Chromatic confocal microscopy with a finite pinhole size". In: *Optics letters* 29.18 (2004), pp. 2130–2132.

[91] Shaobai Li et al. "MicroLED chromatic confocal microscope". In: *Optics letters* 46.11 (2021), pp. 2722–2725.

[92] Matthias Hillenbrand et al. "Hybrid hyperchromats for chromatic confocal sensor systems". In: *Advanced Optical Technologies* 1.3 (2012), pp. 187–194.

[93] A. G. Schott. *Optical Glass Catalogue*. Mainz, Germany, 2011.

[94] Jiabin Chen et al. "Large chromatic shift objective for chromatic confocal microscopy". In: *Three-Dimensional and Multidimensional Microscopy: Image Acquisition and Processing XXXI*. SPIE. 2024, PC1284804.

[95] Bernard C Kress. "Optical waveguide combiners for AR headsets: features and limitations". In: *Digital Optical Technologies 2019*. Vol. 11062. SPIE. 2019, pp. 75–100.

[96] Dewen Cheng et al. "Design and manufacture AR head-mounted displays: A review and outlook". In: *Light: Advanced Manufacturing* 2.3 (2021), pp. 350–369.

[97] Jonathan D Waldern, Ratson Morad, and Milan M Popovich. "Waveguide manufacturing for AR displays, past, present and future". In: *Frontiers in Optics*. Optica Publishing Group. 2018, FW5A–1.

[98] Jeremy Goodsell et al. “Metagrating meets the geometry-based efficiency limit for AR waveguide in-couplers”. In: *Optics Express* 31.3 (2023), pp. 4599–4614.

[99] Miaomiao Xu and Hong Hua. “Methods of optimizing and evaluating geometrical lightguides with microstructure mirrors for augmented reality displays”. In: *Optics express* 27.4 (2019), pp. 5523–5543.

[100] Saturu Yoneyama et al. “Lens distortion correction for digital image correlation by measuring rigid body displacement”. In: *Optical engineering* 45.2 (2006), pp. 023602–023602.

[101] Dr. Chinnababu Sunkavalli. *Signs and Symptoms of Oral Cancer*. Accessed: 2024-06-04. 2024. URL: https://www.drchinnababu.com/signs-and-symptoms-of-oral-cancer/.

[102] Poul Erik Petersen. *Strengthening the prevention of oral cancer: the WHO perspective*. 2005.

[103] World Health Organization et al. “Control of oral cancer in developing countries”. In: *Bull World Hlth Org* 62 (1984), pp. 817–830.

[104] Poul Erik Petersen. “Oral cancer prevention and control–the approach of the World Health Organization”. In: *Oral oncology* 45.4-5 (2009), pp. 454–460.

[105] Rengaswamy Sankaranarayanan et al. “Cancer survival in Africa, Asia, and Central America: a population-based study”. In: *The lancet oncology* 11.2 (2010), pp. 165–173.

[106] Ross D Uthoff et al. “Point-of-care, smartphone-based, dual-modality, dual-view, oral cancer screening device with neural network classification for low-resource communities”. In: *PloS one* 13.12 (2018), e0207493.

[107] Bill W Colston et al. “Dental oct”. In: *Optics express* 3.6 (1998), pp. 230–238.

[108] Bofan Song et al. “Mobile-based oral cancer classification for point-of-care screening”. In: *Journal of biomedical optics* 26.6 (2021), pp. 065003–065003.

[109] Masahiro Watanabe and Shree K Nayar. “Telecentric optics for focus analysis”. In: *IEEE Transactions on Pattern Analysis and Machine Intelligence* 19.12 (1997), pp. 1360–1365.

[110] Xiaoli Jin et al. “Balanced homodyne detection with high common mode rejection ratio based on parameter compensation of two arbitrary photodiodes”. In: *Optics Express* 23.18 (2015), pp. 23859–23866.

[111] JN Whiteley. “Notes on a theorem on convolutions”. In: *Proceedings of the American Mathematical Society* 16.1 (1965), pp. 1–7.

[112] Maciej Wojtkowski et al. “Ultrahigh-resolution, high-speed, Fourier domain optical coherence tomography and methods for dispersion compensation”. In: *Optics express* 12.11 (2004), pp. 2404–2422.

[113] Dierck Hillmann et al. “Common approach for compensation of axial motion artifacts in swept-source OCT and dispersion in Fourier-domain OCT”. In: *Optics express* 20.6 (2012), pp. 6761–6776.

[114] Liuhua Pan et al. “Depth-dependent dispersion compensation for full-depth OCT image”. In: *Optics express* 25.9 (2017), pp. 10345–10354.

[115] Pengfei Zhang et al. “Adaptive optics with combined optical coherence tomography and scanning laser ophthalmoscopy for in vivo mouse retina imaging”. In: *Ophthalmic Technologies XXVIII*. Vol. 10474. SPIE. 2018, pp. 137–145.

[116] Shakir Khan et al. “Clinical assessment of a low-cost, hand-held, smartphone-attached intraoral imaging probe for 5-aminolevulinic acid photodynamic therapy monitoring and guidance”. In: *Journal of Biomedical Optics* 28.8 (2023), pp. 082809–082809.

[117] Talisa E De Carlo et al. “A review of optical coherence tomography angiography (OCTA)”. In: *International journal of retina and vitreous* 1 (2015), pp. 1–15.

[118] Johannes F De Boer, Christoph K Hitzenberger, and Yoshiaki Yasuno. “Polarization sensitive optical coherence tomography–a review”. In: *Biomedical optics express* 8.3 (2017), pp. 1838–1873.